Universität Rostock Traditio et Innovatio

LEIBNIZ-INSTITUTE OF ATMOSPHERIC PHYSICS IAP

Multi Field of View Observations of Wind, Aerosol and Temperature using a Compact, Frequency Scanning Lidar

Dissertation
zur
Erlangung des akademischen Grades
doctor rerum naturalium (Dr. rer. nat.)
an der Mathematisch-Naturwissenschaftlichen Fakultät
der Universität Rostock

VORGELEGT VON:
Thorben H. Mense, geb. am 09.06.1992 in Bielefeld

GUTACHTER:
Prof. Dr. Franz-Josef Lübken, Univ. Rostock / IAP
Dr. habil. Alain Hauchecorne, Univ. Versailles / LATMOS

EINGEREICHT AM: 28.05.2024 VERTEIDIGT AM: 17.01.2025

Leibniz-Institut für Atmosphärenphysik e.V. an der Universität Rostock
Optische Sondierungen und Höhenforschungsraketen
Schlossstraße 6, 18225 Kühlungsborn

https://doi.org/10.18453/rosdok_id00005119

Abstract: Our atmosphere is a complex system in which numerous processes occur on various spatial and temporal scales, connecting the different layers of the atmosphere. To explore this system, the VAHCOLI (**V**ertical **A**nd **H**orizontal **CO**verage by **LI**dar) concept was developed at the Leibniz Institute of Atmospheric Physics (IAP), aiming for high-resolution detection of vertical, horizontal, and temporal scales using a lidar array. Part of this concept are compact, transportable Doppler lidars (approx. 1 m^3) with daylight capability and multiple fields of view (MFOV). This dissertation describes the development and application of the necessary extension for simultaneous measurement of wind, temperature, and aerosols in five fields of view. A major focus of the work is on the technical development of the extension, the theoretical considerations underlying the design, and the necessary modifications to the existing lidar. The technical development of the MFOV upgrade, including the optimization of the telescope design, the beam switching mechanisms, and the integration of advanced temperature management systems for the lidar telescope optics, is comprehensively described. Another focus is on the evaluation of measurements with the extended system, conducted during several measurement campaigns between December 2022 and April 2023 at the IAP (54°07'N; 11°46'O). Various new methods were developed to process the raw data into wind, temperatures, and aerosol parameters. The results of the measurement campaigns demonstrate the performance of the extended system. Winds in the five fields of view were measured at heights of up to 25 km solely by aerosol backscattering. The observation of a meridional wind gradient by comparing two opposing fields of view demonstrates the system's ability to capture horizontal scales. The backscatter ratio and backscatter coefficient of aerosols were determined and then used to calculate temperatures in aerosol-influenced atmospheric layers. The lidar measured winds were compared with the data from the European Centre for Medium-Range Weather Forecasts (ECMWF) and measurements of the satellite lidar Aeolus. For a comparison of the backscatter coefficients, results from the WACCM-CARMA model were used, and the temperatures were compared with ECMWF temperatures and lidar measurements of another IAP lidar. Good matches underline the effectiveness of the developed processing methods. New in the results of this work is the measurement in the middle atmosphere using five fields of view, the development of new processing methods, the determination of 3D winds between 3 and 25 km solely by aerosol backscattering, the high sensitivity of the aerosol measurements, and the determination of accurate temperatures using Rayleigh integration in the presence of aerosols. These results demonstrate the capabilities of the lidar with MFOV extension, and will be used in future measurement campaigns, for example, to validate new spaceborne lidars.

Kurzfassung: Unsere Atmosphäre ist ein komplexes System, in dem zahlreiche Prozesse auf verschiedenen räumlichen und zeitlichen Skalen ablaufen und die verschiedenen Schichten der Atmosphäre miteinander verbinden. Zur Erforschung dieses Systems wurde am Leibniz-Institut für Atmosphärenphysik das Konzept VAHCOLI (**V**ertical **A**nd **H**orizontal **CO**verage by **LI**dar) entwickelt, das eine hochauflösende Erfassung vertikaler, horizontaler und zeitlicher Skalen mittels eines Lidar-Arrays zum Ziel hat. Teil dieses Konzeptes sind kompakte, transportable Doppler-Lidare (ca. 1 m^3) mit Tageslichtfähigkeit und mehreren Sichtfeldern (Multi Field of View, MFOV). Diese Dissertation untersucht die Entwicklung und Anwendung der nötigen Erweiterung zur simultanen Messung von Wind, Temperatur und Aerosolen in mehreren Sichtfeldern. Ein Schwerpunkt der Arbeit liegt auf der technischen Entwicklung der Erweiterung, den theoretischen Überlegungen, die dem Design zugrunde liegen, sowie den notwendigen Modifikationen am bestehenden Lidar. Die technische Entwicklung des MFOV-Upgrades, einschließlich der Optimierung des Teleskopdesigns, der Strahlumschaltmechanismen und der Integration fortschrittlicher Temperaturmanagementsysteme für die Lidar-Teleskop-Optiken, wird umfassend beschrieben. Ein weiterer Fokus liegt auf der Auswertung von Messungen mit dem erweiterten System, die im Rahmen mehrerer Messkampagnen zwischen Dezember 2022 und April 2023 am IAP (54°07'N; 11°46'O) durchgeführt wurden. Dabei wurden verschiedene neue Methoden entwickelt, um die Rohdaten zu Winden, Temperaturen und Aerosolparametern zu verarbeiten. Die Ergebnisse der Messkampagnen zeigen die Leistungsfähigkeit des erweiterten Systems. 3D-Winde konnten in Höhen von bis zu 25 km allein mittels Aerosolrückstreuung gemessen werden. Die Beobachtung eines meridionalen Windgradienten durch den Vergleich zweier gegenüberliegender Sichtfelder zeigt die Fähigkeit des Systems, horizontale Skalen zu erfassen. Das Rückstreuverhältnis und der Rückstreukoeffizient von Aerosolen wurden erfolgreich ermittelt und anschließend zur Berechnung von Temperaturen in von Aerosolen beeinflussten Atmosphärenschichten genutzt. Die ermittelten Winde wurden mit den Daten des europäischen Zentrums für mittelfristige Wettervorhersage (ECMWF) und Messungen des Satelliten-Lidars Aeolus verglichen. Für einen Vergleich der ermittelten Rückstreukoeffizienten wurden Ergebnisse des WACCM-CARMA-Modells herangezogen und die ermittelten Temperaturen wurden mit ECMWF-Temperaturen und Lidarmessungen eines weiteren IAP-Lidars verglichen. Gute Übereinstimmungen unterstreichen die Effektivität der entwickelten Prozessierungsmethoden. Neu an den Ergebnissen dieser Arbeit ist die Vermessung der mittleren Atmosphäre mittels fünf Sichtfeldern, die Neuentwicklung der Prozessierungsmethoden, die Ermittlung von 3D-Winden zwischen 3 und 25 km allein mittels Aerosolrückstreuung, die hohe Sensitivität der Aerosolmessungen sowie die Bestimmung genauer Temperaturen mittels Rayleigh-Integration in der Anwesenheit von Aerosolen. Diese Erkenntnisse zeigen die Fähigkeiten des neuen Lidars mit MFOV-Erweiterung und werden bei künftigen Messkampagnen zum Einsatz kommen werden.

Contents

1 | Introduction

I well remember a brilliant red balloon which kept me completely happy for a whole afternoon, until, while I was playing, a clumsy movement allowed it to escape. Spellbound, I gazed after it as it drifted silently away, gently swaying, growing smaller and smaller until it was only a red point in a blue sky. At that moment I realized, for the first time, the vastness above us: a huge space without visible limits. It was an apparent void, full of secrets, exerting an inexplicable power over all the Earth's inhabitants. I believe that many people, consciously or unconsciously, have been filled with awe by the immensity of the atmosphere. All our knowledge about the air, gathered over hundreds of years, has not diminished this feeling.

– Theo Löbsack, *1963*

1.1 Background and Motivation

The atmosphere of our Earth is a complex, dynamic system with numerous physical processes occurring simultaneously. According to Lorenz (1955), the most important variables of the atmospheric system are the five physical quantities of pressure, temperature, humidity, wind, and density. These five quantities interact in complex ways to shape the Earth's weather and climate system. They are influenced primarily by the distribution of solar radiation, which varies with latitude and drives global circulation patterns. Additionally, the Coriolis effect, resulting from the Earth's rotation, introduces a fundamental asymmetry in atmospheric motion, leading to the formation of prevailing zonal wind patterns. Interactions between the atmosphere and other components of the Earth system, such as the oceans and land surfaces, also play a crucial role in determining weather patterns and climate variability. Beyond these fundamental drivers, the atmosphere is also influenced by various mechanisms of more intricate nature, like gravity waves, planetary waves and tides. Gravity waves are buoyancy driven oscillations which propagate through Earth's atmosphere (and oceans) (e.g., Fritts and Alexander, 2003; Nappo, 2013). They are generated by factors such as topography, convection, and wind shear and play a crucial role in transferring energy and momentum vertically and horizontally within the atmosphere. These waves contribute to a range of atmospheric phenomena, from influencing local weather patterns to impacting global climate dynamics. A well-known example of this is the cold summer mesopause at high latitudes, where gravity waves drive the temperature 100 K away from radiative equilibrium. Understanding the interplay between basic

atmospheric drivers and more nuanced processes like gravity waves is key to comprehensively understanding atmospheric dynamics.

In order to gain a complete understanding of the atmospheric system, it is essential to accurately observe key physical quantities with sufficient resolution and coverage, both in terms of space and time. Remote sensing instruments such as lidar and radar provide measurements of wind and temperature across extensive altitude ranges. These technologies offer continuous coverage with high precision, though they are typically limited to a single fixed location. Radar systems are capable of measuring horizontal winds in the troposphere and lower stratosphere, reaching up to approximately 20 km, and in the mesosphere / lower thermosphere above ∼80 km (Hocking, 2011). Lidar systems can provide temperature measurements from the tropospheric boundary layer up to the mesosphere or even higher, if resonance scattering is used. Coherent detection technology in smaller wind lidars enables horizontal wind measurements within the troposphere, while larger Doppler-Wind lidars can assess wind patterns up to mesospheric altitudes. A significant observational challenge that remains is the precise measurement of three-dimensional winds, especially in the stratosphere and mesosphere. The vertical wind component, often of low magnitude, is particularly difficult to measure but is crucial for enhancing our understanding of transient atmospheric phenomena, such as gravity waves.

Ground-based remote sensing instruments, though invaluable for data collection at specific locations, face limitations in capturing horizontal atmospheric scales. Traditionally, this gap has been filled by space-borne instruments, such as satellites. Satellites are adept at providing global measurements, but their orbital patterns and measurement techniques result in limited temporal and spacial resolution compared to ground based observations (Wing et al., 2018). Consequently, their typically coarse horizontal and vertical resolution and infrequent measurements hinder their effectiveness in monitoring transient atmospheric phenomena. Specifically, in the study of gravity waves, current satellites struggle to resolve waves with horizontal wavelengths shorter than 100 km or intrinsic periods under 120 minutes, as discussed in Lübken and Höffner (2021). Given the anticipated absence of significant advancements in satellite coverage or resolution in the foreseeable future, a dense network of ground-based remote sensing instruments emerges as the primary method to acquire the necessary data. Furthermore, the ground-up measurements from such a network offer a complementary perspective to the top-down approach employed by space-borne instruments. This synergistic integration of continuous, Eulerian-frame ground measurements with the temporally scattered, yet global satellite data promises to significantly enhance our understanding of atmospheric dynamics. For the effective deployment of such a network, instruments need to be versatile in measuring diverse atmospheric parameters, capable of autonomous operation with minimal maintenance requirements, and cost-efficient. Furthermore, it is essential to establish and adhere to standards for both measurement technology and data processing protocols. In line with the VAHCOLI (**V**ertical **A**nd **H**orizontal **CO**verage by **LI**dar) concept, the Leibniz Institute of Atmospheric Physics has developed a lidar system specifically designed for network applications, striving to meet these standards.

1.2 Overview of the VAHCOLI Lidar System

The VAHCOLI systems have been designed as compact and mobile lidar instruments, suitable for Doppler-Mie, Doppler-Rayleigh, and Doppler-resonance measurements. This means that the systems are capable of measuring wind, temperature, and other atmospheric parameters based on the light backscattered on aerosols (Mie), molecules (Rayleigh) and potassium vapour (resonance). The systems feature a custom-developed diode-pumped alexandrite ring laser as the emission source, paired with a compact receiver. The receiver employs a narrowband planar etalon (FWHM ≈900 MHz) and an ultra-narrowband confocal etalon (FWHM ≈7 MHz) for measurement filtering. The operational principle is based on the frequency scanning of the power laser across the stabilized filters, facilitating high-resolution spectroscopy of the backscattered signal. As detailed in chapter 3.4, this technique enables the systems to perform atmospheric measurements of wind, temperature, and aerosol parameters across an extensive altitude range, from 10 km to 100 km. This is achieved through a singular measurement approach targeting different scattering processes, allowing for a streamlined optical setup with fewer optical components compared to alternative methods. The design, employing additive manufacturing, supports efficient assembly and deployment. These design choices render the VAHCOLI systems suitable for network applications, aimed at extensive atmospheric monitoring.

The foundational measurement principle of the VAHCOLI systems is derived from the mobile potassium and iron lidars developed by the IAP, but both the measurement concept and hardware have undergone significant enhancements to achieve the compact design of the VAHCOLI systems (von Zahn and Höffner, 1996; Fricke-Begemann et al., 2002; Höffner and Lübken, 2007). In these systems, all essential optical and mechanical components are housed within a compact structure, which is made possible by employing 3D printing as the primary manufacturing technique. Using custom printed components, tailored specifically towards the needs of the instrument, for the housing, the optical system and in various other places, results in the lightweight, compact system. The alexandrite ring-laser is intricately integrated both optically and electronically into the measurement framework. The system's architecture ensures a high level of integration, encompassing the laser control, optical components, and all electronics required for data acquisition, processing, and storage. A singular computer manages these components, allowing for a seamless interconnection of all critical operational processes, thus enhancing the system's efficiency and capability in instrument control and atmospheric data collection. The incorporation of fast measurement cards enables the precise assessment of each laser pulse, capturing its temporal form, exact firing time, and frequency, alongside the altitude-resolved atmospheric backscatter sampled with a resolution of 1 meter. Furthermore, a close integration of electronics, mechanics, and software facilitates innovative methods for instrument control and the derivation of system and atmospheric properties during operation. This integrated approach significantly surpasses the capabilities of lidars with more conventional designs in terms of operational efficiency and data accuracy.

In addition to the laser, the detection bench, a 50 cm mirror telescope, the control PC and all additional electronics required for the lidar measurements, the housing includes all necessary features for fully autonomous operation such as an automated hatch, cooling, laser and air safety measures, a weather station and more. The temperature sensitive com-

ponents like the detection bench and the laser have their own compartments, away from electronics with high or strongly variable power consumptions. This leads to a temperature stability of 0.1 K in the crucial compartments.
The very first prototype of these systems, called VAHCOLI 0 was constructed in 2019, prior to the developments and results presented in this thesis. This system, shown in Figure 1.1, utilized a single vertical pointing 50 cm telescope, and passive cooling and was used to do the very first measurements with such a compact system. Even though there were significant deficiencies in signal strength and performance during summer days, the system showed the general feasibility of the concept as reported in Froh (2021) and Lübken and Höffner (2021). The improved systems, designated VAHCOLI 1 and VAHCOLI 2, were constructed in 2021 and 2022, respectively, and were employed in this thesis, utilising the presented developments and advancements.

Figure 1.1. Image of the VAHCOLI 0 prototype system during a daylight measurement in 2020 on the test range in Kühlungsborn, Germany. The Prototype system features a small volume of one cubic meter, a weight of 250 kg and is designed for a power usage of 500 W. It uses a single 50 cm telescope and is thus limited to vertical measurements. On the front left edge of the system, the passive cooling solution is visible.

1.3 Research Objectives

With the initial feasibility of the general concept of a universal Doppler-Mie, Doppler-Rayleigh, Doppler-resonance lidar shown with the VAHCOLI 0 prototype, this research aims to significantly advance the capabilities of the VAHCOLI instruments, particularly in the measurement of three-dimensional winds and temperatures. The focuses of this thesis

is set on the altitude range between 3 and 25 km for three-dimensional wind measurements and between approximately 10 and 40 km for temperature measurements. However, the instruments are designed to cover the whole middle atmosphere from 10 to 100 km. The enhancement of the VAHCOLI instrument to capture accurate 3D wind dynamics is a pivotal development in atmospheric sciences, facilitating a deeper understanding of atmospheric processes and contributing to improved accuracy in weather forecasting.
A crucial objective of this development is the capability to observe horizontal scales in the transition region from microscale to mesoscale, ranging from approximately 1 km to several tens of kilometres, using a single instrument. Consistent with the VAHCOLI concept, effectively covering these scales is essential, given their significant impact on the observation of transient atmospheric phenomena such as gravity waves and stratified turbulence[1].
In alignment with these objectives, the research includes the development of a Multi Field of View (MFOV) upgrade for the VAHCOLI systems. This enhancement is designed with the network application of the systems as a central consideration, striving to maintain the instrument's mobility and simplicity. Additionally, cost efficiency is a critical factor in the design process. The MFOV upgrade facilitates a broader and more detailed acquisition of atmospheric data, consistent with the primary goal of comprehensive atmospheric monitoring. Similar to the spectral capabilities, a key aim is the system's flexibility, as the number of fields of view (FOV) is determined by software settings and can be adjusted to meet specific scientific needs without physical modifications to the system. The division of the FOV into sub-FOVs is achievable through minor adjustments in the angle of the optical axis via the telescopes, enabling coverage of the smallest horizontal scales.
The paramount goal of this research is to establish a robust pipeline for processing the raw data obtained from the VAHCOLI systems. The processing pipeline is an essential component of the project, enabling the precise derivation of detailed wind profiles, aerosol parameters and temperature data from the raw lidar measurements. This is of great importance for the practical application and scientific contribution of the VAHCOLI systems within the fields of atmospheric research and meteorology. Although this thesis focuses primarily on the development of the necessary analytical methods, the ultimate objective is to achieve a fully automated data analysis system capable of efficiently handling the vast volumes of data produced by a network of instruments.
Following these objectives, the structure of this thesis is as follows: Chapter 2 outlines the required theoretical foundations of atmospheric physics, emphasizing atmospheric scales, lidar principles, and scattering processes, crucial for advancing the VAHCOLI systems' atmospheric observation capabilities. Chapter 3 provides a comprehensive summary of the current state of middle atmosphere wind lidars. It explores various Doppler-lidar methodologies and offers an in-depth analysis of the VAHCOLI measurement technique. Chapter 4 details the development process of the MFOV upgrade, along with additional enhancements made to the system. In Chapter 5, the newly developed pipeline for wind measurements is described. This chapter also presents wind measurement results, compares them with satellite data and model predictions, and underscores the system's proficiency in observing horizontal wind field gradients. Chapter 6 outlines the approach for extracting

[1] The theory of stratified turbulence describes three-dimensional turbulence with significantly constrained vertical motion in highly stratified flows (Billant and Chomaz, 2001; Lindborg, 2006).

aerosol properties from VAHCOLI measurements and presents findings from this method. Chapter 7 is dedicated to the retrieval and analysis of temperature data from the measurements. Chapter 8 discusses the implications of the findings presented in the preceding chapters. Finally, Chapter 9 gives a conclusion of the research findings and offers a perspective on potential future developments in this field.

2 | Theoretical Background

2.1 Scales of Relevant Atmospheric Effects

Atmospheric dynamics cover a broad spectrum of scales, each significantly influencing weather patterns, climate variability, and atmospheric phenomena. From small eddies to vast patterns of global circulation, these scales engage in complex interactions, propelling the dynamic nature of the atmosphere. Interactions of different scale atmospheric effects are not limited to a single atmospheric layer, but can span altitude ranges from the troposphere to the mesosphere and beyond, leading to the vertical coupling of the atmosphere. The varying horizontal scales are generally distinguished by their typical temporal and spatial extent, grounded in the notion that a scale separation exists among different phenomena (Fiedler and Panofsky, 1970; Klein, 2010).

At the microscale, atmospheric processes manifest at a highly localized level, where phenomena like turbulence and individual cloud formations exert significant influence. Especially turbulence plays an important role in the energy budget of Earth's middle atmosphere, where it transfers energy from large scales into smaller scales. The scales on which turbulence occurs depend strongly on the observed altitude range. While in the troposphere, the typical length scale is on the order of centimetres (see Section 4.3.1), in altitudes of 60-110 km effects occurring on length scales smaller than $\approx$100 m are considered turbulent (Poblet et al., 2023).

Broadening our perspective to the mesoscale, we observe atmospheric phenomena that extend across tens to hundreds of kilometers. This scale encompasses a variety of phenomena, including thunderstorms, mesoscale convective systems, and sea breezes, each playing a pivotal role in shaping regional weather patterns and the distribution of precipitation. As discussed in Poblet et al. (2022), mesoscale dynamics also vary drastically with the observed altitude, making it necessary to observe them over a wide range of altitudes.

On the synoptic scale, large-scale features in the order of few 1000 km and more dominate. High and low-pressure systems, jet streams, and weather fronts characterize this scale, steering global circulation patterns and influencing long-term weather trends. The dynamics at the synoptic scale serve as the cornerstone for weather forecasting models and offer valuable insights into the overarching climate system.

At the planetary scale, the atmosphere unveils its global interconnectedness through phenomena such as the El Niño-Southern Oscillation (ENSO), the North Atlantic Oscillation (NAO) and the Quasi-Biannual Oscillation (QBO), which wield influence over extensive spatial areas. Dynamics at this scale surpass regional confines, affecting weather variability and climate conditions worldwide. Climatologists meticulously examine these

phenomena, aiming to decipher their underlying mechanisms and their repercussions on climate variability and change (Roedel and Wagner, 2011).
However, an examination of atmospheric scales would be incomplete without addressing the middle atmosphere, particularly the upper stratosphere and lower mesosphere. In this region, planetary waves, atmospheric tides and gravity waves are of critical importance, affecting temperature distributions, wind patterns, and chemical compositions. Planetary waves, including Rossby and Kelvin waves, propagate both horizontally and vertically, influencing stratospheric variability and facilitating the interaction between different atmospheric layers. Gravity waves, originating from a variety of sources, play a key role in the transport of momentum and energy, thereby affecting turbulence, atmospheric stability, and processes within the mesosphere. As previously mentioned, in these altitudes dynamical effects can drive the temperature drastically (up to 100 K) away from the radiative equilibriums.
The interaction of the different scales shape the dynamics in all atmospheric layers, and thus an observational coverage of the scales is required over a large altitude range to see the full picture. Here, the large variety of scales in the atmosphere, provides a challenge for the observational atmosphere physicist. As discussed already in the introduction, space born instruments struggle with resolving all of them, especially when it comes to the shorter scales. This leaves a need to provide the vertical and horizontal coverage for future studies with ground based instruments such as lidar (Lübken and Höffner, 2021).

2.2 Basic Principles of Atmospheric Lidar Measurements

The abbreviation lidar stands, in reference to radar, for light detection and ranging. The roots of modern lidar systems can be traced back to the end of the 19th and the beginning of the 20th century. Already in 1887 O. Jesse suggested a (purely geometric) method to determine the altitude of noctilucent clouds using a ray of intense, parallel, electric light (Jesse, 1887). In 1917 Albert Einstein then laid the theoretical foundation for laser light with his work on the quantum theory of radiation (Einstein, 1917). In 1930 Edward Hutchinson Synge came up with an idea how to use the large quantities of searchlights for atmospheric measurements, which were collecting dust in military depots in the inter war period. He envisaged an array of hundreds of searchlights illuminating the sky and a single large mirror focussing the light backscattered by the air molecules on a photoelectric detector (Synge, 1930). Such an assembly he estimated to be sufficient to do density measurements up to 50km altitude, even though he stated that probably “the method would only have an abstract scientific interest” since fluctuations in these altitudes are not directly connected to weather. In 1937 first measurements were realised by the US Naval Research Laboratory under the lead of Edward Olson Hulburt reaching altitudes of 28 km with just one 12 inch searchlight (Hulburt, 1937). Two years later Ellis A. Johnson was able to capture signals up to 40 km using this method and showed that it can be extended to allow measurements up to heights of 70 to 90 km and to determine the distribution of ozone at low altitudes (Johnson et al., 1939). Einstein’s theoretical description of stimulated emission was first validated in 1953 at the Columbia University, when a team around Charles Townes successfully realised the first microwave amplification by stimulated emisson of radiation or

abbreviated MASER (Gordon et al., 1955). In 1960 Theodore Maiman demonstrates the very first laser, based on a flashlamp pumped ruby crystal, emitting on 694.3 nm (Maiman, 1960). This proved to be a real breakthrough in the development of lidar technology, due to the coherent and monochromatic laser light allowing for the usage of spectral filtering to analyse the backscattered light. In the same way as laser technology was pushed rapidly into many scientific fields, in 1963 Fiocco and Smullins reported the first successful atmospheric soundings in the upper atmosphere, with echoes from maximum altitudes between 80 km and 140 km (Fiocco and Smullin, 1963). In the following decade the most important lidar techniques like elastic scattering lidar, Raman scattering lidar, different absorption lidar and Doppler-lidar were successfully demonstrated using lasers (Measures, 1984).
The three fundamental steps of lidar operation, which have been present in all modern lidar systems since then, have remained consistent. The first step is the transmission of a laser pulse into the atmosphere with a well known timing. This can either be done without any beam widening, directly out of the laser, or through a beam widening telescope. The second step is the interaction of the emitted laser photons with a scatterer in the atmosphere. This can be the either be molecules, like nitrogen (N_2), aerosol or dust particles, or individual atoms, like potassium (K), which is present as vapour due to the ablation of meteors in the upper atmosphere, with a peak around 90 km. These particles cause the photons to be scattered in all directions. In the third step, the photons which are scattered in the backwards direction are focussed onto a photodetector by a receiver telescope and a varying degree of other optics, like polarisers and filters, which allow for daylight suppression or spectral analysis. From the time resolved electrical signal of the detector the time of flight t of the photons can then be calculated and converted into a range r, or, in the case of a vertically pointing telescope and laser beam, an altitude z using the speed of light c, so that $r = c \cdot t/2$. Figure 2.1 shows these three steps of lidar oparation based on a simple monostatic configuration, in which the laser is emitted coaxially to the receiving telescope.
The range dependent signal (or power) $P(r)$ on the photodetector of a lidar is often described by the so-called lidar equation.

$$P(\lambda, r) = P_0 \cdot C_{sys}(r) \cdot r^{-2} \cdot \beta_{tot}(\lambda, r) \cdot \tau_1(\lambda, r) \cdot \tau_2(\lambda, r) + \mathcal{B}(\lambda) \tag{2.1}$$

Wheras P_0 is the transmitted power, C_{sys} is the instruments' system constant, $\beta_{tot}(\lambda, r)$ is the combined backscatter coefficient of all scattering processes, $\tau_1(\lambda, r)$ and $\tau_2(\lambda, r)$ are the respective atmospheric one way transmissions to the scatterer and back. $\mathcal{B}(\lambda)$ is the background signal caused by the dark count rate of the instrument and the scattering of other radiation in the atmosphere, mostly sunlight. Both backscatter coefficient and transmission are dependent on the wavelength of the laser light and the backscattered light. For the instruments' system constant, one typically considers the area of the telescope A, the system efficiency Γ and the range dependent overlap function $\mathcal{O}(r)$ of the laser beam and the telescope's field of view (FOV).

$$C_{sys}(r) = A \cdot \Gamma \cdot \mathcal{O}(r) \tag{2.2}$$

The defocus effect of the telescope is often not considered in the overlap function, but, as shown in Chapter 4.3, is equally important. The different scattering types which need

to be considered for the combined backscatter coefficient depend on the observed altitude range and the filtering used in the instrument. A lidar without any spectral filter operating in the upper troposphere, lower stratosphere (UTLS) will measure signals from Mie-, Rayleigh- and Raman-scattering, while a mesospheric lidar will pick up echoes from Rayleigh-, Mie- and resonance-scattering (Fernald, 1984; Measures, 1984). The scattering processes commonly utilised for measurements from upper troposphere to the mesosphere will be discussed in the following section.

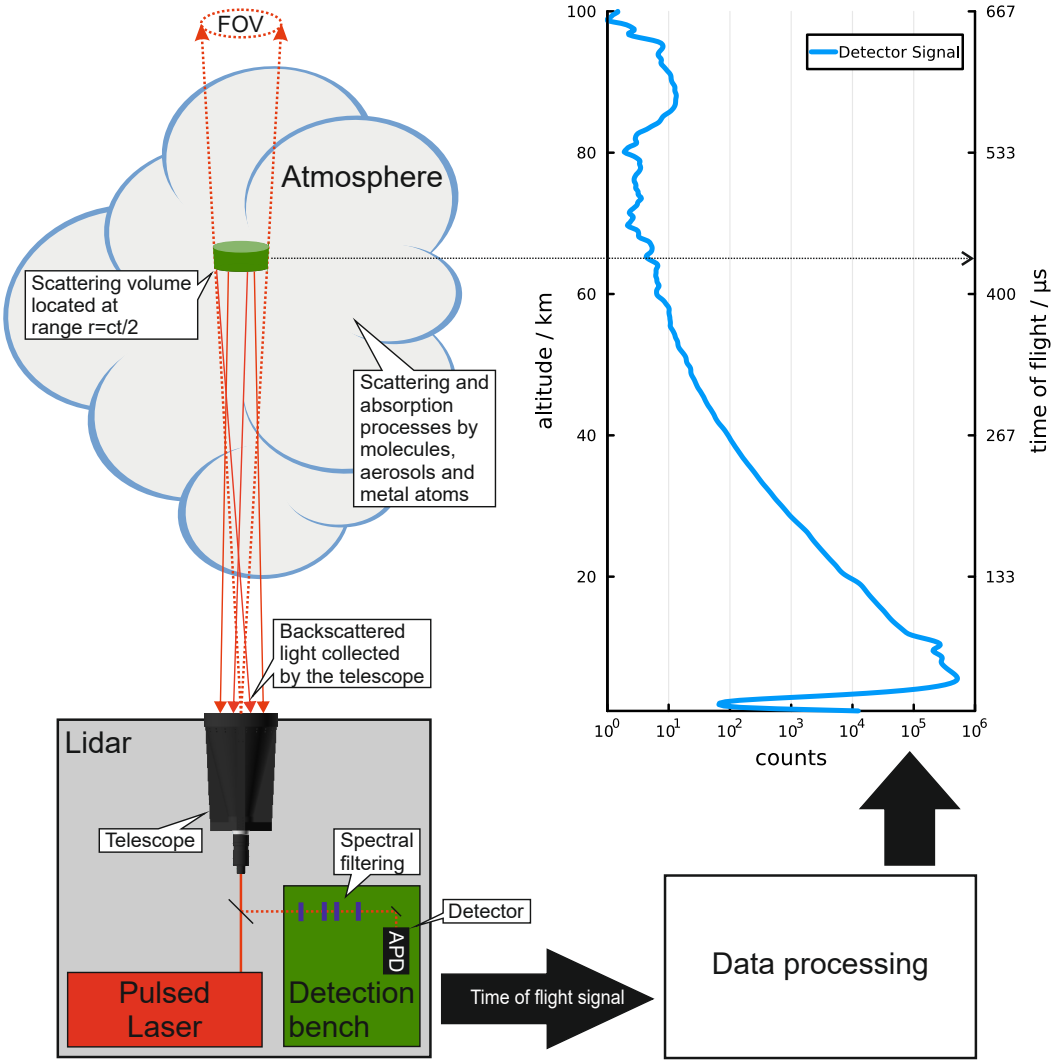

Figure 2.1. Overview showing the operation principle of a lidar. The emission part of the schematic lidar, positioned on the bottom left side (red), produces a laser pulse which is transmitted into the atmosphere (top left), coaxially to the receiver telescope. The pulse travels through the atmosphere in the field of view of the telescope and is scattered. The receiver telescope collects the backscattered photons and focusses them on into the detection bench (green). In the detection bench, the photons are analysed using various filters and finally directed to a detector. The time resolved signal of the detector is then processed and converted into atmospheric parameters in dependence of altitude (top right), in this case an exemplary measurement of VAHCOLI 1.

2.3 Properties of Different Scattering Processes

Rayleigh-scattering

Rayleigh scattering, named after Lord Rayleigh, who developed this theory in the late 19th century to explain the blue colour of the sky, describes the scattering of an electromagnetic wave on an object, which is much smaller than the wavelength of the scattered wave (Rayleigh, 1899; Young, 1982). Within this limitation of very small scattering particles, Rayleigh was able to find an approximate solution to Maxwell's equations. A more general solution was later found by Gustav Mie (see next section). With the largest constituent in the atmosphere being molecular nitrogen at a size of 0.37 nm and typical lidar wavelength in the optical range or close to it (Nd:YAG 1064 nm,532 nm and 355 nm; Alexandrite 700-800 nm), it is one of the most prominent scattering processes in lidar observation and often called molecular scattering (Mehio et al., 2014). The important property for lidar is the backscatter cross section of Rayleigh scattering. According to the Rayleigh theory the differential scattering cross sections for vertical (VV) and horizontal polarisation (HH) are (Hahn, 2009):

$$\sigma'_{VV}(\lambda) = \frac{\lambda^2}{4\pi^3} \cdot \alpha^6 \left(\frac{m^2 - 1}{m^2 + 2} \right)^2 \tag{2.3}$$

$$\sigma'_{HH}(\lambda) = \sigma'_{VV} \cdot \cos^2(\theta) \tag{2.4}$$

with m the index of refraction of the scatterer. α is the so called the size parameter which is defined as:

$$\alpha = \frac{2\pi a m_0}{\lambda} \tag{2.5}$$

Here a is the spherical diameter of the particle and m_0 is the refractive index of the surrounding medium. For the backscattering with an angle of $\theta = \pi$, we thus get the polarisation independent differential backscatter cross-section:

$$\sigma'_{\pi}(\lambda) = \frac{\lambda^2}{4\pi^3} \cdot \alpha^6 \left(\frac{m^2 - 1}{m^2 + 2} \right)^2 \tag{2.6}$$

From Equation 2.3 and 2.4 follows, that the polarisation is conserved. A property which can be used in lidars (see Section 3.4). Using the values for the mixture of gases found in dry air, which occurs below 100 km this ultimately leads to (Measures, 1984):

$$\sigma^R_{\pi}(\lambda) = 5.45 \left(\frac{550}{\lambda} \right)^4 \times 10^{-32} \mathrm{m}^{-1} \mathrm{sr}^{-1} \mathrm{nm}^{-4} \tag{2.7}$$

In the middle atmosphere (above 10 km) the scattering is considered elastic, with the wavelength of the light being the same before and after the scattering process, except for the Doppler shift imprinted on the photons due to the movement of the molecules. Due to the small size and low mass of the molecules, the Doppler-broadening from thermal motion is significant. For an alexandrite laser operating at 770 nm it is in the order of 1.5 GHz at a temperature of 200 K with a Gaussian spectrum, as visible in Figure 2.2. In the troposphere where the mean free path length of the individual molecules becomes short, one has to also consider an inelastic scattering component when describing the spectral shape

of the backscattered light, which is due to the influence of scattering on acoustic waves in the atmosphere. This leads to an additional doublet occurring left and right to the mean peak, the so called Cabannes lines. The scattering is then considered Rayleigh-Brillouin scattering, after Leon Brillouin who described the effect in 1922. The strength of the doublet peaks is dependent on the ratio y of the scattering wavelength to the mean path of collisions

$$y = \frac{\lambda n k_B T}{2\pi v_0 \eta} \tag{2.8}$$

with n the number density, k_B the Bolzmann constant, T the temperature, v_0 the most probable thermal velocity and η the shear viscosity. For typical atmospheric conditions in 15 km altitude this gives a value of approximately $y \approx 0.1$ and thus the influence of Brilloin-scattering on the spectral shape can be neglected for $z > 15$ km as visible from Figure 2.2. Due to the exponential decrease of the atmospheric density with altitude, this statement is true for the whole middle atmosphere (Measures, 1984; Hahn, 2009; Witschas, 2012; Tenti et al., 1974).
Lidar observations using Rayleigh scattering can be done to high altitudes, but due to the mentioned exponential decrease in molecular number density in the atmosphere, more and more technical effort is necessary when pushing for higher altitudes. Nevertheless, atmospheric studies using Rayleigh scattering are possible to altitude in the range of 100 km (Wing et al., 2020).

Mie-scattering

Mie-scattering named after Gustav Mie, who came up with the theory in the early 20th century, is often associated with the scattering on spherical dust and aerosols particles (Mie, 1908). While the theory strictly speaking has no size limitations and is thus also applicable to the Rayleigh regime, this is almost never done, due to its much higher complexity. Thus also in this thesis, Mie-scattering is used synonymously for scattering on dust and aerosol particles with a size close to the laser source wavelength (sulfate aerosols $\approx$ 100 nm, noctilucent clouds $\approx$20 nm). A brief introduction into the calculation of backscatter cross-sections using Mie theory, as done for Rayleigh theory, is beyond the scope of this section due to its complexity. In general the cross-section of Mie-scattering is strongly dependent on the particles size and shape, and their refractive index. Aerosols in the middle atmosphere vary strongly in these parameters and thus scattering cross-sections are mostly described on numerical models which include the statistical distribution of these parameters. Typical values of the backscatter cross-section for middle atmosphere aerosols are in the order of 10^{-21} m^2/sr, while number densities are typically below 10 cm^{-3} in the stratospheric Junge layer of sulphate aerosols (McCormick et al., 1968; Deshler, 2008). In general the vertical structure of aerosol density is highly variable with the common occurrence of layering. The Junge layer mentioned above typically extends up to 25 kilometres. Above this, the aerosol density drops sharply. In summer aerosols in the form of ice crystals can be observed in the mesopause region at heights between 80 and 90 km, which form so called noctilucent clouds. In these clouds, Mie scattering can exceed Rayleigh scattering by orders of magnitude.
Mie-scattering is a form of elastic scattering introducing no frequency shift to the scattered

light exept the Doppler-broadening and -shift due to the movement of the particles. The Doppler-broadening of Mie-scattering is very weak, due to the high weight of the individual particles. The broadening for typical particle sizes in the middle atmosphere is in the order of a few 100 kHz and thus close to negligible, when compared to the broadening of Rayleigh scattering as shown in Figure 2.2. Since Mie-scattering and Rayleigh-scattering are both elastic and thus occur on the same frequencies, it is difficult for lidar instruments to separate the two scattering processes. The VAHCOLI instruments use optical splitting on ultra-narrowband filters, as explained in more detail in Section 3.4, to detect the spectrally sharp Mie peak on the broader Rayleigh background. Furthermore, VAHCOLI can resolve spectral features that are below the linewidth of the laser and receiver by utilizing Mie-scattering. Although no significant Doppler broadening occurs during the scattering on aerosols in the stratosphere due to the high mass of the particles, random motion within the observation volume, such as turbulence, introduces additional broadening which can be detected and used for atmospheric studies with VAHCOLI. For other instruments like middle atmosphere temperature lidars, which use Rayleigh scattering for temperature measurements (see Chapter 7), and don't use ultra narrowband filters the additional aerosol scattering causes significant problems in the temperature retrieval in the presence of aerosols, which is why in these altitudes Raman-scattering is often used to retrieve temperatures (Flamant, 2005; Witschas, 2012).

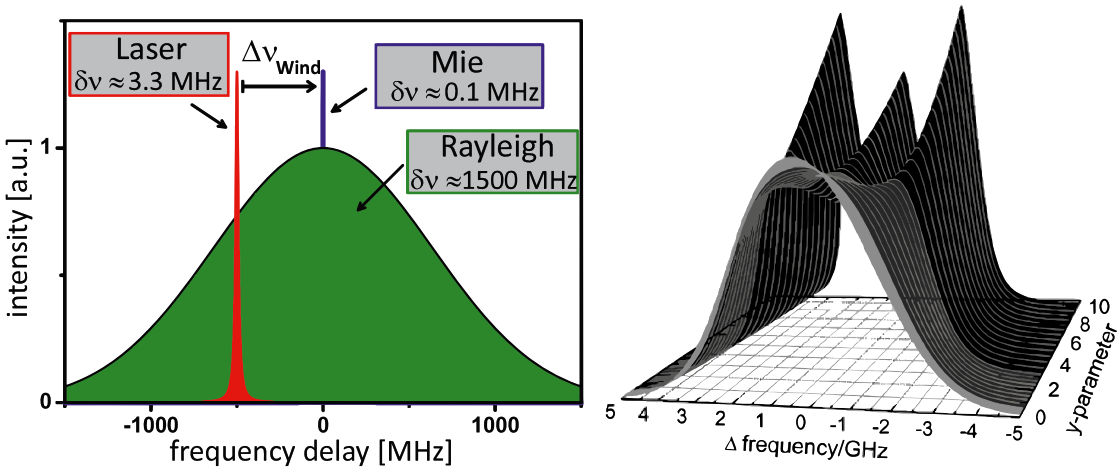

Figure 2.2. **left:** Schematic representation of the spectra when the laser is scattered by molecules (Rayleigh-scattering, green) and aerosols (Mie-scattering). The laser with a spectral with of 3.3 MHz is Doppler-shifted due to the wind in the atmosphere and then Doppler-broadened by ≈0.1 MHz when scattered on aerosols and by ≈1500 MHz when scattered on molecules. Adapted from (Froh et al., 2022). **right:** Evolution of the Rayleigh-Brillouin scattering at 355 nm for different values of the y-ratio. Middle atmospheric values are highlighted in light grey, where a Gaussian shape can be assumed, typical tropospheric values are shown in dark gray and black values are only found in laboratory experiments. Adapted from (Witschas, 2012).

Raman-scattering

Raman scattering is a form of inelastic scattering which occurs on molecules and was first discovered and described by the Indian physicists Chandrasekhara Raman and Kariamanickam Krishnan in the early 20th century (Raman and Krishnan, 1928). It is caused by a photon being scattered on a molecule, which simultaneously changes its rotational or vibrational energy level. If the scattered photons energy is transferred to the molecule and thus is reduced in frequency (red-shifted) this process is also called Stokes scattering. If instead energy from a rotational or vibrational state of the molecule is transferred to the photon, increasing its frequency (blue-shifted), it's called anti-Stokes scattering. The frequency shift of the scattered photon corresponds to the required energy to change the energy level of the molecule, and is thus dependent on the energy levels in the molecular species.
The differential backscattering cross-section of Raman-scattering is typically several orders of magnitude below the one of Rayleigh scattering, as shown on the left side of Figure 2.3. Spectrally, the individual Raman peaks are also significantly broader than Rayleigh-scattering. This combination of properties are a disadvantage for lidar application, since measurements are highly sensitive to the background, due to the low signal, and a narrowband filtering is not possible to remove the solar background efficient enough, which limits the system nighttime operations in the stratosphere and above. In the troposphere up to altitudes of 6 km, high power lidar systems are still able to do daylight Raman measurements (Martucci et al., 2021). The benefit of the Raman-scattering is the introduced frequency shift. Since the photons backscattered by Raman-scattering are not on the same frequency as the Mie scattering, they can be used to retrieve temperatures in the presence of aerosol, with the right filter setup in the receiver (Measures, 1984; von Zahn et al., 2000; Witschas, 2012).

Resonance-scattering

Resonance scattering is an inelastic scattering process in which a photon of the right frequency is absorbed by an atom, raising the atoms electronic state. The atom then emits photons in the process of spontaneous emission on the same, or various other wavelengths. The backscattering cross-section of this process is strongly dependent on the element and the electronic transition which is exited. For the D1 transition of potassium at 769.9 nm the backscatter cross-section is $\sigma_{\pi}^{K} = 7 \cdot 10^{-17}$ m^2/sr and thus almost 16 orders of magnitude larger than the backscatter cross-section for Rayleigh scattering at the same frequency. This allows a lidar operating on the correct wavelength to detect already small quantities of atomic potassium in the atmosphere. Potassium is introduced into the atmosphere by the vaporisation of meteors entering the atmosphere at high speeds. In altitudes between 120 and 80 km they ablate and cause the mesospheric metal layer in which the most prominent elements are iron, potassium and sodium.
The spectral shape of the backscattered light is highly dependent on the atom's electronical structure. Each transition has a natural line width, which has the spectral form of a Lorenz function, and is Doppler broadened. Thus, the spectral shape of a single transition can be described with a Voigt function, which is the convolution of a Lorenz with a Gaussian function. The complete spectral shape is then given by superimposing the Voigt profile

for all electronic transitions. In the case of scattering on the D1 line of Potassium one has to consider 8 of these electronical transitions, caused by the isotopes and the hyperfine structure. Additionally, relaxation pathways need to be considered, which leads to light being emitted along 12 different wavelengths and the complex spectral shape shown in Figure 2.3 (von Zahn and Höffner, 1996; Friedman et al., 2003; Fricke-Begemann, 2004; Höffner and Lübken, 2007).

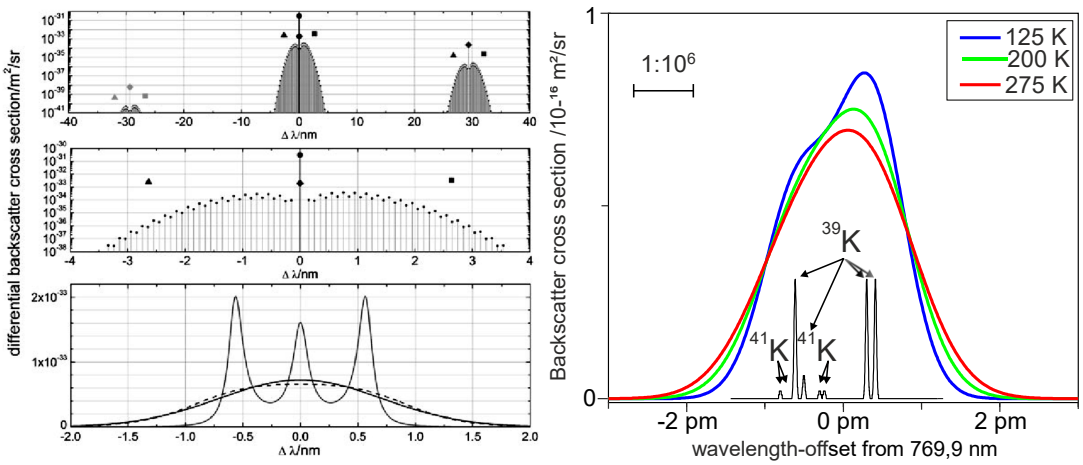

Figure 2.3. **left:** Simulated differential backscattering cross sections at 355 nm for scattering on N^2 with different resolutions. *Top* shows rotational and vibrational Raman-scattering. *Center* shows only the rotational Raman-scattering. *Bottom* shows the Rayleigh-Brillouin scattering. Symbols mark the integrated differential backscattering cross-sections for each band. Adapted from (Witschas, 2012). **right:** Spectral shape of resonance-scattering on potassium at 769.9 nm. Adapted from (von Zahn and Höffner, 1996).

3 | Middle Atmosphere Doppler Wind Lidars

3.1 Wind Measurement Techniques in the Middle Atmosphere

As discussed in Mense et al. (2024), accurate and comprehensive measurements of wind profiles play a critical role in various atmospheric studies and applications, including numerical weather prediction (NWP) (Baker et al., 2014; Stoffelen et al., 2005). However, obtaining such measurements presents significant challenges. In situ measurements using anemometers mounted on towers or masts are limited to the boundary layer, whereas wind measurements from radiosondes, aeroplanes, and rockets can only offer snapshots of the winds, lacking continuous coverage.

To achieve continuous wind measurements with a high degree of accuracy and spatiotemporal resolution, ground-based remote sensing methods are indispensable. Among the most prominent ground-based techniques for measuring wind are sodar, radar, and lidar. Sodar and radar are limited in their altitude coverage due to inherent technical constraints. Specifically, sodar wind profilers are capable of reaching heights of up to two kilometres through the scattering of sound waves off turbulence, as noted by Bailey (2000). Radar, on the other hand, can measure winds in the troposphere and in the upper mesosphere and lower thermosphere (MLT), facilitated by the presence of available scattering targets. Nonetheless, radar experiences a significant observational gap, unable to measure winds between altitudes of approximately 20 and 80 km (Hocking, 1997).

Ground-based Doppler-wind lidars (DWL) stand out as the sole remote sensing instruments capable of providing continuous wind profiles from the troposphere to the MLT, achieving high vertical and temporal resolution. Among existing DWL technologies, all primarily rely on Rayleigh scattering to bridge the observational gap identified for radars. An exception is the VAHCOLI instruments, which uniquely leverage Mie scattering in the lower part of this range to enhance measurement capabilities.

3.2 Existing Rayleigh Doppler-Wind Lidar Systems

As outlined in Section 2.3, Rayleigh scattering is traditionally identified as the only scattering mechanism effectively utilized in lidar technologies for the exploration of the middle atmosphere, covering altitudes between 30 and 80 km. The process involves the elastic

scattering of photons by atmospheric molecules, where the frequency of the light backscattered on a molecule may be altered due to the Doppler effect, as described by:

$$\Delta f = \frac{2 \cdot \Delta v}{c} f_0, \tag{3.1}$$

where Δf denotes the frequency shift, Δv represents the relative velocity between the laser emitter and the molecule along the line of sight, and f_0 is the emitted light's frequency. This scattering results in two spectral phenomena when an ensemble of molecules in the form of an air parcel is observed by lidar: a Doppler shift from the parcel's collective motion and a Doppler broadening from the thermal motion of individual molecules. The mean velocity of these molecules, following a Maxwell-Boltzmann distribution, is given by:

$$\overline{v}_T = \sqrt{\frac{8 \cdot k_B \cdot T}{\pi \cdot m}}, \tag{3.2}$$

with k_B as the Boltzmann constant, T the temperature, and m the molecular mass. Consequently, the Doppler broadening of the scattered spectrum, expressed as the full width at half maximum (FWHM), is:

$$\Delta \overline{f}_T = \frac{2 \cdot f_0}{c} \sqrt{\frac{8 \cdot k_B \cdot T \cdot \ln 2}{m}}, \tag{3.3}$$

highlighting the lidar's need to discern a Doppler-shift within a distribution approximately 692 times broader than the shift itself for accurately measuring wind speeds of 1 ms^{-1} at a temperature of 300 K.
Currently there are only six operational Rayleigh Doppler-wind lidars in the world which achieve this precision or come even close to it, in middle atmospheric altitudes. These systems and their measurement methods will be briefly discussed in the next sections.

Observatoire de Haute Provence (OHP)

Located in the southeast of France, the Doppler wind lidar at the Observatoire de Haute-Provence (OHP) began operation in 1989, making it the longest operating middle atmosphere Rayleigh Doppler wind lidar still in use today. Since its inception, the system has undergone several modifications (Chanin et al., 1989; Souprayen et al., 1999b,a). As detailed by Khaykin et al. (2020), the current configuration of the instrument comprises three sets of telescopes, each equipped with four 50 cm telescopes. One set is oriented vertically (zenithal), while the other two are angled 40° off zenith toward the north and east. The lidar's transmitter is a Quanta-Ray Pro290 Q-switched, injection-seeded Nd:YAG laser that emits at a 532 nm with a 30 Hz repetition rate and an energy output of 800 mJ per pulse. To detect the Doppler shift in the backscattered light, the system employs a double-edge Fabry–Pérot interferometer (FPI). The detection bench channels the collected light along two distinct paths through the FPI, which differ slightly in plate distances, thereby creating two bandpass filters with frequency shifts as illustrated in Figure 3.1. This design aims to optimize signal strength while minimizing the impact of Mie scattering, which could significantly affect wind measurement accuracy (Garnier and Chanin, 1992). The ratio of

the signals from the two channels is converted via a calibration curve into the Doppler shift, thus determining the line of sight wind.
The system operates only at night since no daylight suppression is available. During the measurement the beam is switched between the individual fields of view over the course of 5 minutes, with 1 minute of vertical measurement followed by 2 minutes of measurement each in the north and east field of view. The vertical pointing is used to calibrate the zero wind position of the FPI under the assumption, that vertical winds are negligible, since no absolute frequency measurement of laser and backscattered light is done. The system is capable to measure winds between 5 and 75 km altitude with a random error of less than 6 ms^{-1} as shown by the most recent validation campaign (Khaykin et al., 2020).

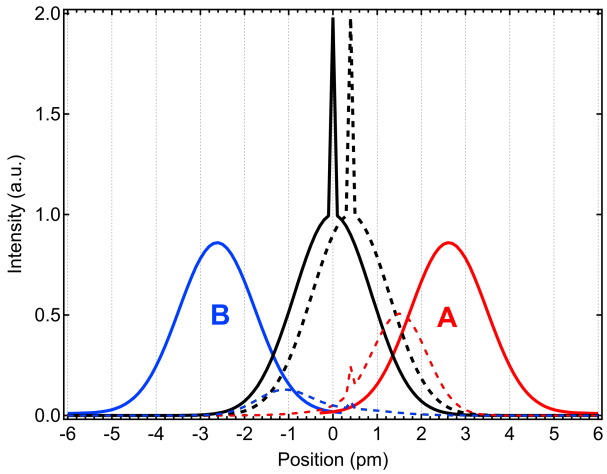

Figure 3.1. The thermally broadened Rayleigh backscatter line and a Mie line (solid black), with FPI A and B bandpasses (solid red and blue) as used for the OHP Doppler-wind lidar. A hypothetical Doppler-shifted backscatter line for a wind speed of 175 m/s is shown as a dashed black curve, with its transmission through A and B bandpasses illustrated by dashed red and blue curves, respectively (Khaykin et al., 2020).

Arctic Lidar Observatory for Middle Atmosphere Research (ALOMAR)

Constructed in 1994 atop the Ramnan mountain on Andøya island, Norway, and following five years after OHP's initiation, the ALOMAR Rayleigh-Mie-Raman (RMR) lidar employs dual lasers emitting at 1064, 532, and 355 nm, alongside two variable-pointing telescopes connected to a singular 17-channel detection bench via optical fibers (Fiedler and Baumgarten, 2024). This configuration facilitates simultaneous temperature, aerosol, and wind soundings within the middle atmosphere, showcasing the system's advanced capability for comprehensive atmospheric analysis.
For wind measurements, the 532 nm wavelength and the Doppler Rayleigh Iodine Spectrometer (DORIS) technique are utilized (Baumgarten, 2010). DORIS determines the Doppler-shift of backscattered light using a single molecular absorption line of iodine, stabilizing the lasers at the edge of this absorption line, as shown in Figure 3.2. In the detection setup, the backscattered light is split, with a portion passing through a second

iodine cell. The Doppler-shift alters the amount of light absorbed by the iodine cell, allowing the Doppler-shift to be reconstructed from the ratio of the count rate before and after the iodine cell using a calibration function, which also takes the atmospheric temperature into account. This stabilization method on the iodine line negates the need for vertical pointing to establish the system's zero wind position.
The system is able to utilize double FPI as daylight filters and is thus the only Doppler-wind lidar capable of daylight measurements in the middle atmosphere (Baumgarten et al., 2015). ALOMAR is also the only middle atmospheric lidar that was validated using colocated rocket-borne wind measurements for altitudes between 30 and 60 km (Lübken et al., 2016).

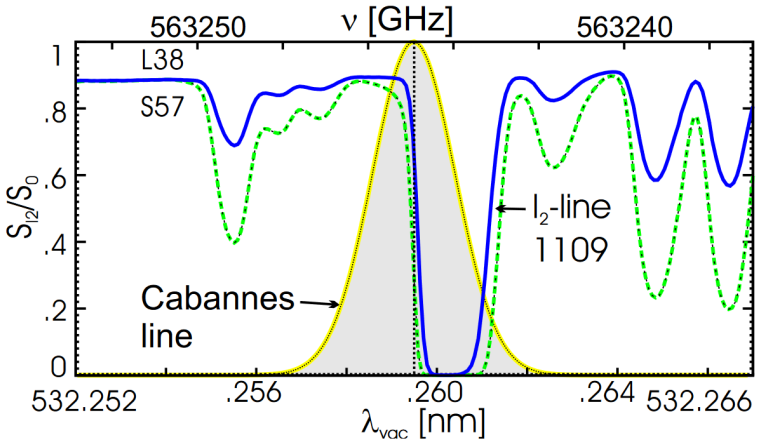

Figure 3.2. Transmission spectra of two different iodine cell setups (L38: 15 cm & 38°C, S57: 10 cm & 57°C). For reference the Doppler-broadened Rayleigh scattering (Cabannes line) for 230 K is shown. The dotted vertical line indicates the seed laser stabilisation wavelength of the ALOMAR-RMR lidar (Baumgarten, 2010).

Observatoire de Physique de l'Atmosphere de la Reunion (OPAR)

The LiWind lidar, situated at OPAR on La Réunion island in the Indian Ocean east of Madagascar, was established in 2012, adopting the same wind measurement technique as the OHP wind lidar. A notable design adaptation is its single, rotating 60 cm telescope, employed for both the expansion of the beam and the collection of backscattered signals. This lidar system boasts the capability to measure winds up to an altitude of 50 km. Similar to its OHP counterpart, it lacks daylight suppression features (Ratynski et al., 2023).

Chinese wind lidars

Two operational Chinese Doppler wind lidars are currently in use. The first system utilises a mobile setup housed in two large truck containers, each functioning as an independent lidar system. This configuration marks it as the only operational, mobile Rayleigh Doppler-wind lidar for the middle atmosphere. To measure the horizontal wind field, these systems are positioned orthogonally, utilizing 1 m telescopes angled 30° off zenith. The detection

of Doppler shifts employs a method inspired by the DORIS technique but features a simplified receiver with just 4 detectors (Xia et al., 2012; Yan et al., 2017).
The second system is mounted on a 6 m turntable and uses a single, tiltable telescope with an aperture of 80 cm, which allows for variable beam pointings. This system uses a similar technique to the OHP wind lidar, based on a double edge FPI. The system is capable of measuring winds during the night up to 47 km altitude, with a maximal random wind error of ∼6 ms^{-1} above 30 km and ∼3 ms^{-1} below (Chen et al., 2023).

Middle atmospheric lidar facility at the Leibniz Institute of Atmospheric Physics in Kühlungsborn (RMR3)

In 2021 a wind lidar at the IAP in Kühlungsborn became operational, called simply the third Rayleigh-Mie-Raman lidar (RMR3). The system uses the DORIS technique, similar to Alomar, but is reduced in complexity, with only a single laser distributed the east and north field of view and 5 receiver channels (1 Raman, 4 Doppler-Rayleigh). As telescopes two 70 cm mirror telescopes are used. With a 2 h integration time, the system can measure zonal and meridional wind at night simultaneously between 30 and 90 km (Gerding et al., 2023).

3.3 Aeolus - A Doppler Wind Lidar in Space

Space-based Doppler wind lidars provide the ability to obtain global wind profiles. The first satellite carrying such an instrument is the Atmospheric Dynamics Mission-Aeolus (Aeolus), which embarked on its mission in August 2018 and continued its measurements until May 2023. Aeolus orbits the Earth in a Sun-synchronous, dusk/dawn orbit (inclination of 97°) at a height of 320 km (ESA, 2020). Winds are measured orthogonal to the flight direction at an angle of 35 degrees off-nadir on the night side of the Earth. Along this field of view, the mission aimed to provide line of sight (LOS) winds from the ground up to the lower stratosphere (up to 30 km) with an altitude resolution of 250 m to 2 km and an altitude-dependent precision of 1 m s^{-1} to 3 m s^{-1} (Drinkwater et al., 2016). The actual error estimates during the operation were proved to be in the range of 4.1 m s^{-1} to 4.4 m s^{-1} (Rayleigh) and 1.9 m s^{-1} to 3.0 m s^{-1} (Mie) by Martin et al. (2021). Later validation campaigns showed even higher random errors due to the decreasing signal levels throughout the mission. Witschas et al. (2022) report a random error for Rayleigh clear winds of 5.5 m s^{-1} to 7.1 m s^{-1} in the altitude range from 0.5-10.5 km and Ratynski et al. (2023) report an error between 5.37 m s^{-1} and 6.49 m s^{-1} in the altitude range up to 27 km. The Atmospheric Laser Doppler Instrument (ALADIN) onboard Aeolus used a frequency tripled Nd:YAG laser operating at 355 nm and two receiver channels. The first channel utilises coupled Fabry-Pérot interferometers to capture the Rayleigh scattering signal, while the second channel incorporates a Fizeau interferometer to detect the narrowband Mie scattering (Paffrath et al., 2009; Reitebuch et al., 2009). While the FPI-method for Rayleigh scattering is very similar to the OHP method, albeit with a more refined and complex optical setup, the Fizeau interferometer generates a fringe image on the 16x16 pixel accumulation charge coupled device (ACCD) detector. This gives Aeolus the capability to resolve the spectrum of the backscattered light on 16 frequency channels, as

shown in Figure 3.3. The frequency resolution spacing of the individual channels is here given by the pixel size of the ACCD detector. This results in a spectral width on the order of 250 MHz FWHM for observed Mie scattering.

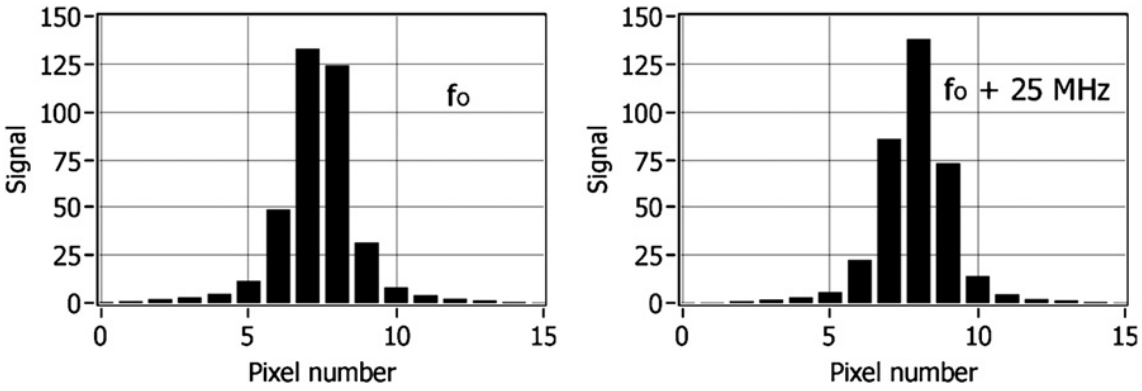

Figure 3.3. Spectrum of the internal laser reference as measured with the Fizeau interferometer of the ALADIN airborne demonstrator (A2D), which uses the same detection setup as the Aeolus satellite. Signal in 10^4 analog-digital converter counts vs pixel number. **left:** Laser at the fundamental frequency f_0. **right:** Laser frequency shifted by 25 MHz. The frequency spacing between the individual channels is 100 MHz, given by the size of the ACCD pixels (Reitebuch et al., 2009).

Since the wind measurements presented in this work relies solely on Mie scattering to cover the altitude range between 3 and 25 km a closer look on its use by the Aeolus satellite is valuable. Within the height range covered by Aeolus, the Rayleigh and Mie scattering techniques serve complementary purposes. In scenarios where the atmosphere is contaminated with significant aerosol loads, such as clouds or smoke plumes, the quality of the Rayleigh winds may be compromised. However, the Mie winds derived under these conditions exhibit an improved quality, with error estimates approximately half of that associated with clean Rayleigh winds (Rennie et al., 2021; Rani et al., 2022).

This reduction in measurement error can be attributed to the narrowband nature of Mie scattering, which allows for a more accurate estimation of the Doppler shift. Due to the substantial mass of the aerosol scattering particles, temperature-induced broadening of the Mie backscattered signal can be neglected. As a result, the spectral width of the Mie scatter is about two orders of magnitude smaller than that of the Rayleigh scatter for Aeolus. While these advantageous spectral properties of Mie scattering enable more precise wind measurements, it is important to note that the ALADIN instrument requires complementary Rayleigh-winds, since the use of the Mie channel necessitates sufficient aerosol loading to derive Mie winds. Consequently, it cannot solely rely on background aerosols present in the atmosphere for wind measurements (Drinkwater et al., 2016; Reitebuch et al., 2009).

3.4 Measurement Principle of the VAHCOLI Instruments

The VAHCOLI instrument employed in this study uses a measurement technique notably different from the Doppler-wind lidars previously described. Unlike traditional ground-based instruments that rely on comparing two channels with distinct spectral filters, VAHCOLI instruments adopt a spectroscopic method, which was derived from the method used by IAPs potassium Doppler-resonance lidar (von Zahn and Höffner, 1996). Adapted for Doppler-Mie, Doppler-Rayleigh and Doppler-resonance measurements, this approach was initially introduced by Lübken and Höffner (2021) and further elaborated by Froh (2021). In general, the instruments measure spectra of the backscattered light by scanning an alexandrite ring laser quickly and precisely over fixed narrowband filters. A sketch of this concept is shown in Figure 3.4 for a single arbitrary filter and 10 laser pulses. As discussed later in section 3.4.2, the VAHCOLI instruments utilise this method on two different filters to separate the different scattering processes, with typically 400 frequency channels. The LOS wind can then be extracted from the Doppler-shift of the measured spectrum, as discussed in detail in chapter 5.

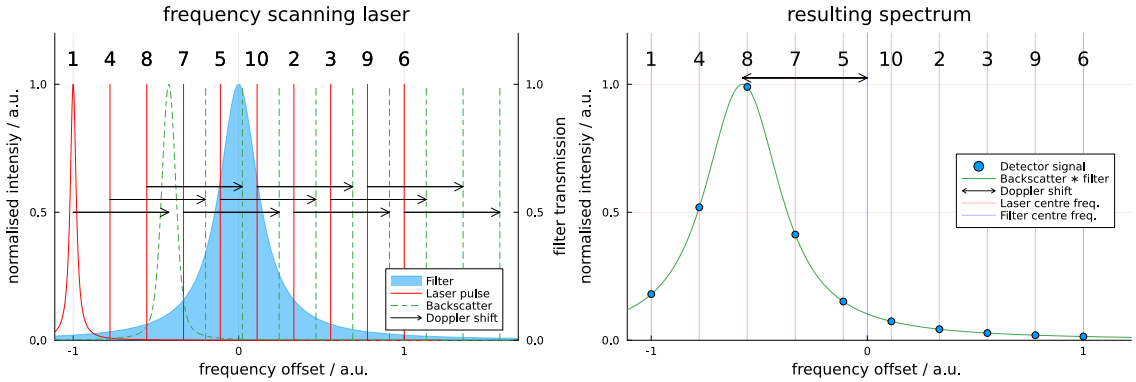

Figure 3.4. Simplified sketch of the general spectroscopic method utilised in the VAHCOLI instruments for an arbitrary filter, laser and scattering process. Note that instead of 10 frequencies, VAHCOLI typically uses 400. **left:** The pulsed power laser (red) is scanned in frequency in the pattern indicated by the numbers from 1 to 10. The backscattered light (green dashed) received from the atmosphere, which is Doppler shifted (black arrows) and broadened in the scattering process, is analysed using a fixed filter (blue). **right:** Resulting spectrum measured by a detector behind the spectral filter on the ten frequencies (blue), together with the theoretical spectrum, which results from the convolution of the spectrum of the backscattered light and the filter spectrum.

In order to realise this measurement concept technically, a narrowband, rapidly tunable seeder laser is employed for the purposes of spectral characterisation and stabilisation of the filters. To achieve Doppler-resonance measurements this seeder laser is additionally stabilized using Doppler-free polarization spectroscopy on potassium as an absolute wavelength reference, and nonlinearities in its frequency scanning are corrected based on the spectral periodicity of a fibre optic resonator. The seeder laser also controls the frequency for the alexandrite power laser, which is used for atmospheric probing. A novel technique called advanced Ramp&Fire stabilizes the pulsed laser in frequency and also allows for

the compensation of a possible frequency offset to the seeder laser. A small part of each pulse of the power laser is diverted into the detection bench as a reference and characterized using the spectral filters. The majority of the laser pulse is directed via a two-axis galvanometer scanner into the five telescopes of the upgraded lidar. The development of the multi field of view upgrade, which added this scanner and four additional telescopes, is described in more detail in the next chapter. The telescopes are not only used for the reception of the backscattered photons but also for the widening of the laser beam. In the detection bench, the backscattered photons are spectrally analysed using the combination of a planar and a confocal etalon.
Wind measurements utilizing Mie and Rayleigh scattering benefit significantly from this spectral method. The incorporation of narrowband filters mitigates daylight background interference, thereby enabling measurements during daylight hours. Importantly, atmospheric temperature variations do not impact the wind measurements, as these variations do not affect the peak position of the measured spectra. The presence of aerosols plays a dual role: it is exploited for wind measurement in the context of Mie scattering (as elaborated in Chapter 5), whereas it does not influence the measurements derived from Rayleigh scattering. A notable advantage of this method is the use of a single detector, with one optical element serving as the frequency discriminator, for the measurement of a spectrum. This setup eliminates errors associated with signal comparison across different optical paths, detectors, or electronic systems, thereby significantly simplifying the wind calibration process. The sole calibration required for wind measurement is the accurate determination of the frequency scan of the power laser relative to the employed filters. This is measured using an internal reference simultaneously with the atmospheric measurement. The calibration facilitates the direct calculation of the Doppler shift, which can then be converted into a line-of-sight wind velocity using Equation 3.1. Additionally, the high spectral resolution of typically 400 frequencies per spectrum (adjustable in the control software), makes the method robust against disturbances and allows for a control of the measured spectra against the scattering theory in order to quickly detect faults in the measurement system.
Figure 3.5 illustrates the optical configuration of the instruments, categorizing them into three main components: **(1)** the Laser subsystem, **(2)** the telescope and beam stabilization subsystem, and **(3)** the detection bench. The alexandrite laser and the spectral analysis capabilities of the detection bench are further elaborated in subsequent subsections. For discussions on the multi-field of view upgrade, it is important to note that the optical axes of the alexandrite ring laser and the detection bench are coupled via a polarizing beam splitter (coupling PBS), allowing beam stabilization to be managed by a single piezo mirror situated before the coupling PBS.

3.4.1 Alexandrite Ring Laser

The alexandrite ring laser used for the measurements presented in this work, is a power scaled version of the alexandrite ring laser, which was developed in cooperation with the Fraunhofer Institute for Laser Technology (ILT) in Aachen over the course of the last decade (Strotkamp et al., 2013; Munk et al., 2016, 2018, 2021). The new power scaled versions of the laser called prototype 3 and prototype 4 (PT3 & PT4) are described in de-

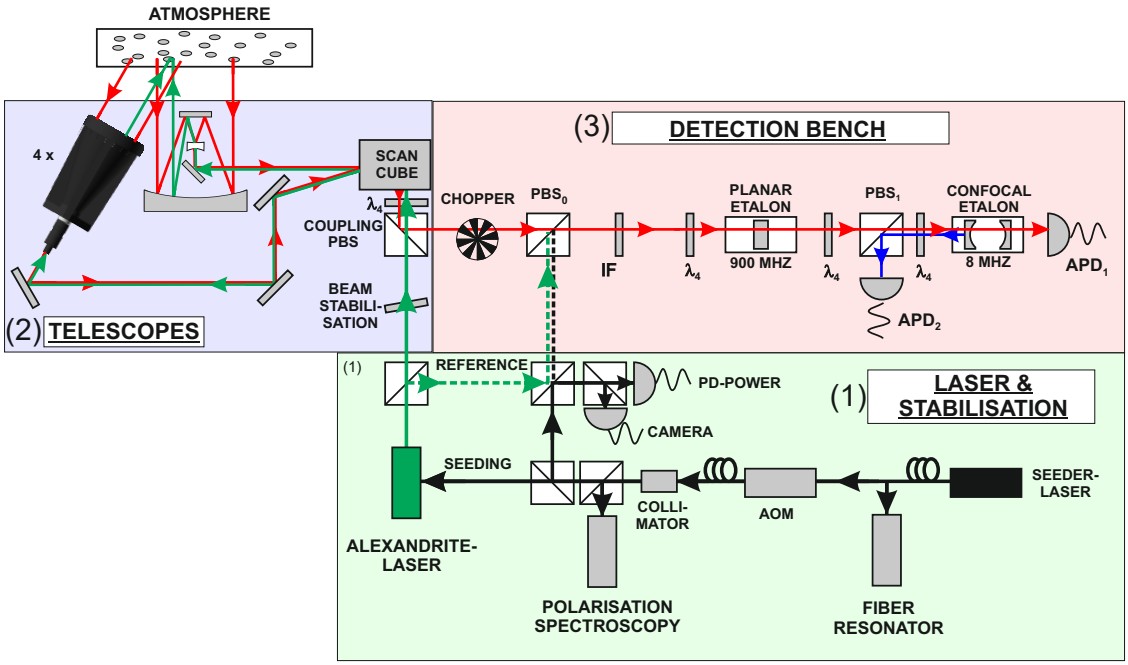

Figure 3.5. Schematic representation of the VAHCOLI instruments optical setup divided into three groups: **(1)** Laser system comprising the Seeder (black) and alexandrite (green) laser, **(2)** Telescopes and beam switching, and **(3)** Detection bench with separate inputs for atmospheric (red) and reference signals (dashed lines). For frequency stabilization, polarization spectroscopy on potassium serves as an absolute wavelength reference, and a fiber optic resonator is used to linearise the frequency axis during scanning. The detection bench includes a filter combination with interference filters, a planar, and a confocal etalon. The transmitted and reflected (blocked) signals of the etalon filters are captured on two detectors (APDs), separating the reflected signal from the input signal by exploiting polarization. A chopper blocks the atmospheric signal during reference measurements. Adapted from Froh (2021).

tail in Munk et al. (2023). They feature a higher pulse energy of 3.0 mJ (PT3) and 3.2 mJ (PT4) at a repitition rate of 500 Hz (PT3) and 750 Hz (PT4), which equates to a power of 1.5 W (PT3) and 2.4 W (PT4). The repetition rate of the laser, together with the number of frequencies in a spectrum determines the speed with which a full spectrum can be measured. The typical 400 frequencies of a spectrum can be scanned with the PT4 laser within 533 milliseconds, whereas a complete scan with the PT3 laser requires 800 milliseconds. Although the general power output of the alexandrite ring laser appears to be small when compared to traditional Nd:YAG lasers (e.g. Quanta-Ray Pro290, 800 mJ, 24 W), it has clear advantages when it comes to the spectral properties of the laser. Alexandrite lasers equipped with the advanced Ramp&Fire technology can be quickly and precisely tuned in frequency over a wide frequency range. Additionally, the laser is operated in long pulse mode, giving it a spectral bandwidth of less than 3 MHz at a pulse length of $\sim$1 μs (e.g. Quanta-Ray Pro290, $\sim$90 MHz).

This combination of frequency control and small spectral bandwidth is necessary for the spectral measurement method. Frequency control is critical as it enables the scanning of

the power laser across two highly stabilized interferometric filters. Concurrently, maintaining a small spectral bandwidth is essential for the efficient separation of Mie and Rayleigh backscattered signals through optical splitting.

3.4.2 Optical Splitting of Mie and Rayleigh Backscatter

The spectral method employed in the VAHCOLI instruments leverages optical splitting among various scattering processes based on their Doppler widths. Figure 3.6 presents a simplified schematic of this methodology for the case of perfectly rectangular filters.

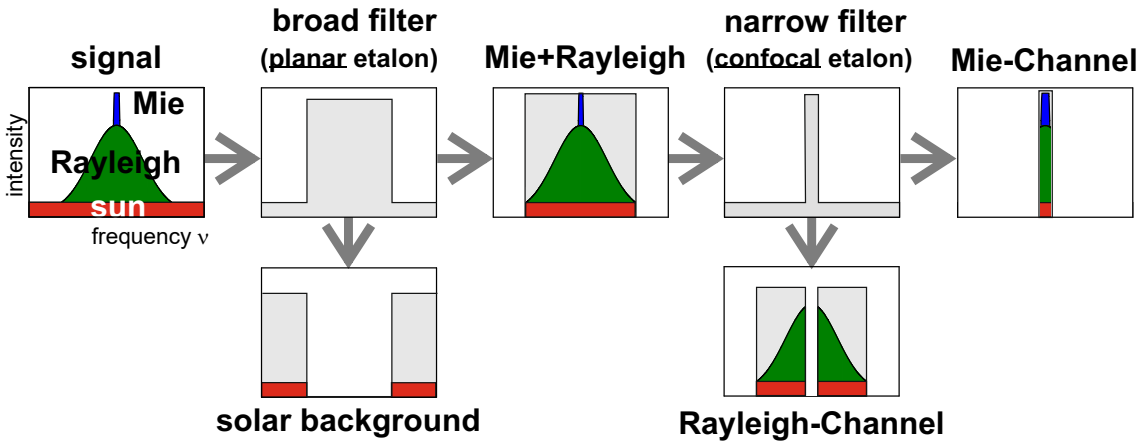

Figure 3.6. Simplified schematic representation of the optical splitting of different scattering processes based on the Doppler width using the example of Mie (blue) and Rayleigh (green) scattering with solar background (red) and rectangular filter. The central wavelengths of the filters and of the Mie and Rayleigh signals are identical, as it is the case for zero wind. Adapted from Froh (2021).

The lidar captures light through the telescopes, that contains a mix of daylight background, Rayleigh backscatter, and Mie backscatter, directing it into a detection bench. This light first passes through a broad filter, which effectively rejects the bulk of the daylight background. The signal transmitted through this filter consists of the backscattered Mie and Rayleigh signals, along with a minor fraction of the solar background. This background is frequency independent and given by the illumination of the sky. Subsequently, this mixture is subjected to a second, narrower filter. This filter sorts the light into two parts: one containing the spectrally narrow Mie scattering and a small portion of the Rayleigh scattering, which is transmitted, and another containing the majority of the Rayleigh backscatter, which is reflected. Each portion is detected by an avalanche photodiode (APD), resulting in the Mie-channel (APD_1) and the Rayleigh-channel (APD_2). This configuration significantly diminishes the fraction of solar background in the Mie-channel to a nearly undetectable level, and substantially reduces it in the Rayleigh-channel (Froh, 2021). Compared to Aeolus, which uses a similar approach, a much higher finesse of the filters combined with the sequential stacking results in virtually solar blind measurements of the Mie spectrum for the VAHCOLI instruments.

In practice, the filters incorporated into the system are not ideal rectangular filters but consist of two interferometric filters: a broader planar etalon with a spectral width of 900 MHz, a free spectral range (FSR) of 90 GHz, and a finesse (F) of 100, alongside a narrowband confocal etalon with a spectral width of 7.5 MHz, an FSR of 1 GHz, and a finesse of 130. The spectral characteristics of these filters, depicted in the left panel of Figure 3.7 alongside the scattering phenomena and the laser line, are governed by the Airy function, which can be approximated with a Lorenz function near its peak. As previously mentioned, the filters are stabilized to a high degree, with a root-mean-square (RMS) deviation on the order of 100 kHz (Lübken and Höffner, 2021). Frequency scanning of the power laser yields spectra on both channels, the spectral contours of which are represented as the convolution of the filters' spectral profiles, the scattering processes, and the laser's spectral shape. An illustrative spectrum obtained from the Mie-channel of the VAHCOLI 1 instrument is displayed in the right panel of Figure 3.7. The Rayleigh scattering appears as an almost linear background due to the narrow frequency scanning range. Superimposed on the Rayleigh scattering, the Mie peak is distinctly discernible.

The Doppler shift observed in the spectra is used for the wind speed determination, as discussed in more detail in Chapter 5. It is notable that the Mie-peak is particularly beneficial when used for wind measurements, due to its narrow spectral shape. Despite broadening from convolution with the filter and laser spectral shapes, the spectral width of the Mie-peak is only by a factor of 4-5 larger than the Doppler shift induced by a wind of 1 ms^{-1}. This is in stark contrast to the factor of 692 observed for the Rayleigh peak.

For the VAHCOLI instruments, the width of the frequency scan can be altered easily

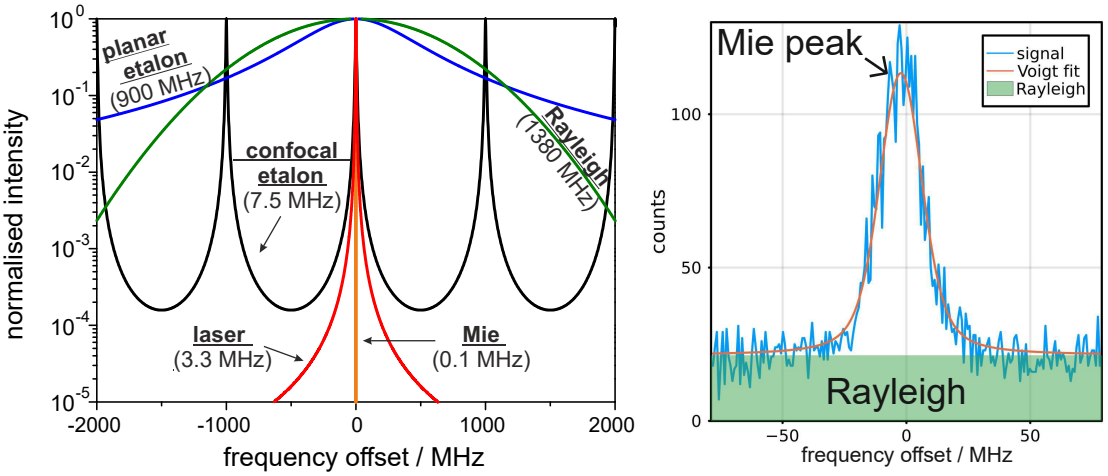

Figure 3.7. **left:** Spectral shape of a filter combination with two etalon filters, similar to the real system. Represented are the Rayleigh scattering (green, $\Delta\nu$ = 1380 MHz, T = 200 K), Mie scattering (orange, $\Delta\nu < 0.1$ MHz), laser (red, Lorentzian shape, $\Delta\nu = 3.3$ MHz), planar etalon (blue, FSR = 75 GHz; $\Delta\nu$ = 900 MHz; F = 83), and confocal etalon (black, FSR = 1 GHz; $\Delta\nu$ = 7.5 MHz; F = 130) (Froh et al., 2022). **right:** Spectrum measured with Mie-channel of the VAHCOLI 1 instrument in an altitude between 19.8 and 20.8 km on the 16th of December 2022, with an integration time of 2h along the vertical field of view. The contribution of the Rayleigh-scattering to the signal is marked green and the Mie-peak is clearly visible on top.

within the control software depending on the scientific goals. This measurement technique allows for the construction of a compact, universal Doppler-lidar which can measure the spectra of Mie scattering, Rayleigh-scattering and resonance scattering, covering a large altitude range with just two detectors. Based on the Mie-channel, measurements of wind and aerosol properties are realised, as discussed in more detail in Chapters 5 and 6. The Rayleigh-Channel can be used for temperature measurements, as shown in Chapter 7, and wind measurements, based on the measured spectra of Rayleigh and resonance scattering.

3.5 Comparison of the Different Doppler-Wind Techniques

The instruments discussed in this chapter utilize various different measurement techniques for Doppler wind detection, broadly classified into three categories. The first category encompasses techniques based on the double-edge Fabry–Pérot interferometer, exemplified by the OHP and OPAR wind lidars, the Chinese turntable-mounted wind lidar, and the Rayleigh component of the Aeolus satellite. The principal advantages of this approach include its simplicity, with just one pressure regulated etalon, its well-established application in lidar technologies and its relative insensitivity to aerosol contamination, provided the frequency spacing of the two bandpasses is appropriately selected (Garnier and Chanin, 1992). However, a significant drawback of this method is its inefficiency, characterized by maximum blocking at the peak of the Rayleigh backscatter and highest transmission at the spectral wings of the scattering. The relatively large spectral spacing of the two bandpasses also prevent effective narrowband filtering to reduce the solar background. Instruments using this technique are typically also unable to do simultaneous measurements of wind and temperature, since the transmission through each bandpass is temperature dependent. This results in signals which are no longer proportional to the atmospheric density and thus cannot be used for temperature measurements (see Chapter 7).

The second category comprises techniques that utilize the absorption properties of an iodine gas cell, such as the DORIS techniques employed by ALOMAR, the Chinese mobile wind lidar, and the new IAP RMR3 system. Even though typically about one third of the Rayleigh signal is lost due to the absorption in the iodine cell, these methods harness significantly more of the Rayleigh peak than the double edge method, thereby offering enhanced photon efficiency. Conversely, this approach renders the instruments highly susceptible to aerosol contamination of the signal. As a result, additional corrective steps are necessary during data processing for altitudes below 30 km or within noctilucent clouds (Baumgarten, 2010). An advantage compared to the double-edge technique is that these instruments are able to measure winds and temperature simultaneously.

The third category encompasses spectral methods, as exemplified by the VAHCOLI instruments and the Mie-part of the Aeolus satellite. While both techniques involve capturing spectra of backscattered light, their methodologies diverge. Aeolus employs a fringe imaging technique with a Fizeau interferometer, enabling spectrum resolution without necessitating frequency scanning. Conversely, the VAHCOLI system achieves spectrum resolution through laser scanning. A significant advantage of spectral methods is their immunity to aerosol contributions. For Aeolus and VAHCOLI Mie-winds, the Mie scattering from aerosols is leveraged for wind measurement. In the case of VAHCOLI Rayleigh-winds,

aerosol contributions do not alter the peak's position, thereby not affecting wind measurements. However, a limitation of the methods for Mie-peak measurements is the frequent emission of the laser at frequencies substantially blocked by the confocal etalon or the Fizeau interferometer. For VAHCOLI this drawback is largely mitigated by the increased sensitivity to the position of the Mie-peak due to the narrow filter width ($\approx$ 1/20th of the Aeolus filter width). Furthermore, spectral scanning parameters can be readily adjusted within the control software to minimize this issue. This adjustment can even be done to use different scan windows for the measurement of horizontal and vertical winds, since vertical winds typically are much smaller and thus a smaller scan window can be used, increasing the efficiency of the method. Additionally, spectral methods allow for continuous monitoring of system performance, with deviations in the laser's spectral width immediately evident in the measured spectra. This spectral monitoring capability renders spectral methods likely less susceptible to instrumental effects, thus providing a more robust technique compared to the double-edge FPI and DORIS methods previously discussed. The VAHCOLI method can be seen as a significant advancement compared to the Aeolus method here, due to its much higher spectral resolution.

4 | Technical Development of the Multi FOV Upgrade

4.1 Rationale for the Multi FOV Upgrade

As highlighted in Section 2.1, atmospheric phenomena manifest across a diverse range of scales, from less than a meter to several hundred kilometers. Lidars, with their typically very narrow fields of view, necessitate the use of multiple fields of view (Multi FOV) approaches to effectively encompass these scales. A straightforward strategy involves arranging multiple instruments, each with a single field of view, in such a way that their spatial configuration spans the spectrum of these scales. The design of such a network can be customized to the study's emphasis, with micro to meso-scale phenomena requiring closely spaced instruments (a few kilometers apart). This arrangement may restrict coverage of larger scales if only a limited number of instruments are available. An alternative involves the use of single instruments equipped with multiple, tilted fields of view, as detailed in Lübken and Höffner (2021). This configuration allows a single instrument to monitor smaller scales through the horizontal separation of its fields of view, enabling a broader geographical distribution of instruments for extensive area coverage. A system equipped with five fields of view (1 vertical, 4 tilted) using five telescopes can span a variety of scales. Particularly small horizontal scales, significantly below 100 m, can be addressed by minimally adjusting the viewing angle through a single telescope. This facilitates the realization of multiple fields of view within one telescope, albeit with minimal separation. However, this approach is viable only for systems with very high time resolution to discern differences between these proximate fields of view and is, therefore, not further discussed in this thesis.

For the coverage of larger scales, the horizontal difference between the individual fields of view can be exploited. The specific horizontal scales that can be addressed depend on the off-zenith tilt of the individual fields of view. For instance, at 20 km altitude, two fields of view tilted 30 degrees off zenith in opposite directions (e.g., the north and the south FOV) have a horizontal separation of ≈23 km, the zenith-pointing FOV has a horizontal separation from the tilted FOVs of ≈11.5 km, and two perpendicularly tilted FOVs have a separation of ≈16 km. By correlating these fields of view, these three horizontal scales can be covered at 20 km altitude. For much larger scales, in the order of several hundred kilometers, a network of these instruments is necessary.

To ensure effective coverage of vertical scales, each instrument should be capable of observing from the troposphere to the thermosphere. This requires simultaneous Doppler

Rayleigh, Mie, and resonance measurements within a single system.

As previously mentioned, atmospheric properties can be measured with lidar only along the field of view. This aspect is especially critical for measuring horizontal winds. Along a field of view pointing directly up to the zenith, no horizontal wind component can be measured, necessitating the use of tilted fields of view. Therefore, multiple fields of view are essential not only for covering atmospheric scales but also for measuring all three wind components.

The technical development and implementation of an upgrade that transitions a single field of view instrument to a multi-field of view capability are discussed in this chapter.

4.2 Design Considerations

As the VAHCOLI instruments are designed for network usage, the MultiFOV upgrade prioritises minimal modifications to ensure ease of deployment across the system. This design philosophy aims to limit the increase in construction time, particularly since the network requires multiple units, thus avoiding extensive alterations to time-intensive components like the laser and detection bench. Cost-effectiveness is paramount, as the upgrade must significantly enhance lidar capabilities without proportionally increasing expenses, ensuring the network's expansion remains financially viable. Additionally, it's crucial that this upgrade does not compromise the VAHCOLI units' core functionalities while broadening their observational scope.

4.3 Telescope Design

The design of the MultiFOV upgrade for the VAHCOLI instruments incorporates four additional, tilted telescopes. These telescopes play dual essential roles: firstly, they expand the power laser beam to diminish its divergence in the atmosphere, and secondly, they are responsible for capturing backscattered photons. This dual functionality marks a departure from more conventional middle-atmosphere lidar systems, which typically employ two separate telescopes for emission and reception.

The integration of both tasks within a single telescope unit simplifies the VAHCOLI instruments by reducing system complexity, ensuring precise alignment between the emitter and receiver components, and facilitating rapid switching between different fields of view for both emission and reception. This consolidation offers significant advantages in terms of operational efficiency and system robustness.

However, this approach also imposes stringent requirements on the optical quality of the telescopes. The design of these telescopes becomes a critical factor in the overall performance of the lidar system. Achieving their dual roles effectively demands a high degree of precision and attention to optical design and thus, a reliable method to measure said optical quality of each constructed telescope in a quality control step is of high importance.

4.3.1 Relevant Optical Effects

For the design of a lidar telescope one has to consider different effects which are relevant to the telescopes' performance, apart from traditional measures of optical performance, like the point spread function of the telescope or its transmission.

Telescope field of view

A telescope designed for a lidar system capable of daytime operation typically features a very narrow field of view of few 10 μrad. This design choice is crucial for substantially reducing solar background interference, which increases with the square of the field of view. However, it's also important to ensure that the telescope's field of view is wide enough to capture the entirety of the scattered laser signal. The optimal field of view, which balances effective solar suppression and signal transmission, is determined based on the laser's divergence and the telescope's optical properties. Ideally, the telescope's field of view should be twice the laser divergence, limited by the laser's M^2 factor [1], measured at Full Width Half Maximum (FWHM), ensuring reception of 96% of scattered photons while minimising solar background. In practice, a wider field of view is often selected to account for realistic conditions such as atmospheric disturbances ('seeing') and optical aberrations ('defocus'), which can diminish the telescope's performance.

Seeing

Seeing is an effect often encountered in astronomical observations through telescopes, particularly at or near optical wavelengths. This effect introduces additional blurring to the observed images, primarily caused by light refraction in a turbulent atmosphere. As such, seeing is heavily dependent on atmospheric conditions. As noted in Anderson (1935), this effect is more pronounced in larger diameter telescopes. For instance, stars observed through a 4-inch telescope appear almost perfectly formed, whereas the same stars appear significantly blurred and irregular when observed through 60-inch or 100-inch telescopes. A common measurement for the strength of the seeing is the Fried-parameter r_0, which was derived by David L. Fried in the 1960s (Fried, 1966). This parameter, having the dimension of length, can be interpreted as the maximum diameter of a telescope that remains unaffected by seeing. It can be converted into the angular blurring θ of a point source with the wavelength λ as a result from the seeing conditions, as described by (Dierickx, 1992):

$$\theta \approx 0.025 \frac{\lambda}{r_0} \cdot \frac{\text{arcsec} \cdot \text{cm}}{\text{nm}} \tag{4.1}$$

At the IAP location, seeing conditions typically range between 2 and 4 arcseconds (10-20 μrad), corresponding to a Fried-parameter of approximately 6.88 to 3.44 cm (at 550 nm). Therefore, the impact of seeing on lidar measurements must be considered, when using any reasonably sized telescopes. The seeing conditions can also worsen drastically, depending on the measurement site (e.g. hot tarmac) and the weather conditions. This easily results

[1] The M^2 is a common measure to assess the beam quality of a laser. A diffraction-limited beam has a M^2 factor of 1, higher values lead to an increased laser divergence (Paschotta).

in seeing induced blurring in the order of 100 μrad and thus in significant signal loss for a lidar with a narrow field of view.
Both the Fried-parameter and the angular blurring θ are usually measured or predicted for a wavelength of 550 nm. The dependence of seeing on the wavelength is relatively mild, as indicated by

$$\theta \propto \lambda^{-\frac{1}{5}} \tag{4.2}$$

suggesting that seeing effects diminish at longer wavelengths. For example, moving from 550 to 10000 nm wavelength can improve angular resolution by a factor of 1.8 (Boyd, 1978). Due to the described telescope diameter dependence of the seeing there is a good argument in the astronomy for the use of smaller optics for certain applications (Ofek and Ben-Ami, 2020).

Beam widening factor and divergence

For the telescopes used for the VAHCOLI instrument, a general law of optics, the conservation of the telescopes' divergence and beam diameter product, applies.

$$\theta_{\mathrm{FOV}} \cdot D_{\mathrm{in}} = \theta_{\mathrm{out}} \cdot D_{\mathrm{out}} \tag{4.3}$$

For a telescope with an aperture of $D_{\mathrm{in}} = 500$ mm and a field of view of $\theta_{\mathrm{FOV}} = 30$ μrad, which reduces the beam diameter to $D_{\mathrm{out}} = 12.5$ mm by the magnification power $\mathrm{MP} = D_{\mathrm{in}}/D_{\mathrm{out}} = 40$, this results in a beam divergence on the receiver site of the instrument of $\theta_{\mathrm{out}} = 1200$ μrad, which equates to an increase of the beam diameter by roughly 1.2 mm for every meter travelled. This can cause problems in the design of the detection bench if the beam diameter becomes too large and causes vignetting in the detection bench, which can only be mitigated by building a compact receiver with minimal beam length. A high beam divergence can also cause problems with interferometric filters, increasing their spectral width and reducing their transmission. For larger diameter telescopes, this results in the need for larger diameter filters in order to increase the beam size through them and meet their divergence requirements (Folkard and Ward, 1986).

Defocus effects on overlap function

Telescopes have a focus point and thus, for a lidar which observes over a range of altitudes, only a singular altitude can be perfectly focused. This introduces an altitude (or range) dependent blurring, akin to the depth of field or bokeh effect in photography. A simplified model for the angular blurring of an idealized telescope can be derived from geometric optics as:

$$\theta_{\mathrm{DF}}(z) = \arctan\left(D \cdot \frac{z - z_{\mathrm{focused}}}{z \cdot z_{\mathrm{focused}}}\right), \tag{4.4}$$

where D represents the telescope diameter and z_{focused} the altitude in focus (Coddington, 1829; Anonymous, 1866). In lidar telescopes, typically characterized by small angles, the blurring is proportional to the telescope's diameter. This effect, if not properly accounted for when adjusting the instrument's field of view, can lead to signal loss and an altitude dependent sensitivity of the instrument.

The actual defocus function, however, is more complex, and its impact, for example on the altitude dependent transmission through a lidar instrument onto its detector, can only be accurately calculated numerically using tools like raytracing.
Figure 4.1 presents results from the simplified model of the blurring angle, alongside the more realistic outcomes from raytracing using the OSLO optical design suite for different telescope sizes. These simulations reveal that smaller telescopes exhibit significantly less altitude dependence in their signal strength due to telescope defocusing, compared to larger diameter telescopes.

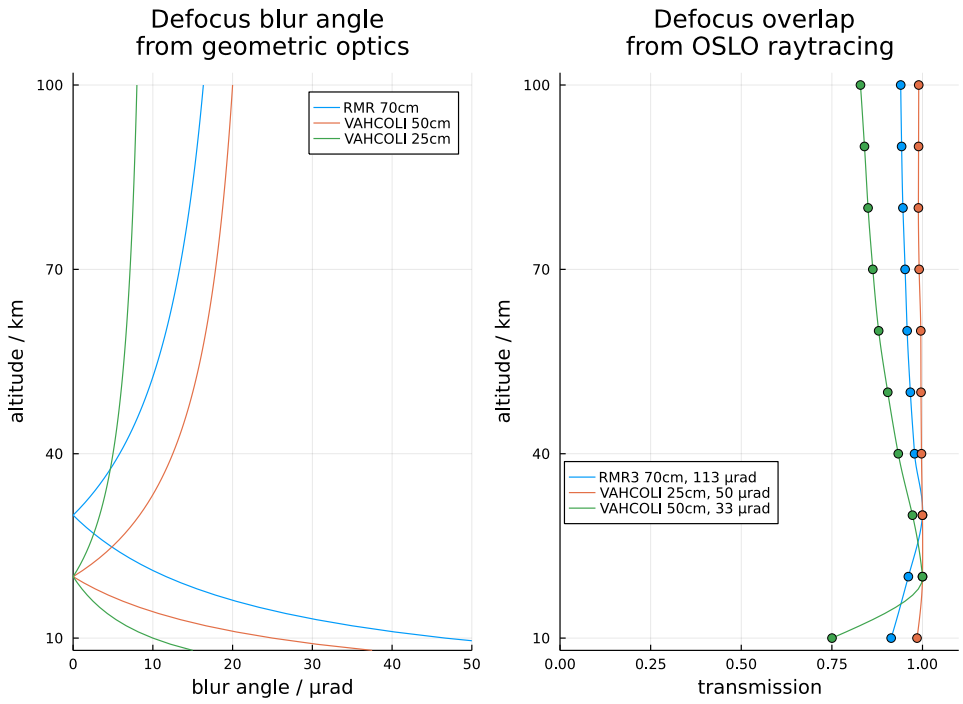

Figure 4.1. Defocus effects for 70 cm diameter telescope of the RMR3 wind lidar, the 50 cm vertical telescope and the 25 cm tilted telescopes of VAHCOLI. Reflecting their real world configuration the RMR telescope is focussed to 30 km, while the VAHCOLI telescopes are focussed to 20 km. **left:** Blur angle for the telescopes calculated using equation 4.4. **right:** The defocus contribution to the overlap function calculated using OSLO raytracing. For VAHCOLIs free beam optics, the complete optical path onto the detector was simulated, for the RMR system only the coupling into the 300 μm fibre optic cable was considered.

4.3.2 Optimal Telescope Size

In the selection of the optimal telescope size for a lidar system, operational parameters are paramount. For the VAHCOLI lidar instruments, the primary considerations include the system's extensive altitude coverage, ranging from 10 to 100 km, and its capability to operate in daylight conditions. Secondary, yet significant factors influencing the choice of telescope size are the overall system dimensions and the cost implications of the multi-field-of-view upgrade, inherent to VAHCOLI's network design.

Particularly crucial is the lidar's performance under daylight conditions. The solar background radiation intensity is directly proportional to both the telescope's field of view and its aperture area, which is related to the square of the aperture. The quantity of backscattered laser photons is also primarily a function of the telescope's aperture area. Hence, maintaining a constant field of view and disregarding influences such as telescope defocus and atmospheric seeing, the ratio of the received signal to solar background should remain stable across varying aperture sizes. This ratio is pivotal for lidar observations during daylight, and can be improved through spectral filtering. However, the enhancement potential is limited due to the spectral range of the backscattered signals and the consequent constraints on filter bandwidth.

Although the signal-to-solar background ratio is invariant to telescope size, the absolute photon count rate from solar background can quickly reach the upper limit of the lidar detectors' counting capacity. This phenomenon is exemplified in the IAP's mobile potassium lidar, which used an 80 cm mirror telescope with a 192 μrad field of view. Despite the use of twin Faraday anomalous dispersion optical filters (FADOF) for daylight suppression and the operation in a deep Fraunhofer line, the system encountered a solar background rate nearing 0.2 MHz (Fricke-Begemann et al., 2002). Considering that avalanche photodiodes (APD), as employed in both the potassium lidar and VAHCOLI, have a maximum count rate in the 1-10 MHz range, this results in a significantly constrained dynamic range for measurements of less than one or two orders of magnitude. For an instrument with a narrow altitude focus, such a range might be adequate. However, for systems like ALOMAR, which are designed to cover a broader altitude range, this necessitates multiple channels with varied attenuations to accommodate different altitudes, thereby complicating the receiver design (von Zahn et al., 2000). The compact nature of VAHCOLI's detection bench, which incorporates only two detectors for assorted scattering processes, demands that each detector has an extensive dynamic range to span the full measurement altitude range of 10-100 km. Consequently, the use of very large telescopes is unsuitable for VAHCOLI, given the significant solar background they entail.

These telescopes must ensure maximal transmission of the signal to the system's detectors across the entire measurement spectrum, while simultaneously enabling the utilization of small fields of view to effectively reject daylight interference. Figure 4.2 illustrates simulation results that estimate these parameters for telescopes of varying sizes. The simulations assess the impact of various optical phenomena on the ideal field of view.

In panels (a) and (b), the simulations demonstrate broadening effects on the field of view for telescopes with clear apertures of 200 mm and 500 mm, respectively. The factors incorporated in these simulations include a constant point spread function of 5 μrad, indicative of the optical quality of the telescope, the Airy diffraction disk related to the telescope diameter, laser divergence, atmospheric image size, and astronomical seeing conditions. For seeing conditions, a typical Kühlungsborn scenario with poor visibility of 4 arcseconds is assumed, resulting in an image blur of 13.7 μrad. From all blurring effects, the total blurring angle is calculated in the form of the FWHM of the convolution of the individual curves (dashed blue line). The simulations determine the optimal field of view for each telescope, defined as the field that encircles 95.6% (with minor deviations due to numerical methods) of the energy backscattered from an altitude of 10 km. For the 200 mm telescope, an optimal field of view of 64 μrad is calculated, while the larger 500 mm

telescope requires a broader field of view of 92 μrad to capture the same percentage of backscattered light.
Panel (c) of Figure 4.2 presents the altitude-dependent effects of telescope defocus and the combined impact of the geometrical size of the laser in the sky and laser divergence, resulting in angular blurring for the two telescopes, both focused at an altitude of 30 km. Although the 200 mm telescope exhibits less defocus blurring compared to the 500 mm telescope, it is more significantly impacted by the laser image in the sky due to higher laser divergence resulting from its smaller laser beam diameter. Panel (d) illustrates the overlap function for these two effects at a fixed field of view of 50 μrad for both the 200 mm and 500 mm telescopes, highlighting the larger variation in signal strength across the measurement altitude range in the larger telescope.
The total blurring angle and the calculated optimal field of view, considering the various optical effects, are displayed in Panel (e) for telescope sizes ranging from 50 to 800 mm. A distinct minimum in the optimal field of view is observed around the 200 mm telescope size. This translates to a peak in encircled energy at a fixed field of view size of 50 μrad for the 200 mm telescope, as shown in panel (f). Panels (g) and (h) also exhibit a similar maximum around the 200 mm size in terms of the optimal telescope field of view and the encircled energy within a 50 μrad field of view, under varying seeing conditions. Based on these analytical findings, it can be inferred that a telescope with a clear aperture of 200 mm is capable of operating with a small field of view, providing efficient daylight rejection, while also ensuring minimal signal strength variations across the altitude range. Therefore, under the specified conditions for the lidar instrument, a telescope size of approximately 200 mm is deemed optimal.
Notably, the optimal FOV and telescope size depends on the observed altitude range due to the defocusing effect. The image size is given by the M^2 factor of the laser and the beam diameter of the emitted laser. The smallest FOV is achieved if the laser divergence and diameter is adapted to the altitude range, which is not possible for the VAHCOLI instruments due to the secondary mirror obstruction of the 500 mm mirror telescope[2]. The 500 mm vertical telescope of the VAHCOLI units was integrated into the system in the original design, before the calculations presented in this chapter were done. Replacing the vertical telescope with a more optimal 200 mm lens telescope allows for the reduction in the FOV by optimizing the laser diameter for this altitude range; an approach which will be used in follow-up projects. The minimum laser divergence for a given diameter is also wavelength dependent, which is beneficial for lidars operating in the UV, since the image size can be reduced.
Additionally, the adoption of a smaller telescope size aligns well with the objectives of achieving compactness and cost-effectiveness, key aspects stemming from the network-centric approach embedded in the instrument's design.

4.3.3 Lens Telescope Design

In the development of the multi field of view upgrade for the VAHCOLI lidar system, a significant challenge encountered was the absence of commercially available lens tele-

[2]The secondary mirror of a mirror telescope prevents the emission of the laser on the optical axis of the telescope, since it would cause the power laser to be reflected back into the system.

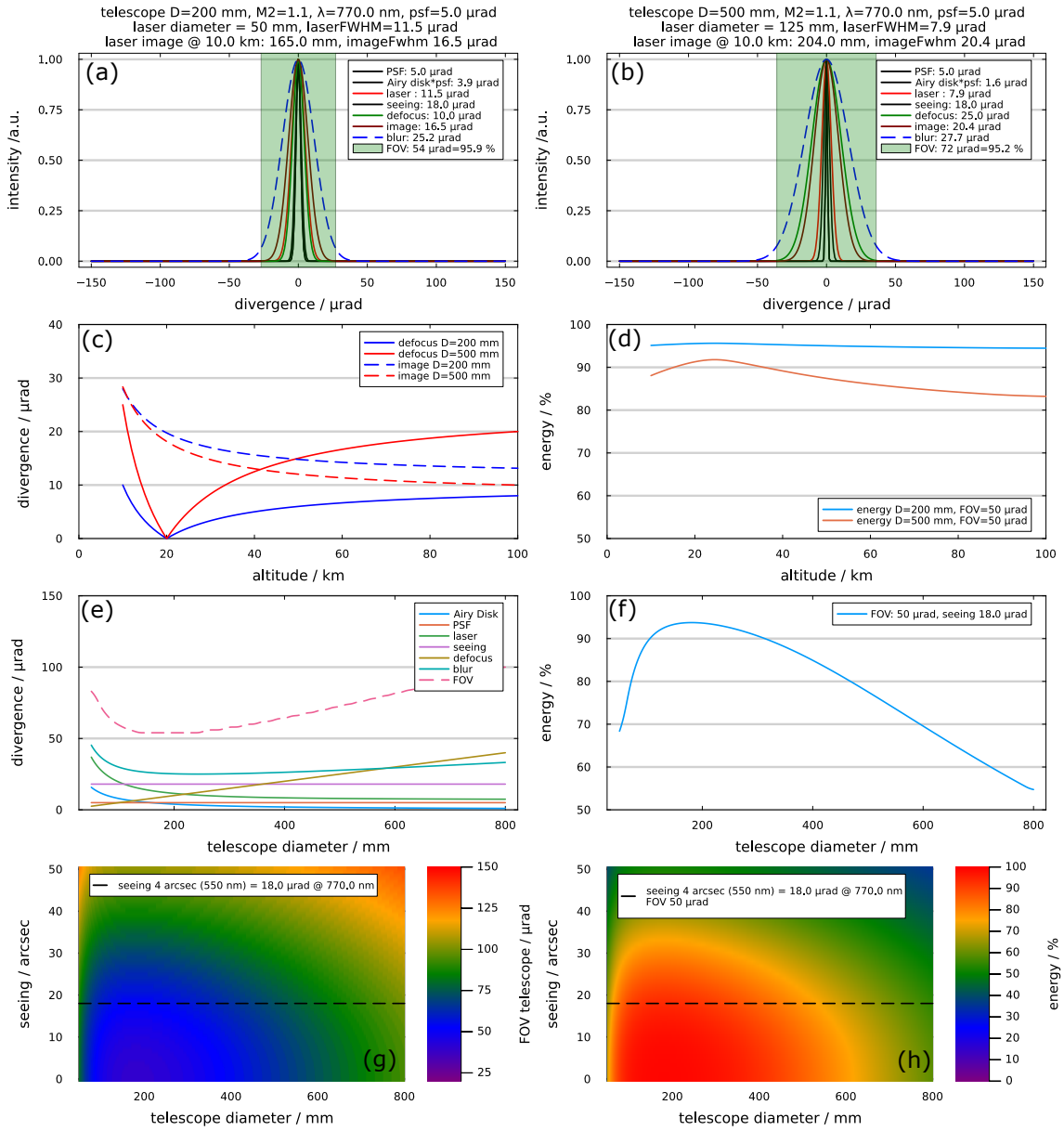

Figure 4.2. Results of a simplified simulation program to determine the optimal telescope diameter. **(a),(b)** Estimated FOV divergence due to diffraction, laser divergence and image, seeing and telescope defocus effect for two telescopes with 200 mm and 500 mm aperture. The optimal telescope field of view is highlighted by the green box. **(c)** Altitude dependence of the divergence component introduced by the defocussing and image of the laser beam in the sky for the 200 mm and 500 mm telescope. **(d)** Altitude dependence of the energy encircled in a 50 μrad field of view for the 200 mm and 500 mm telescope. **(e)** Telescope diameter dependence of different divergence components together with the resulting optimal field of view. **(f)** Telescope diameter dependence of the energy encircled in a field of view of 50 μrad under seeing conditions, typical for Kühlungsborn. **(g)** Ideal field of view in dependence of the telescope diameter and the seeing conditions. The black line marks seeing conditions, typical for Kühlungsborn. **(h)** Energy encircled in a 50 μrad field of view in dependence of the telescope diameter and the seeing conditions. The black line marks seeing conditions, typical for Kühlungsborn.

scopes that could meet the specific requirements outlined above. The available commercial lens telescopes with the necessary aperture typically feature front lenses with focal lengths significantly over 1000 mm, making them unsuitable for integration into our system. Although there are commercially available mirror telescopes with the required aperture size that are sufficiently compact, the obstruction by the secondary mirror significantly reduces signal strength and contrast. This issue is especially pronounced in smaller aperture mirror telescopes due to a higher relative obstruction compared to the free aperture, which is a major limitation of the 500 mm telescope within VAHCOLI for the vertical observations. This necessitated the custom design of a lens telescope tailored to our specific needs. Owing to the scarcity of commercially available lenses with a diameter of 200 mm or more, the front lens of the telescope was selected first. The choice fell on a polished condenser lens from Edmund Optics, with a diameter of 250 mm, a focal length of 500 mm, and made from N-BK7 substrate. The optical design and ray tracing software OSLO was then employed to simulate various configurations of commercially available optical elements with the objective of optimising the telescope's optical quality. The OSLO setup consisted of a homogeneously illuminated field of view of 33 μrad at infinity, with a wavelength of 770 nm, and a 200 mm entrance aperture. The simulations extended beyond the telescope, including the complete optical system from the front lens to the surface of APD1. The primary objective was to minimize the geometrical rms size of the image on the APD, while avoiding vignetting in both the telescope and the detection bench. As a secondary measure of optical quality, the configurations were evaluated based on the calculated point spread function of the telescope and the resulting encircled fractional energy.

Several combinations of commercially available lenses were tested using the software, with the most significant challenge being the strong spherical aberrations introduced by the large, strongly curved spherical front lens.

The final configuration, based on the simulations, comprised five commercially available lenses that produced the required optical quality, with a geometrical rms spot size close to the diffraction limit, as shown in Figure 4.3. The lenses were arranged into three groups: The first group contained only the front lens. The second group included two field lenses, a plano-concave lens with a 2-inch diameter and a focal length of -75 mm made from N-BK7 (Thorlabs LC1315-B), and a plano-concave lens with a 2-inch diameter and a focal length of 100 mm made from fused silica (Thorlabs LA4545). The third group contained two optical elements, a one-inch achromatic doublet with a focal length of -50 mm (Thorlabs ACN254-050-B) and a negative meniscus lens to adjust the exit beam diameter with a focal length of -300 mm (Thorlabs LF1015-B). The final layout of the optical components is visible in the bottom left panel of Figure 4.3.

The finalization of the telescope design was accomplished using the 3D modelling software OpenSCAD. A cross-sectional view of the 3D rendering of this finalized design is displayed in the right panel of Figure 4.3. During the design phase, particular emphasis was placed on mitigating turbulence between the front lens and the field lenses. This was achieved by implementing the cooling solution described in Section 4.6.1. The telescope housing was also specially contoured to facilitate easy insertion into the telescope holders, ensuring self-alignment within these holders to maintain the correct measurement geometry.

The construction of the telescope body involved a combination of additive manufacturing

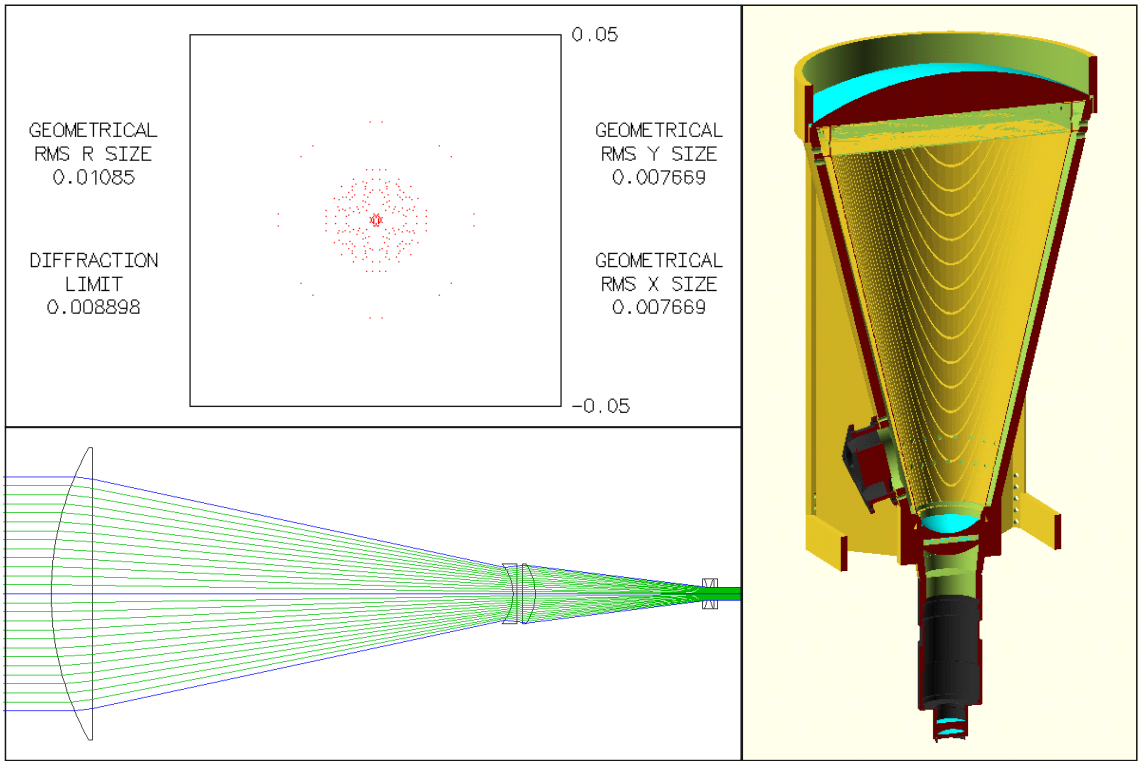

Figure 4.3. Images highlighting the design process of the lens telescopes. **top left:** Spot size diagram, as calculated using the OSLO raytracing software. The geometrical RMS R size is an essential parameter for the optimisation of the design. **bottom left:** The two dimensional lens layout from the OSLO software. The lens surfaces are shown in black, rays simulated by OSLO are shown in blue and green. **right:** Cut through the final CAD model of the telescope including the telescope body, with measures for turbulence reduction and ventilation.

techniques and aluminium optical system components, sourced from Thorlabs. The front lens is securely fastened to the main body of the telescope using a 3D-printed screw ring. This main body serves as the connecting piece between the front lens and the field lenses. The assembly housing the field lenses is contained within a separate 3D-printed holder, which can be conveniently attached to the main telescope body via 3D-printed threads. A two-inch Thorlabs tube is then affixed to this field lens group holder. The focusing mechanism of the telescope is implemented using a two-inch fine-thread tube. Lastly, the third optical group is entirely supported within a one-inch Thorlabs tube.

In order to assess the optical quality of the constructed telescopes, an autocollimation setup was implemented on an optical table. This setup, detailed in Appendix A, employs a collimated laser beam that passes through the telescope, reflects off a large planar mirror, and then travels back through the telescope to a camera. This double pass through the telescope magnifies the impact of any optical aberrations. The optical quality is assessed by comparing camera images of the laser beam with and without the telescope in its path, as shown in Figure 4.4. Analysis of these images involves fitting a Gaussian function to the intensity profiles captured by the camera to determine the Full Width at Half Maximum (FWHM) size of the beam. The beam's spot size without the telescope's influence is

approximately 18 μm, while with the telescope, it increases to about 21 μm.
Using the convolution rule for two Gaussian functions, the FWHM of the telescope's point spread function (PSF) can be estimated as follows:

$$FWHM_{PSF} = \sqrt{20.76^2 - 17.94^2}\mu\text{m} \approx 10.5\mu\text{m}. \tag{4.5}$$

This value closely aligns with the geometrical RMS radius of the spot, which is 10.85 μm as per the OSLO raytracing results. While the comparison is not exact, due to the double transmission through the telescope in the autocollimation setup and the general limitations of the setup introduced by the pixel size of the camera (5.2 μm) and possible nonlinearities in the intensity measurement, the similarity of the results indicates that the constructed telescopes are in good agreement with our theoretical calculations. For comparison: The aperture in the detection bench has a size of 100 μm, only approximately nine times the theoretical RMS radius of the spot. This is why this measure is of such importance.
Apart from the verification of the OSLO calculations, the autocollimation setup is used for the quality control of the individual telescopes and to set the focus points of the telescopes to infinity. For the final MultiFOV upgrade 6 lens telescopes (4 final, two spares) were build and tested, with all of them showing similar quality.

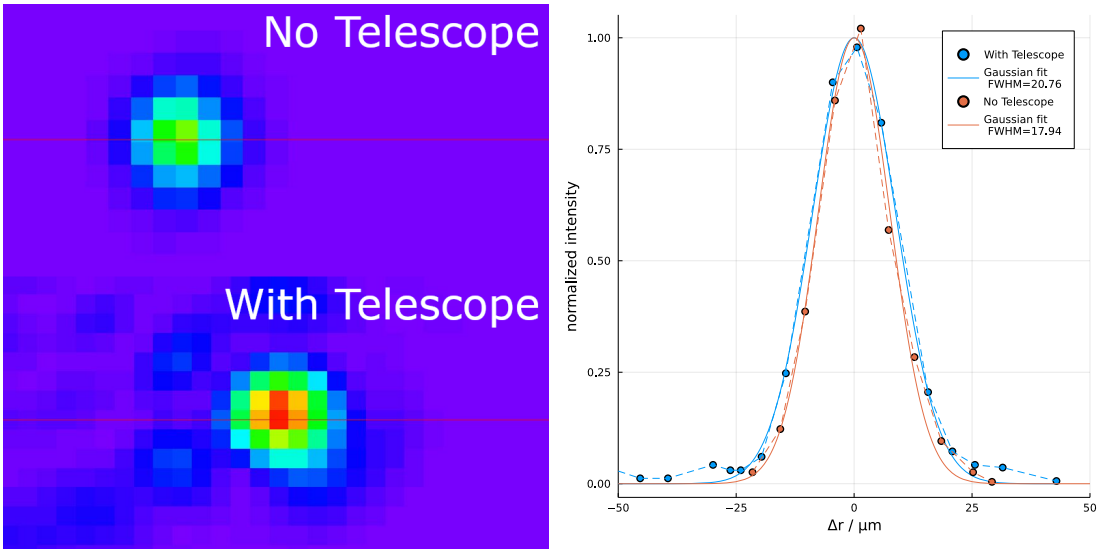

Figure 4.4. Results of the autocollimation measurement for the telescope with serial number SN1. **left:** Images of the beam, when focussed onto the camera. On the top is the image as produced by only the laser beam, on the bottom the image produced by the laser beam after being transmitted twice through the telescope. **right:** Gaussian fits through the normalised intensity profiles of the spots, together with the calculated FWHM size of the spot. The cut through the spot which is used for the intensity profile is indicated by the red lines in the left panel.

4.4 Beam Switching

For the multi field of view upgrade of the VAHCOLI instrument, a rapid and efficient method for transitioning between different fields of view is crucial. Given the alexandrite

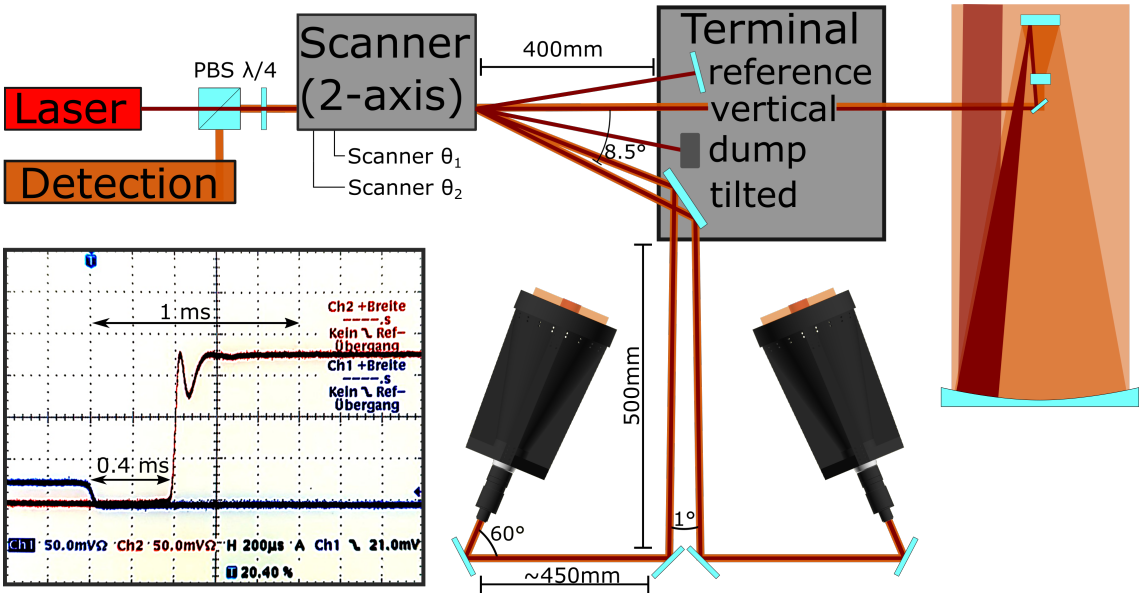

Figure 4.5. Schematic drawing of the beam switching as done by the laser. For readability only two of the four tilted telescopes are shown. The beam switching of both the detection bench and the laser beam is done via the combination of a 2-axis galvanometer scanner and the distribution terminal (grey). In the bottom left panel the switching between two fields of view is shown, as measured with two photodiodes and an oszilloscope.

ring laser's repetition rate of 500 Hz and atmospheric measurements extending up to 150 km (corresponding to approximately 1 ms of travel time for light), there is only a 1 ms window available for beam switching. Any delay beyond this window could result in lost pulses, potentially distorting the measurement data and risking damage to parts of the system not designed to withstand laser impact. To address this, a two-axis galvanometer scanner has been implemented. Its performance, including switching speed, accuracy, long-term stability, and oscillation behavior, was extensively tested in a laboratory setting to ensure its efficacy for the task.

During the evaluation, the scanner demonstrated its ability to meet the switching speed requirements efficiently, showcasing stable oscillation behavior. It accomplished the transition between two fields of view in approximately 0.4 ms, as depicted in the bottom left panel of Figure 4.5, with minimal oscillations of 1.2 mrad—equivalent to about one field of view post-telescope beam widening. These oscillations were dampened by a factor of 0.5 within 0.3 ms. Moreover, the tests revealed no significant long-term drift in the scanner's pointing accuracy, ensuring its reliability for extended atmospheric measurement campaigns.

The scanner has been integrated into the core unit of the VAHCOLI system, as shown in Figure 4.6 and 4.8. It is responsible for switching both the field of view of the detection bench and the laser. The distribution of laser beams to the individual telescopes is facilitated by additional mirrors located in the core unit and the MultiFOV upgrade, a schematic drawing of this distribution is shown in Figure 4.5. Control of the scanner is directly managed by the unit's measurement PC, through two analogue signals (θ_1 & θ_2 in Figure 4.5) generated by the measurement cards. This setup ensures precise synchronization of the

scanner's movement with the laser firing, with the additional capability to optimize overshooting of the scanner during switching via optimized control signals generated every 66 ns.
Integrating the scanner and additional optics into the emission compartment of the core unit necessitated a substantial redesign of the system's emission section. Due to space constraints on the original breadboard, the scanner was positioned above the initial optical plane. During this redesign process, a motorized mount for the $\lambda/4$ plate was incorporated, facilitating automated polarization/depolarization measurements.

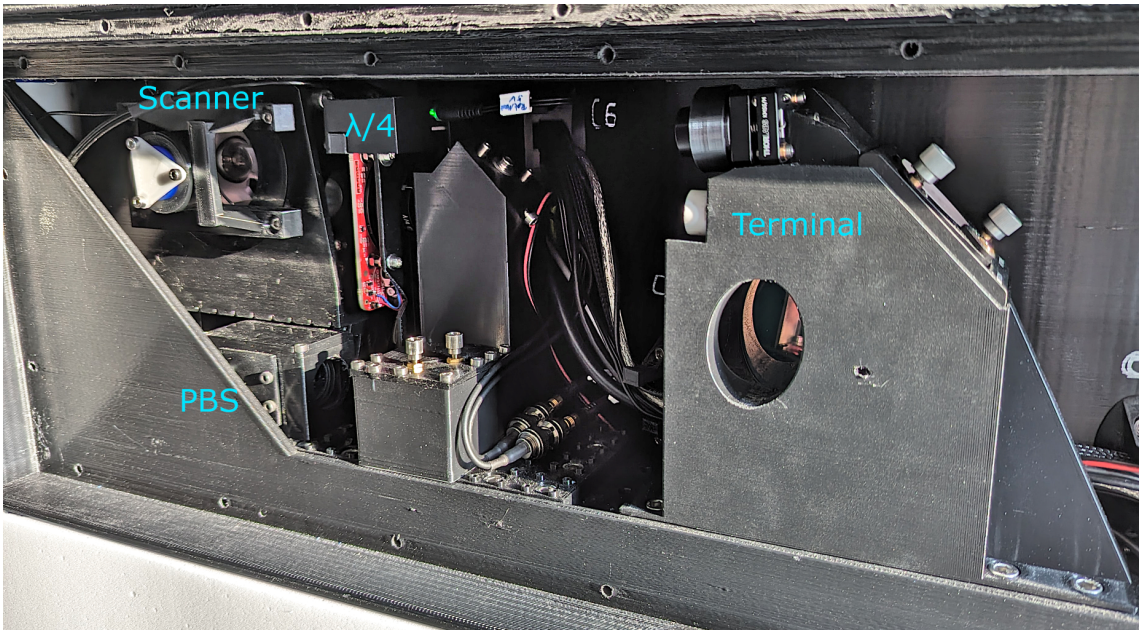

Figure 4.6. Image of the beam switching section as implemented in the VAHCOLI 1 & 2 units. The beam enters the section through the PBS is then diverted upward through the motorised $\lambda/4$ plate and into the scanner. The scanner steers the beam via an elliptical 1-inch mirror onto the different positions of the distribution terminal.

4.5 MultiFOV Housing

The housing for the MultiFOV upgrade of the VAHCOLI instrument was designed using a combination of OpenSCAD and SolidWorks as 3D modeling programs. The L-shaped housing is mounted to the northeast of the core unit, with the telescopes pointing towards north, south, east and west. Its main structural components are two integral telescope holders, one of which is shown in Figure 4.7, each capable of holding two telescopes in an angle of 30° off zenith. These holders are produced using large-scale 3D printing as monolithic parts, eliminating the need for additional assembly steps and thus ensuring the precise positioning of the telescopes once mounted. The telescope holders are affixed to the sides of the core unit, utilizing the existing mounting points originally designed for the system's side panels. For enhanced structural stability, the holders are interconnected using 12 M6 bolts.

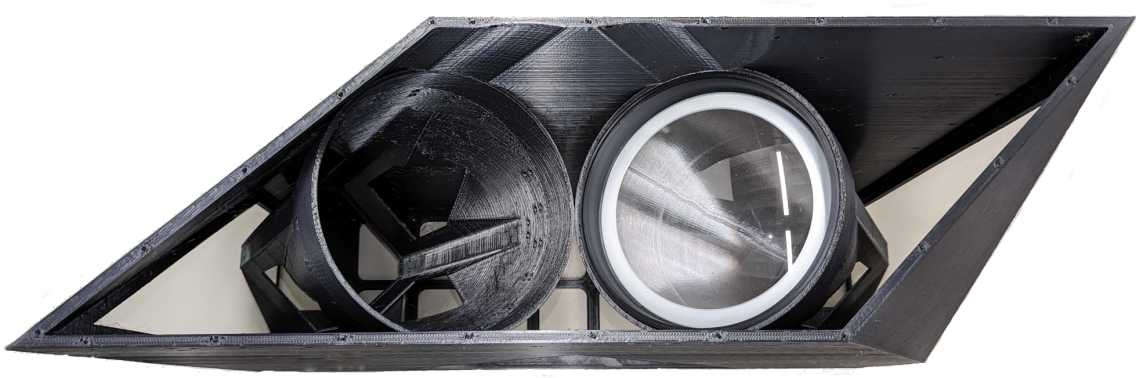

Figure 4.7. Image of one of the monolithic telescope holders of the MFOV upgrade, with one of the lens telescopes installed in the right telescope bay. The 95x28x72 cm piece is 3D printed in 16 days using 17 kg of thermoplastics (BigRep PLX).

The base of the telescope holders is reinforced with two 3 cm thick, 3D printed baseboards, which serve as the mounting platform for the optics responsible for beam distribution. The upper section of the MultiFOV housing is sealed with additional 3D printed panels, equipped with motorised hatches. Surrounding the MultiFOV housing, 3D printed cassettes filled with 2.5 cm thick Basotect insulation material are mounted on all sides for thermal management.
The design of the MultiFOV housing also accommodates space for various additional sensors, such as a weather station, an ADSB antenna for air safety, and extra temperature sensors. To mitigate the risk of overheating during summer conditions, a 120 mm fan is installed on the north side panel. This fan not only cools the housing, but is also strategically positioned to disrupt air turbulence over the telescopes, providing a steady airflow across the front lenses. For use in colder weather, heating strips have been added to the telescope mounts to avoid fogging of the telescope lenses.
Figure 4.8 displays the MultiFOV upgrade as mounted on the VAHCOLI 1 unit, as seen in the left panel. The insulation panels enveloping the entire housing of the upgrade have been fabricated from white PETG, chosen for its high reflectivity. This material choice is critical in minimizing the heating of the housing due to solar radiation. Positioned atop the MultiFOV housing are the additional weather station and ADSB antenna, as depicted. The right panel of Figure 4.8 offers a clear view of the telescope configuration within the housing. The telescopes are oriented at a 30° angle off zenith, with the beams from the north and south, and the east and west beams intersecting. The CAD representation illustrates the laser beams at the center of the lens telescopes. However, during actual operation, the beams exit the lens telescopes off-axis. This off-axis emission is necessitated by the secondary mirror of the vertical telescopes, which would otherwise obstruct an on-axis emission.

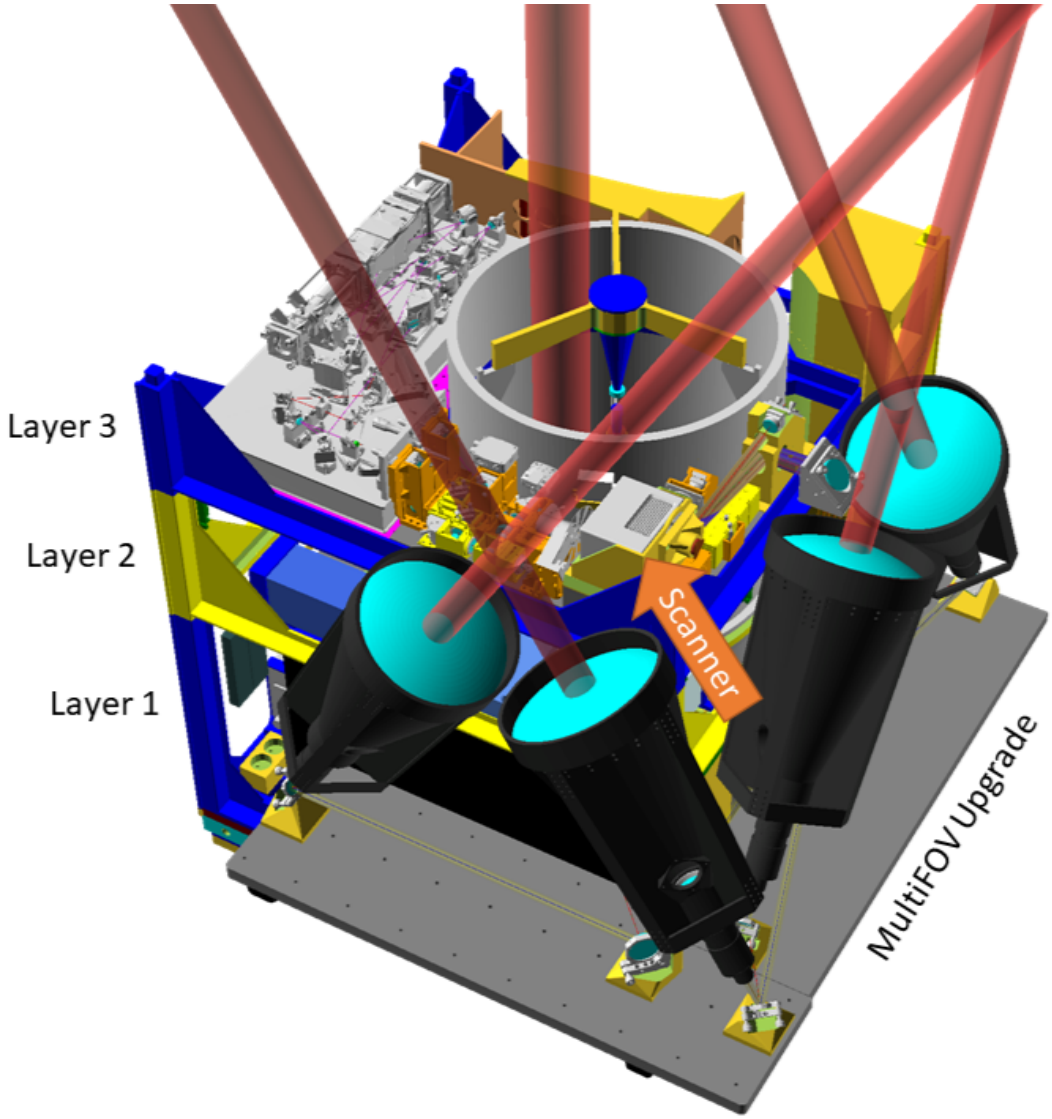

Figure 4.8. Image and CAD drawing of the Instrument with the attached MultiFOV upgrade. **left:** Photograph showing the VAHCOLI 1 unit with the mounted MultiFOV upgrade. In the background the VAHCOLI 0 prototype unit is shown, which lacks the MultiFOV upgrade. **right:** CAD drawing showing the configuration of the MultiFOV upgrade. The position of the scanner is marked. Parts of the core unit, all walls, and the integral telescope holders are hidden for visibilty.

4.6 Further Modifications

The MultiFOV upgrade significantly enhances the VAHCOLI lidar system, yet additional modifications beyond this upgrade have also improved the system's functionality and performance. This section outlines key design changes from the VAHCOLI 0 prototype, which, while not part of the MultiFOV upgrade, have positively impacted the development of the VAHCOLI 1 and VAHCOLI 2 units.

4.6.1 Telescope Temperature Management

Figure 4.9. Parts of the telescope temperature management system. **top:** Tube of the central telescope with the cooling solution installed. **bottom-left:** Macro photography of the black PETG insert, with a cooling channel visible on the left side. **bottom-right:** Macro photography of a piece of the clear PETG telescope wall, showing the rifled microstructure.

In the VAHCOLI 0 prototype, significant thermal challenges were encountered, particularly under summer daylight conditions. The vertical telescope tube experienced temperatures exceeding ambient by over 40 K, leading to a substantial reduction in signal strength. This was primarily attributed to the formation of turbulence inside and above the telescope tube and the resultant deterioration in seeing conditions within the field of view. Addressing this issue was crucial for the development of future systems, necessitating measures to mitigate the excessive heating of the telescope tube by sunlight. While an initial consideration was to change the material used for the telescope's construction to reduce the absorption of sunlight, subsequent laboratory testing indicated that telescope walls with integrated cooling air channels were far more effective in reducing the thermal impact.

In response to the thermal challenges identified in the VAHCOLI 0 prototype, a new design for the telescope tube insert was developed, integrating additional insulation with air cooling capabilities for the telescope walls. This design consists of an inner wall layer made of BASOTECT insulation, secured by a structural component. The structural part, 3D-printed from black PETG, incorporates one of the two cooling channels, as illustrated in the bottom left panel of Figure 4.9. The second cooling channel is formed by placing a thin-walled tube of clear PETG inside the insert, where 3D-printed spacers ensure separation between the clear and black PETG layers. The clear PETG wall is engineered with a distinctive riffled microstructure, illustrated on the right side of Figure 4.9, aimed at reflecting the majority of incoming sunlight back towards its source. This is achieved by alternately shifting the 0.8 mm thick walls by 0.2 mm radially inwards and outwards for every 0.4 mm layer. Consequently, the surface of the cylinder features riffles each with a depth and width of 0.4 mm. This configuration allows the sunlight entering the telescope tube to be either reflected by the rifled clear PETG or transmitted through it, minimizing energy deposition into the material. Light that is transmitted is then absorbed by the black PETG layer behind the clear wall, reducing stray light infiltration. The black PETG layer, which absorbs solar radiation, is cooled by the dual air channels on both sides, effectively dissipating heat and preventing the heating of the clear inner wall of the telescope, thus mitigating turbulence generation.

To prevent the formation of hotspots on the telescope wall, considerable emphasis was placed on ensuring the uniformity of the cooling air stream. This objective was achieved through optimization of the airflow in the 5mm wide cooling channels, using computational fluid dynamics (CFD) simulations. These simulations were conducted with HELYX-OS and OPENFOAM software. Various wall configurations were evaluated until a configuration that yielded a sufficiently homogeneous airflow was identified, as depicted in Figure 4.10. Post-construction of the VAHCOLI 1 unit, the uniformity of the airflow was verified using a hot wire anemometer. Measurements indicated wind speeds within the cooling channels ranging from 0.6 to 1 m/s, achieved using two radial fans to facilitate airflow. Subsequent testing in summer conditions demonstrated that the redesigned telescope wall for the vertical field of view reduced temperatures over ambient by 75%.

Additionally, the tilted lens telescopes of the MultiFOV upgrade have been fitted with this thermal control solution to mitigate turbulence, particularly between the front lens and the middle group. This is crucial for the south-facing telescope, which is at risk of direct exposure to the sun. Without adequate cooling, such exposure could potentially cause the 3D printed body of the telescope to melt.

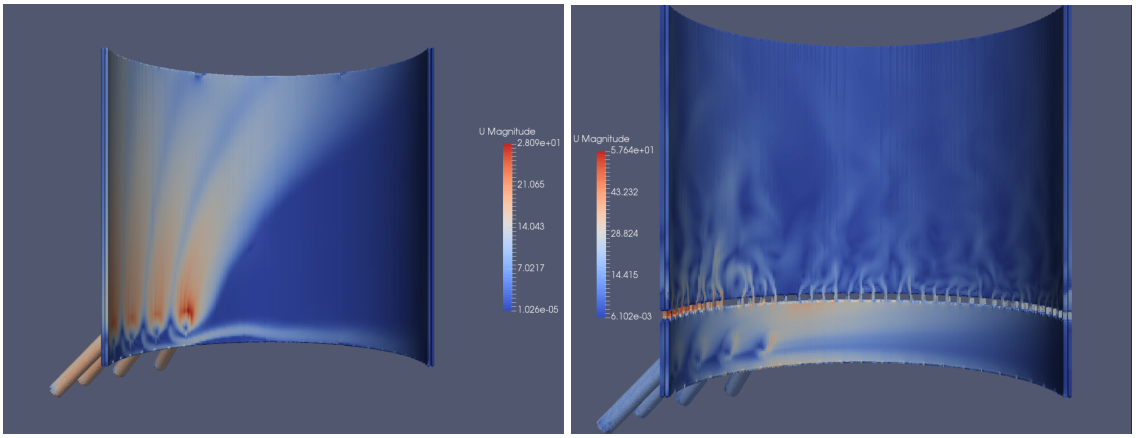

Figure 4.10. Output of HELYX-OS, displaying the results of the OpenFOAM CFD simulations. **left:** Airflow through the double walls without any additional measures taken to generate a homogeneous flow. **right:** Airflow through the double walls with additional nozzles for the homogenisation of the flow.

4.6.2 Vertical Telescope Optimisation

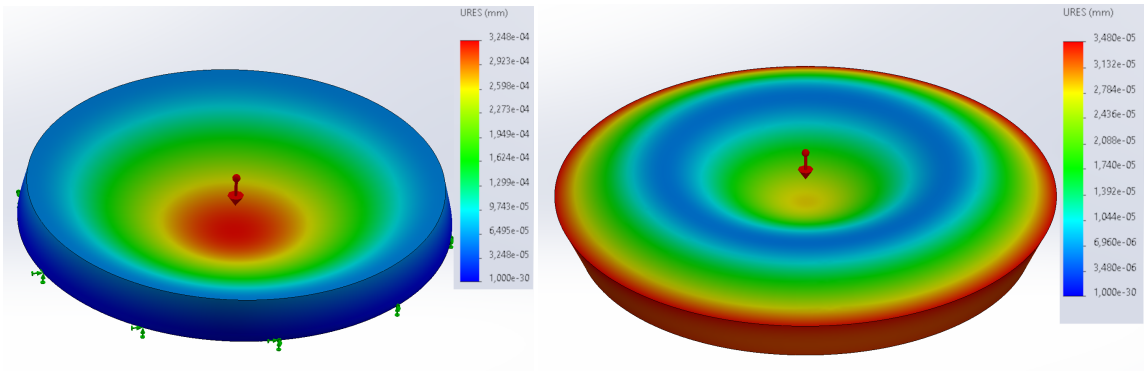

Figure 4.11. Results of the FEM simulations using the simulation suite of SOLIDWORKS 2023 **left:** Mirror deformation when using the old mirror support **right:** Mirror deformation when using the new mirror support.

In the VAHCOLI 1 & 2 units, several improvements have been made to the vertical pointing telescope compared to the VAHCOLI 0 prototype. Alongside the introduction of the turbulence mitigation insert, as detailed in the previous section, the design of the telescope was further refined. The number of spokes holding the secondary mirror and the focus assembly was reduced from four to three, aiming to minimize the obstruction of the primary mirror, as can be seen in Figure 4.9.
Separately, the support structure of the primary mirror was re-evaluated due to concerns identified in the VAHCOLI 0 telescope. In the original design, the support mechanism for the primary mirror was suspected of causing signal loss, potentially due to the mechanical stress it imposed on the mirror. To address this issue, the SOLIDWORKS 2023 simulation suite, utilizing finite element methods (FEM), was employed to analyze the deformation of the primary mirror within its support. FEM simulation results (Figure 4.11) indicated that

the initial support caused a deformation in the primary mirror of approximately 325 nm, about half the wavelength of the laser. Based on these findings, a new support design was developed using FEM simulations, successfully reducing mirror deformation to 35 nm, which is less than one twentieth of the laser wavelength. This improved level of deformation is considered acceptable for telescope operation and was thus incorporated into the construction of the VAHCOLI 1 & 2 units.

4.6.3 Alexandrite Laser and Cooling

For the VAHCOLI 1 & 2 units the design of the alexandrite ring laser has been changed, compared to the two different laser designs which were tested with the VAHCOLI 0 prototype and are described in Froh (2021) and Lübken and Höffner (2021). The changes to the design include the use of a new diode pump module and a significant redesign of the laser oscillator and are detailed in Munk et al. (2023). These changes result in an increased laser power of 1.5 W and 2.4 W respectively in the new lidar units, which translates to an increase of 70% and 174% compared to the 0.875 W generated by the laser last used in the prototype unit, while retaining the excellent spectral properties and the beam quality. The increase in performance in the VAHCOLI 2 laser was accompanied by an increase in the repetition rate from 500 Hz to 750 Hz, which increases the demands on the switching speeds of the scanner. The new lasers utilise water cooling for the temperature control of the alexandrite crystal, and thus the demands on the cooling system of the units is also increased. An active cooling solution is employed using a customised Termotek P802 cooler, which is not only used for the cooling of the laser components, but for the cooling of the entire housing, replacing the previous air cooling solution and resulting in an improved thermal stability inside the unit housing.

4.6.4 Software and Control System Updates

The data acquisition and control software for the new VAHCOLI lidar units has undergone a comprehensive redevelopment, transitioning from RAD Studio 10.3 Rio (DELPHI), which was used in the VAHCOLI 0 prototype, to the Julia programming language (Bezanson et al., 2017). Julia provides notable advantages in terms of usability and performance, on par with languages like C or Rust, making it especially advantageous for scientific computing thanks to its rich package ecosystem for advanced data analysis. This shift has led to a significantly more efficient codebase, reducing the volume of required coding by roughly a factor of five while achieving a twentyfold increase in processing speed for data acquisition and system control. The revamped software is tasked with managing the inputs and outputs of the system's three fast measurement cards from Spectrum Instrumentation, in addition to facilitating real-time data analysis and overseeing closed-loop controls for stabilizing the laser and filters. It's engineered for minimal latency, essential for synchronizing system components, and boasts a response time of 1 ms for closed-loop control actions. To maintain this rapid response in closed-loop operations, the system processes 1.2 GB/sec of data, utilizing complex numerical algorithms to control the lidar, ultimately generating 114 MB/s of data in real-time. The software measures or generates approximately 25 signals, including the two analogue signals for the scanner, with

all system signals synchronized to within a few nanoseconds. Beyond its core real-time functionalities, the software also manages over a dozen auxiliary instruments integral to the lidar's infrastructure, such as weather stations and motors for roof operation, ensuring 24/7 control and system automation.
The updated software now facilitates beam switching for the MultiFOV upgrade, coordinating seamlessly with the power laser's frequency scanning. It oversees a frequency scan cycle that spans 400 frequencies in 0.8 seconds. Following this cycle, the scanner transitions to the next field of view within 1 ms, just in time for the emission of another power laser pulse into the newly targeted field of view. Moreover, the software has been expanded to incorporate data from additional sensors introduced with the MultiFOV upgrade, such as the ADSB antenna, weather station, and camera.
The new software is also tailored towards automatic and unattended operation. Using the data from the weather station on the MultiFOV upgrade, the system can decide independently to start a measurement and to stop it, when the weather conditions prohibit further operations. During operation, the position of nearby planes is continuously monitored using the transponder signals received with the ADSB-antenna and the vertical pointing air safety camera. In case of a plane detected in a radius of 10 km around the instrument, the laser is immediately pointed to a beam dump inside the system using the galvanometer scanner, in order to block the laser and thus prevent any danger by laser radiation for the planes pilots and passengers, while keeping the laser itself running. Once the plane clears the danger area, the laser is automatically released into the sky again.

4.7 Instrument Setup

In preparation for measurements the system is setup up on the test range in Kühlungsborn. The whole system has to be turned around the vertical axis until the instruments north telescope is pointing exactly towards north. This is done using the systems wheels and a compass initially and can be verified by targeting polaris under clear sky conditions at night. For accurate measurements, especially of vertical winds, it is important to ensure the vertical pointing of the telescope. This is done by using an internal 2-axis inclinometer (Posital ACS-080), mounted to the top layer of the instruments frame, and adjustable feet. The feet are then adjusted using a wrench until the inclinometer indicates, that the instrument is perfectly levelled. After the setup, the alignment and levelling of the instrument can be verified using the vertical pointing air safety camera, by taking a picture of the night sky and, from the position of the stars, calculate the orientation of the camera and thus the instrument, using a plate solving software, such as Tetra3 or Astrometry.NET. The used inclinometer provides an accuracy of 0.1° for the vertical pointing and the accuracy of the instruments orientation from plate solving is estimated to be better than 0.2°, based on the pixel size of the camera and the used lens. Since the telescopes themselves are mounted directly in monolithically 3D-printed holders, their pointing accuracy is on the same order as the accuracy of the 3D-printer, which is estimated to be $\sim$2 mrad.
Figure 4.12 shows the system on the test range in Kühlungsborn in operation, after being successfully aligned to north and levelled. The laser beam emitted along the five fields of view is clearly visible.

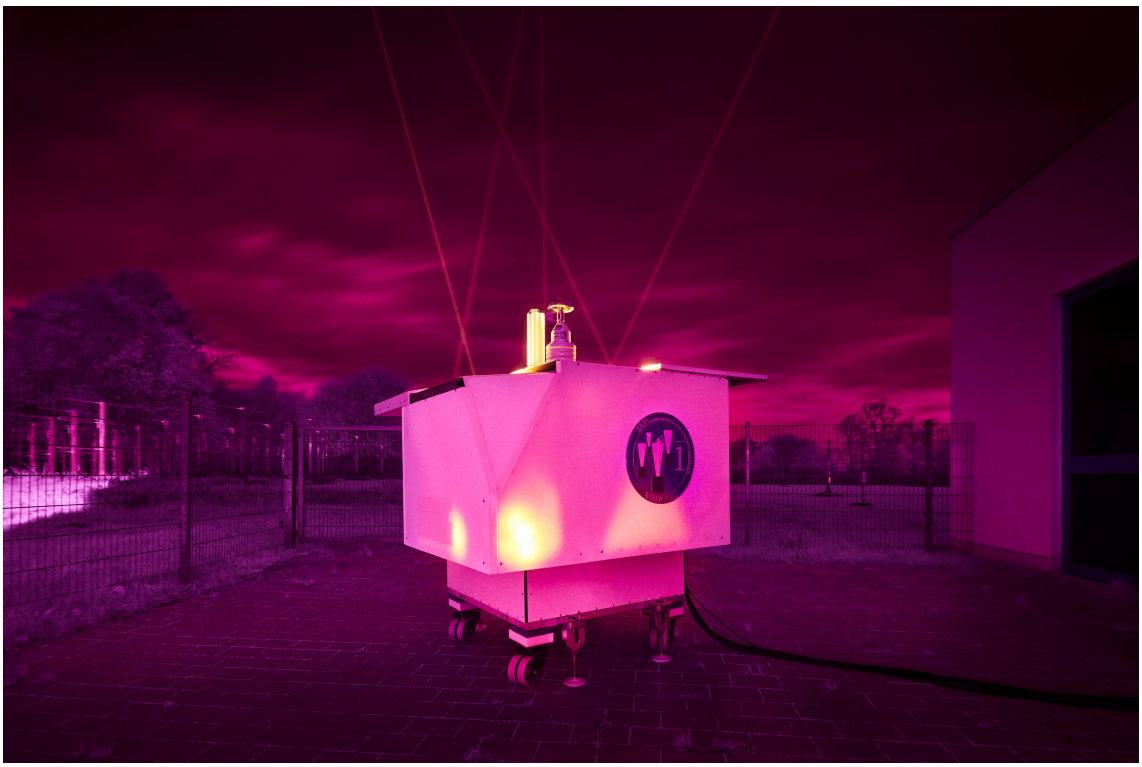

Figure 4.12. Full spectrum photography of the VAHCOLI 1 unit with the mounted MultiFOV upgrade in operation. © Fraunhofer ILT, Aachen / Ralf Baumgarten“

5 | 3D-Wind Measurements Based on Mie-scatter

This chapter is based on the publication Mense et al. (2024).

5.1 Methodology

5.1.1 Retrieval of Horizontal and Vertical Winds from the Lidar Data

VAHCOLI is a frequency scanning lidar, which measures the spectra of the backscattered signal (von Zahn and Höffner, 1996; Höffner et al., 2021; Lübken and Höffner, 2021). For the measurements presented in this chapter, the Mie channel of the system has been used. Mie scattering provides the best wind measurements up to 25 km due to its very narrow spectrum, but is limited in the lower stratosphere by the decreasing concentration of aerosols. Above typically 25 km, the aerosol density drastically drops, giving an upper altitude limit for the use of this method.
For data processing the individual pulse raw data, produced by the system with a time resolution of 2 ms and an electronic altitude resolution of 1 m, are first converted to backscatter spectra with an integration time of 2 minutes and a height resolution of 1 m for each individual field of view. The laser pulse itself has a length of approximately 165m (full width at half maximum) in the atmosphere. In order to improve the statistics for the analysis, these spectra are then integrated in time and altitude with a floating window to the wanted final resolutions of the data. Unless stated otherwise, an integration window of 2 hours and 1000 m is used, which is moved in 2 minute and 100 m steps to take measurements up to 25 km. A shorter integration results in a reduced altitude coverage. Winds are derived from the Mie backscatter spectra by fitting a Voigt-function with a linear background to each height channel, with an example of this fit shown in Figure 5.1. The addition of the linear background in the fitting routine is important, since the background in each altitude channel is not primarily given by the solar radiation or dark count rate of the detectors, but by the altitude dependent Rayleigh backscatter. The laser's spectral shape was determined to be close to a Voigt function with a spectral width of $\approx$ 3 MHz (FWHM) through lab measurements (Munk et al., 2023). The detection filter employed for Mie scattering is a confocal etalon and thus features an airy function as a filter curve, which close to the peak can be estimated by a Lorentzian. The atmospheric broadening, corresponding to wind fluctuations, is simply assumed to follow a Gaussian distribution. Hence, the convolution of a Voigt function, a Lorentzian function, and a Gaussian function yields another Voigt

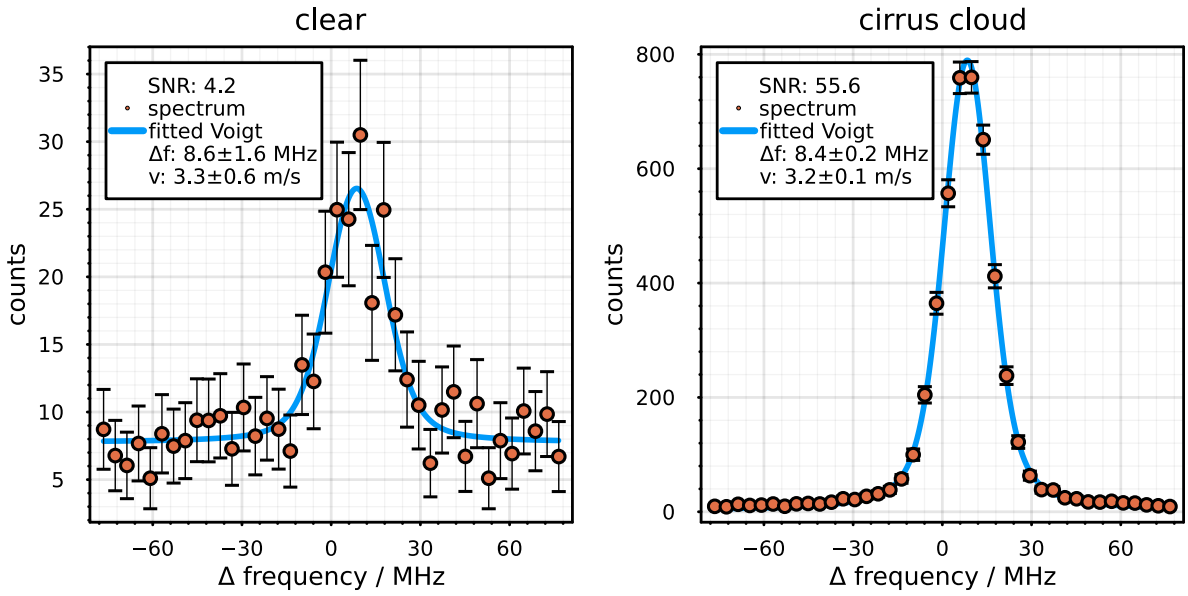

Figure 5.1. Example of the spectrum measured from 9.25 km to 10.25 km with an integration time of 20 minutes in the north field of view, together with the fitted Voigt function in clear air (left) and in a cirrus cloud (right). Corresponding signal-to-noise ratios (SNR = PeakSignal/Background) and errors in frequency offset and winds derived from the fits are shown in the inlets. It is important to note, that the main contributor to the background is Rayleigh scattering and not the solar radiation, due to the strong suppression of the solar background by the confocal etalon.

function. Notably, the instrumental properties such as confocal etalon and laser line shape are measured in parallel to the atmospheric measurements with high accuracy. The analysis can be therefore assume theoretical line shapes as discussed and validate them against the spectra measured in parallel.

From the Doppler-shift, Δf, given by fitting a Voigt function to the measured spectra, the line of sight wind can be derived by rearranging the Doppler-shift equation to $v_{LOS} = \Delta f/(2f_0) \cdot c$ with c the speed of light and f_0 the fundamental frequency (e.g. the laser frequency). This line of sight wind can be decomposed into a vertical and a horizontal component using $v_{LOS} = v_{vert} \cdot \cos(30°) + v_{horr} \cdot \sin(30°)$. Since both the vertical and four off-zenith line of sight winds are measured simultaneously, we can solve for the horizontal component under the assumption, that the vertical wind in the tilted fields of view is the same as in the vertical field of view. This approach is valid for the longer integration times used (≈2 h). It is important to note, that the wind measurement using Mie scattering is based on a relative measurement of the Doppler-shift. This is done by comparing the measured backscatter spectrum to the reference spectrum within the system, as described by Lübken and Höffner (2021). Due to the instruments' capability to do resonance measurements, the laser wavelength of 769.898 nm is known from the usage of potassium saturation spectroscopy as an absolute wavelength reference, even though the Mie-Doppler measurements do not strictly require this precise knowledge of it.

The error estimate for the line of sight winds ($\sigma_{\Delta v}$) is derived from the error estimate of

the Doppler shift ($\sigma_{\Delta f}$) using the propagation of uncertainties ($\sigma_{\Delta v} = \sigma_{\Delta f} \cdot c/(2f_0)$). $\sigma_{\Delta f}$ is a product of the fit routine, which uses the least square fitting of the spectrum, with the standard deviation of each fit parameter being the square root of the corresponding diagonal element of the covariance matrix (Hansen et al., 2013). This requires an estimate for the error of the photon counts, (n), in each frequency bin of the spectrum. For this, a Poisson distribution with a width of $\sigma_n = \sqrt{n}$ is assumed. The precision of the result of the fit benefits from the very narrow spectral shape of the received Mie signal and its high edge steepness which facilitates precise determination of the Doppler shift. Together with the suppression of the background Rayleigh signal, the number of needed photons is significantly reduced to achieve acceptable wind errors compared to traditional DWL systems (Höffner et al., 2021).
Figure 5.2 shows this connection between the measured spectrum of the Mie scattering, the calculated line of sight wind and the error estimate. A change of the peak position in the measured spectrum (top left) results in a change in the calculated wind (bottom left). Black lines in the background of the spectrum correspond to the presence of cirrus clouds, which significantly increase the signal to noise ratio of the spectrum and thus reduce the calculated error of the measurement. This leads to a double distribution of the wind error visible in the bottom right of Figure 5.2. With one peak around 0.15 m s^{-1} produced by measurements with cirrus clouds and one peak around 1.15 m s^{-1} from measurements without cirrus clouds. Figure 5.1 shows an examples of each of these cases. The clear air case shows a low signal to noise ratio of 4.2, resulting in an error estimate of the Doppler-shift of 1.6 MHz and thus a wind error of 0.6 m s^{-1}. In the case of a cirrus cloud the signal to noise ratio drastically increases by more than an order of magnitude, resulting in an error estimate of the Doppler-shift of 0.2 MHz and thus a wind error of less than 0.1 m s^{-1}. In cirrus clouds and other strong aerosol loads the integration in time and altitude can be significantly reduced, while maintaining wind errors below 1 m s^{-1}.

5.1.2 ECMWF and Aeolus Winds

In this work ECMWF winds are utilised in two distinct approaches. Firstly, the ECMWF winds interpolated to the instrument's location are directly (see Fig. 5.4, 5.5 and 5.6). Secondly, to achieve a more comprehensive comparison with the individual fields of view, the ECMWF winds were interpolated and sampled along simulated beams of the lidar measurement (see Fig. 5.2, 5.7 and 5.8). This interpolation and sampling process is very important due to the increasing horizontal distance between the beams at higher measurement altitudes. At a height of 20 km, the separation between two opposite fields of view reaches 23 km, exceeding the ECMWF horizontal resolution of about 9 km. In both cases an observational filter is applied to match the lidars altitude and time resolution.
The Aeolus data has been reprocessed using the Aeolus processing baseline 2B15 and regridded to an altitude resolution of 1 km, as in Banyard et al. (2021). Only Rayleigh-clear winds are used due to the scarcity of Mie-cloudy winds. It is worth noting here, that Aeolus winds and ECMWF winds are not necessarily independent, since Aeolus data was assimilated into ECMWF on a regular basis.

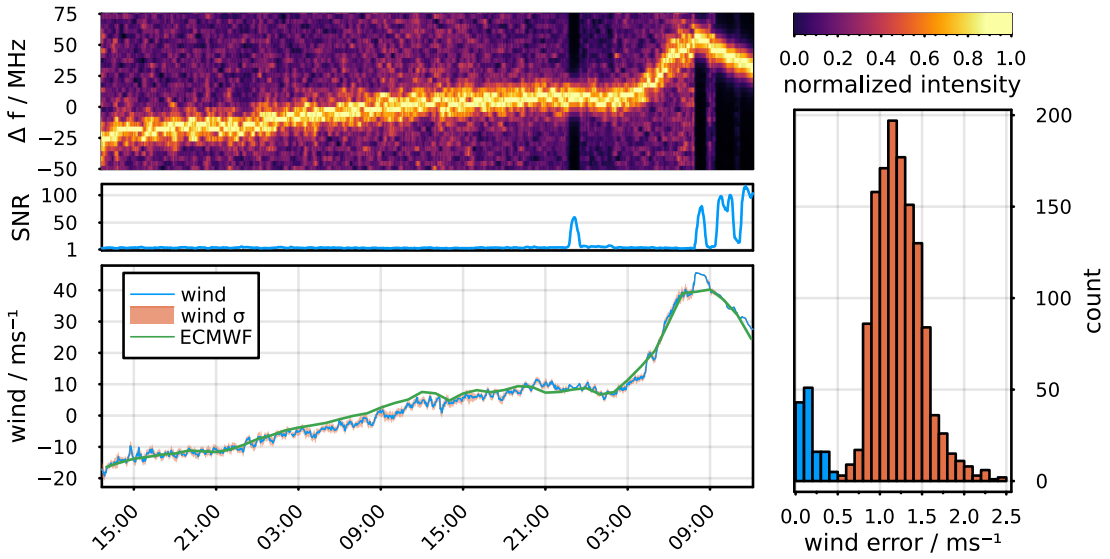

Figure 5.2. Connection between measured spectra, calculated wind and wind error. **top left:** Example of an atmospheric spectrum measured between the 16th and 18th of December 2022 with the north-facing telescope integrated from 9.25 km to 10.25 km, a gridded time resolution of 2 minutes and an integration time of 20 minutes. The purple and black regions in the spectrum plot represent background, comprising mostly Rayleigh scattering. The black corresponds to the cirrus clouds seen in Fig. 5.3 which result in a higher SNR value. **centre left:** Signal-to-noise ratio (SNR) calculated from the spectrum above. **bottom left:** Calculated lidar average wind speed (blue), based on fitting a Voigt function and a linear background to the spectrum, together with the wind error estimate (orange), which most of the time at line strength of the wind speed. The corresponding ECMWF-IFS wind time series is shown for reference (green). A significant deviation of the measured wind and the ECMWF wind is visible at the 18th December around 8:00 UT, probably caused by the much higher smoothing in ECMWF. **bottom right:** Histogram of the error estimate for the wind from measurements with high (blue) and low (orange) aerosol loading.

5.2 Measurement Campaign Description

To acquire the measurements presented in this section, the VAHCOLI 1 instrument was placed outside on a paved and fenced-in area, as described in Section 4.7. During the measurement, the local weather conditions were monitored by a weather station situated roughly 50 m away from the instrument. Over the course of the measurement, the air pressure increased from 1000 hPa to 1024 hPa, the ground temperature was between -2 °C and -8 °C and the relative humidity was high with values ranging between 75 and 100 %.
At the beginning of the measurement, the signal strength of all four oblique fields of view was about a factor of 3 to 4 less than that of the vertical field of view (see Figure 5.3). This is expected due to the smaller size of the lens telescopes. The signal intensity in the meridional fields of view remained relatively stable throughout the measurement period, whereas the zonal fields of view exhibited a pronounced decline in signal strength. This signal decrease was due to icing and condensation occurring on the two zonal pointing telescopes, caused by the cold temperatures and high relative humidity. An internal heating

element was switched on for de-icing around 12:00 UT on the 17th, leading to an increase in the signal of both telescopes. The signal in the westward pointing telescope only recovered to 13 % of its initial value. As a result, our westward zonal winds have a lower top altitude than our eastward zonal winds and both have a significantly reduced performance with more data gaps compared to the meridional telescopes. During this measurement, the planar etalon discussed in section 3.4 was not installed, leading to a slight increase in the daylight background. Despite this, no significant performance drops connected to this daylight background were observed.
Except for the icing problem, the system and the MFOV upgrade performed well with no major problems or interruptions, even under these harsh winter conditions close to the Baltic Sea. After this initial measurement campaign, the VAHCOLI 1 system remained in operation and, as of June 2023, has accumulated more than 600 hours of measurements, of which 85 hours were done in multi field of view mode.

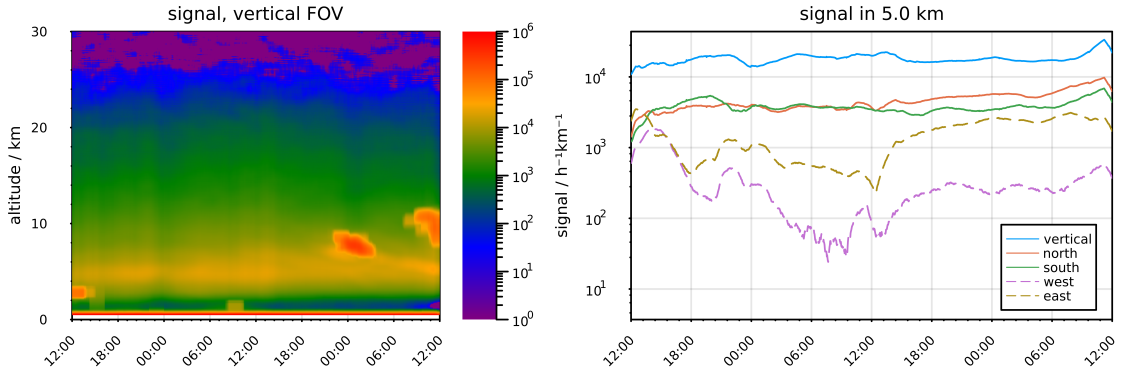

Figure 5.3. Backscatter signal of the vertical field of view (left) and backscatter signal at 5 km in each of the five fields of view (right) from 16 December 2022 12:00 UT to 18 December 2022 12:00 UT. The data is smoothed by the 2 hours and 1 km integration window which is shifted in 2 minutes and 100 m steps. The data is then converted to units of counts per time per altitude. The signal increase at approximately 7-11 km at 00:00 on December 18th is caused by the presence of cirrus clouds, which effectively improves the capability to measure winds with the lidar. Due to a larger aperture the signal from the vertical FOV is generally larger compared to the horizontal FOVs.

5.3 Results

5.3.1 Horizontal Winds

The horizontal winds from all four off-zenith lidar directions are shown in Figure 5.4, as well as the corresponding wind time series from the ECMWF integrated forecast system (ECMWF-IFS) interpolated to the location of the lidar. In the meridional wind, a large change during the measurement is observed, which corresponds to small-scale wind variations associated with the edge of a developing high-pressure region, visible in weather maps of this time period. While at the beginning of the measurement, the meridional winds above 5 km are between 10 m s^{-1} and 20 m s^{-1} (northward), a wind reversal in the

tropopause region is observed, with the winds exceeding -40 m s^{-1} (southward).
In the zonal winds, the previously discussed signal losses are clearly visible as gaps in the top measurement height. Despite the gaps, it was still possible to retrieve zonal wind up to 15 m s^{-1} or higher using the eastward-facing telescope during the majority of the measurement. Here the wind peak in the tropopause region is also visible at the end of the measurement, with winds reaching 40 m s^{-1}.
A first qualitative comparison to the winds from ECMWF-IFS shows the same features in zonal and meridional winds with similar amplitudes. A more quantitative comparison is presented in section 5.3.3.

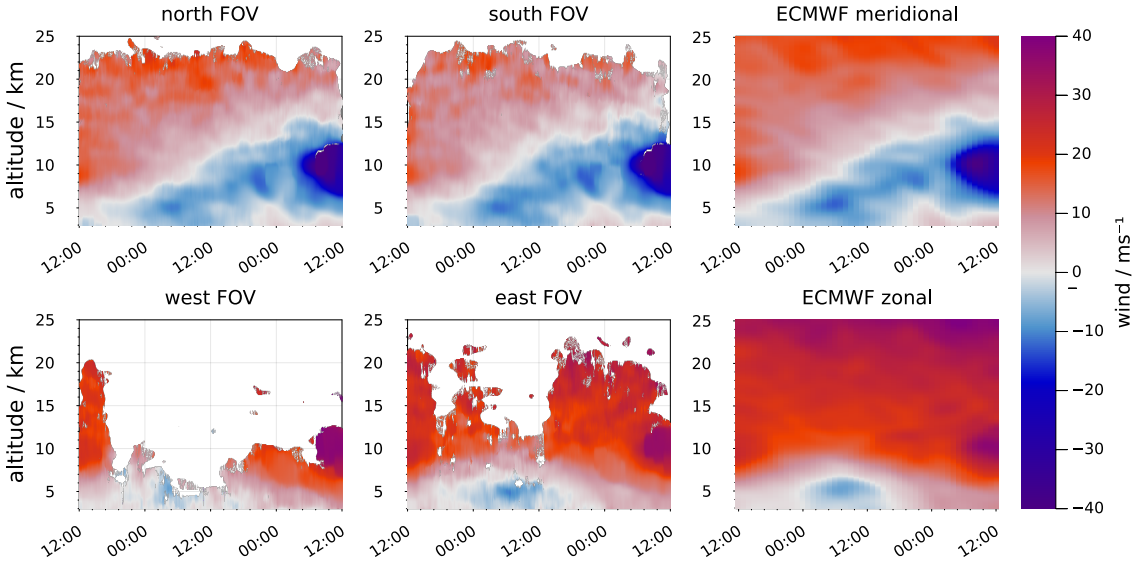

Figure 5.4. Horizontal winds measured between December 16th 12:00 UT and 18th 12:00 UT in the in the north/south/west/east fields of view (see plot titles) using a vertical integration of 1000 m and an integration time of 2 hours. The corresponding meridional and zonal winds from ECMWF are shown in the two right-most panels. The integration window was shifted in 100 m and 2-minute steps. Winds with a line of sight wind error of more than 2 m s^{-1} are masked. Meridional winds show a clear transition around the tropopause from mainly southward winds at the beginning of the measurement to strong northward winds at the end is visible. Gaps in the zonal wind FOVs are caused by reduced signal strength due to icing, affecting especially the higher altitudes.

5.3.2 Vertical Winds

The vertical winds measured are shown in Figure 5.5. Overall, the measured vertical winds show absolute wind speeds of 1 m s^{-1} or less, with a clear separation in the behaviour between the troposphere and the stratosphere. While above approximately 11 km the winds fluctuate due to the passage of gravity waves, below a constant background flow of descending air can be observed. A possible influence of the horizontal winds due to pointing errors will be discussed in Section 5.4. When comparing the measured vertical winds with vertical winds from ECMWF, differences are immediately apparent. ECMWF

underestimates the vertical wind fluctuations by approximately an order of magnitude, which is especially visible in the stratosphere. Additionally, ECMWF does not show the same clear separation between the troposphere and stratosphere.

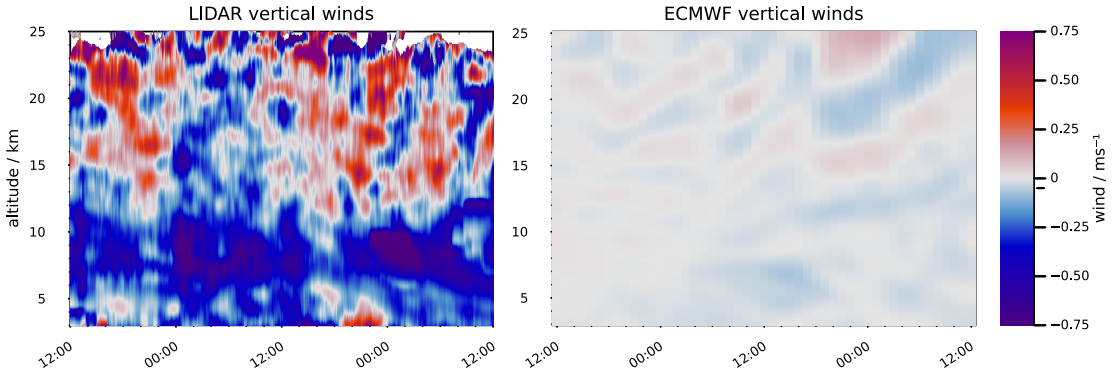

Figure 5.5. Measured vertical winds (left) and the corresponding vertical winds from the ECMWF (right). The vertical winds in ECMWF are underestimated by approximately an order of magnitude. In the upper troposphere a constant background flow of descending air can be observed in the measured winds.

5.3.3 Comparison of Lidar Winds with ECMWF and Aeolus

The comparison of the mean winds during the measurement with the time-averaged ECMWF data over the 48 h of the measurement (see Figure 5.6) shows good agreement of the ECMWF data with the measurement in the meridional direction.
The qualitative comparison presented in Fig. 5.4 shows that the wind pattern observed is similar to the ECMWF zonal wind pattern. In the vertical winds the behaviour discussed in section 5.3.2 is clearly visible, with downward winds in the lower part of the measurements.

The comparison of the meridional winds measured along the north and south field of view (see Fig. 5.7, top left) shows a systematic difference between the two fields of view, with the winds in the north field of view being larger than in the south field of view. This effect increases with altitude. The column mean of the time-averaged difference is 1.32 m s^{-1} with a standard deviation of 0.88 m s^{-1}. The same analysis of the interpolated and beam-sampled ECMWF winds shows a similar trend, but much less pronounced (see Fig. 5.7, top right), with a column mean of the time-averaged difference of 0.32 m s^{-1} and a standard deviation of 0.36 m s^{-1}.
The direct comparison of the time-averaged field of view difference in Fig. 5.8 highlights this. In both the lidar measurements and the ECMWF data, differences of similar altitude dependence are visible, but the difference between the north and south field of view is much more pronounced in the lidar measurements.
The comparison of the meridional winds from the lidar measurement and ECMWF along the individual fields of view (see Fig. 5.7, bottom) reveals a similar pattern. Along the north field of view, the meridional winds measured with the lidar are slightly higher on average than the winds in ECMWF but show excellent agreement in general. The column

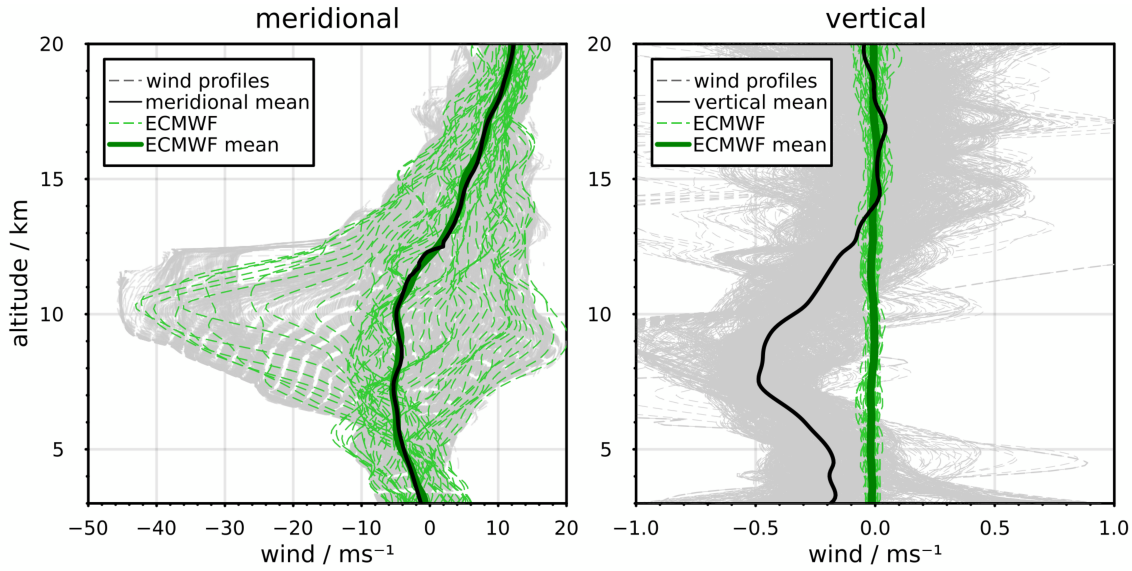

Figure 5.6. Meridional (left) and vertical (right) wind profiles measured (dashed grey lines), together with the calculated mean (thick black line) from 16th 12:00 UT to 18th 12:00 UT, the individual wind profiles from the ECMWF data set (dashed green lines) and the time average ECMWF wind profile (thick green line). The individual wind profiles indicate the variability of the wind during the measurement period, with the highest variability in the meridional winds around the tropopause region.

mean of the difference between lidar and ECMWF winds in the north field of view is 0.30 m s^{-1} with a standard deviation of 0.36 m s^{-1}. Along the south field of view, the lidar measured winds are on average lower than the ECMWF winds, with a column average of -0.93 m s^{-1} with a standard deviation of 0.73 m s^{-1}, and differences are more pronounced in the time resolved heatmap. Especially in the stratosphere, the differences show an altitude dependence, associated with the increase in horizontal distance between the fields of view with altitude. Around the tropopause region, significant deviations are also observable.
For an additional comparison to a Doppler wind lidar, measurements from the Aeolus satellite are used. The closest overpass occurred on 16 December 2022 at 16:40:55 UT over the coordinates (54.615°N, 12.1785°E), so approximately 64 km from the VAHCOLI test site. For the comparison, the VAHCOLI measurements were down-sampled, to match the altitude resolution of Aeolus. The measured wind components were combined and projected to the horizontal line of sight of Aeolus. The distance between the Aeolus position and the location of VAHCOLI 1 has been compensated by a time lag of 96 minutes, based on the observed drift of wind features through the multiple field of view of the VAHCOLI instrument. The comparison (see Figure 5.9) shows good agreement between the projection of the Aeolus HLOS measurement and the projection of the VAHCOLI measurements. Using the 16:40:55 UT profile from Aeolus for statistical analysis of the deviation, like before, results in a standard deviation of 3.31 m s^{-1} and a mean deviation of -0.12 m s^{-1}, with the biggest differences occurring in the stratosphere. The average error estimate of 1.3 m s^{-1} for the projected VAHCOLI wind is by a factor of 2.5 lower than the average error estimate 3.3 m s^{-1} for the Aeolus HLOS wind.

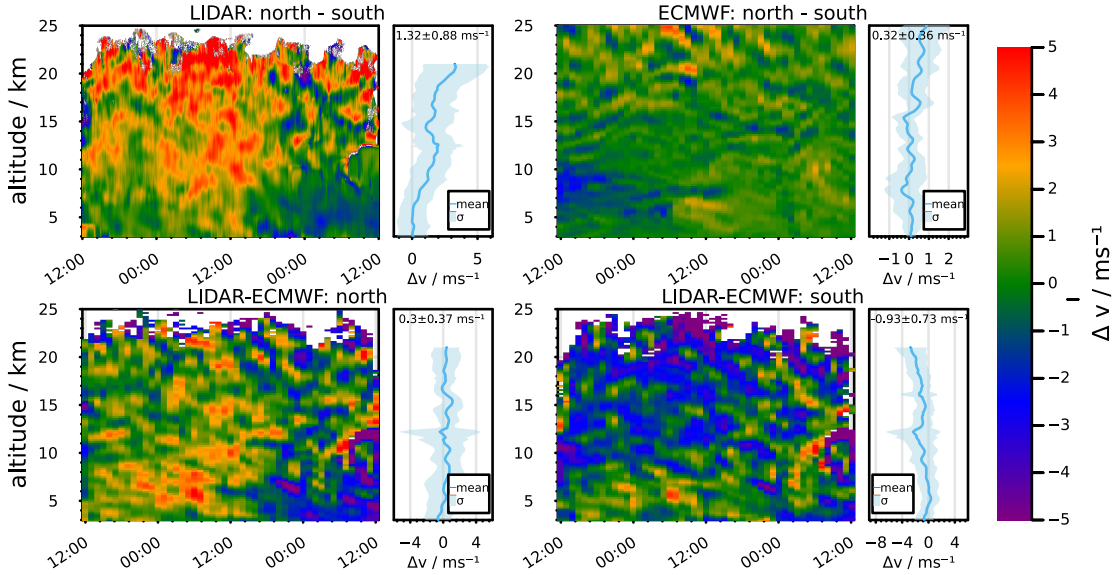

Figure 5.7. Difference in meridional winds (Δv) between 3 and 25 km altitude from 16th December 12:00 UT to 18th December 12:00 UT, with altitude-dependent mean and standard deviation up to 21 km. **Top left:** Lidar's north and south field-of-view difference (Δv = vlidar,north – vlidar,south). **Top right:** ECMWF's north and south FOV difference (Δv = vecmwf,north – vecmwf,south). **Bottom left:** Lidar vs. ECMWF north FOV difference (Δv = vlidar,north – vecmwf,north). **Bottom right:** Lidar vs. ECMWF south FOV difference (Δv = vlidar,south – vecmwf,south).

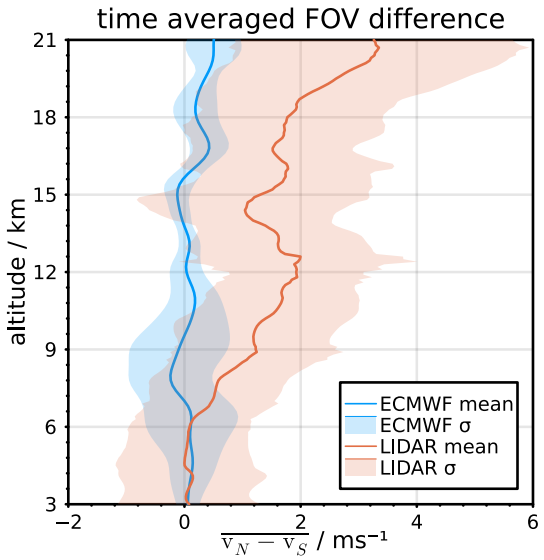

Figure 5.8. Comparison of time-averaged differences between lidar measurements and ECMWF winds along the north and south fields of view from 16th December 12:00UT to 18th December 12:00UT. Blue and orange lines depict mean difference, with shading indicating standard deviation. The lidar data display altitude-dependent asymmetry in meridional winds between the two fields of view.

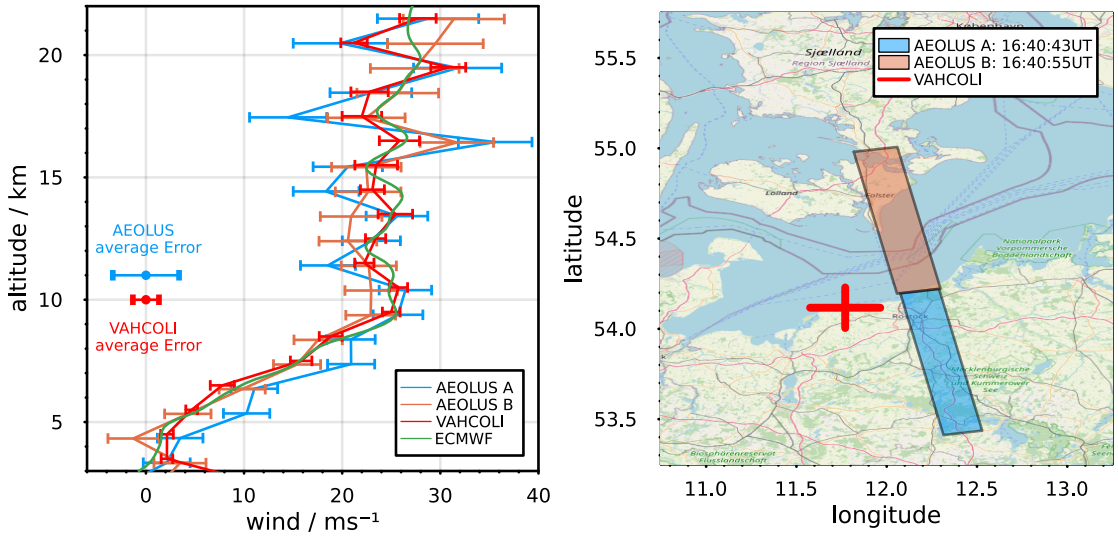

Figure 5.9. **left:** Comparison of the winds measured by Aeolus using Rayleigh scattering (blue and orange line) and Mie winds measured by the VAHCOLI 1 lidar system (red line) together with the winds from ECMWF (green line). The difference of the lidar measurement and the B profile from Aeolus is -0.12 ± 3.31 m s^{-1} on average, with the best agreement below 15 km. The average error for the VAHCOLI winds (1.3 m s^{-1}, red) and the Aeolus winds (3.3 m s^{-1}, blue) are marked. **right:** Map showing the integration areas for the two Aeolus profiles (orange & blue boxes) together with the VAHCOLI beams (red lines) up to a height of 25 km. (Map: © OpenStreetMap contributors 2023. Distributed under the Open Data Commons Open Database License (ODbL) v1.0.)

5.4 Discussion

The lidar measurements during the period from the 16th December 2022 12:00 UT to the 18th December 2022 12:00 UT, were successful with the system operating for more than 48h. The measured winds in the two meridional fields of view show the same wind pattern. The same is true for the zonal fields of view, despite the gaps in altitude coverage. The pointing accuracy of the system's field of views is estimated to be better than 0.5°, based on the internal sensor and the accuracy of the 3D-printed construction. Due to this and the narrow field of view (<30 mrad) a possible contamination of the vertical wind by the horizontal wind components is expected to be less than 0.8% of the horizontal wind speed. This is supported by the vertical winds in the stratosphere above 13 km, which are zero on average, as expected.

Albeit the measured horizontal winds show convincing similarity to the winds reported by ECMWF, both qualitatively and quantitatively, a significant asymmetry of the wind field in meridional direction is observed, which is not well represented in ECMWF. The effect is too large to be caused by a pointing error since for a wind difference of this magnitude between the fields of view a tilting error of 6° is required, which is much larger than our estimated tilting precision of 0.5°. More likely, a true gradient in the wind field above the lidar is observed, associated with the small-scale dynamics at the edge of a developing high-pressure region. ECMWF maps of the meridional wind for the period indicate the presence of such a gradient. It can be concluded that the ECMWF model is underestimating the gradient in the wind field due to its 9 km grid spacing. This highlights the importance of the multi-FOV Doppler lidar to measure variations in the transition region between mesoscale and microscale ($10^3 - 10^4$ m horizontally). The assimilation of higher quality, real-time wind measurements, as provided by a network of ground-based lidar systems, will presumably improve the forecast capabilities of high-resolution numerical weather prediction models, by providing information about these typically inaccessible small-scale processes.

In the vertical winds, there are significant differences between measured and ECMWF winds, with higher fluctuations and systematic deviations, especially in the troposphere. As discussed before it is not likely that a contamination of the vertical winds by the horizontal winds is the cause for these systematic deviations. Additionally, the negative vertical winds in the troposphere are in agreement with the increase in air pressure measured at ground level, discussed in section 5.2. The larger fluctuations in the vertical wind measurements are expected since lidar measurement volume is much smaller than the model cell size (about 9 km x 9 km in this case) and thus captures smaller scale dynamics that are not captured in the model. The different sizes of the sounding volume and the model volume might also explain other differences between the measured data and ECMWF data. This underestimation of vertical wind speeds in ECMWF has also been previously reported and discussed (Preusse et al., 2014).

The comparison to one profile of Aeolus winds shows a good agreement to our measurements with an average deviation of -0.12 ± 3.31 m s^{-1}. These values are well within the values discussed previously by Martin et al. (2021) for the Aeolus measurements. In general, the aerosol-based wind profiles from the VAHCOLI 1 instrument cover a larger altitude range than the Rayleigh winds from Aeolus. The VAHCOLI instruments have

been purposefully designed to integrate seamlessly into a European lidar network in the foreseeable future. Even though IAPs goal for this network is to observe crucial dynamical processes in the middle atmosphere (10-100 km), such as gravity waves and stratified turbulence with sufficient temporal, vertical, and horizontal sampling and resolution, it is also exceptionally well-suited to complement forthcoming Aeolus successor missions (Lübken and Höffner, 2021). While the satellites acquire top-down measurements and sparsely sample multiple locations, the VAHCOLI instruments adopt an Eulerian reference frame, observing the atmosphere from the ground up and offering continuous measurements. The assimilation of both the global wind measurements from satellites and the ground-based lidar network measurements into forecast models such as ECMWF promises significant enhancements to their capabilities, owing to the inherent complementarity of these datasets.

6 | Observation of Aerosol Properties

Aerosols play a crucial role in the physics and chemistry of the atmosphere. In the stratosphere, sulfate aerosols are generally considered the primary contributors to aerosol load. These aerosols impact the Earth's radiative balance, influencing atmospheric dynamics by inducing a negative radiative forcing, which leads to surface cooling (Robock, 2000; Timmreck, 2012). Stratospheric sulfate aerosols are also significant for atmospheric chemistry as they provide surfaces for heterogeneous chemical reactions and act as nuclei for the formation of polar stratospheric clouds (PSCs). These clouds are critical in the depletion of stratospheric ozone during winter and spring at high latitudes (Tritscher et al., 2021b). A relatively new field of research is the effect of spacecraft reentry on aerosols in stratosphere and mesosphere. When spacecraft or other debris re-enters the atmosphere, they produce metal vapours which condense into aerosols, adding anthropogenic material to meteoric smoke particles (MSP). Already today, measurements show that about 10% of the aerosol particles in the stratosphere contain anthropogenic material (Murphy et al., 2023). The effect of this is still unknown. Together with the ever rising amount of rocket launches, this calls for long term observations of aerosol properties.
For temperature measurements using Rayleigh-lidar, precise knowledge of aerosol contributions to the overall backscatter is required, as uncorrected aerosol influence can significantly bias temperature readings, as demonstrated in Chapter 7. It is thus of high interest to measure different aerosol properties using lidar.

6.1 Methodology

6.1.1 Retrieval of the Mie to Rayleigh Backscatter Ratio

For the retrieval of aerosol properties, such as the Mie to Rayleigh backscatter ratio (BSR), from lidar measurements, it is necessary to distinguish between backscatter originating from molecules and from aerosols. The VAHCOLI instruments accomplish this task by leveraging the spectral properties of the two distinct scattering mechanisms, utilizing the optical splitting method as described in Section 3.4.2. Examples of the resulting spectra on detectors APD1 and APD2 are depicted in Figure 6.1.
The spectra measured with APD1 contain both the Mie-signal and Rayleigh-signal transmitted through the confocal etalon, along with the signal from the dark count rate of the APD. Due to the ultra-narrowband filtering of this channel, the solar background is significantly lower than the dark count rate and is thus negligible. As discussed in Froh (2021), the spectral filters are tailored to the spectral properties of the scattering processes,

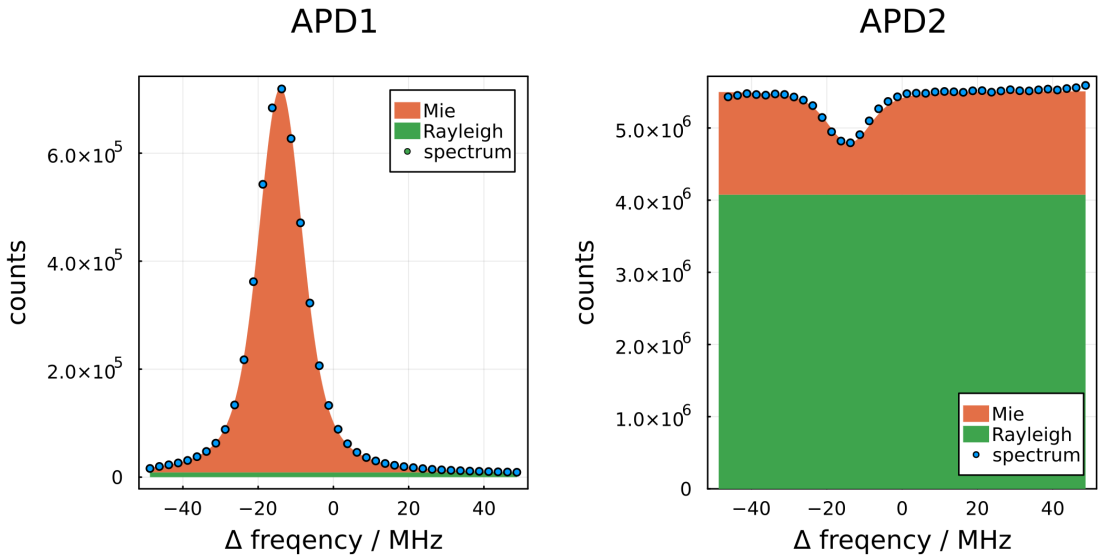

Figure 6.1. Spectra measured with APD1 (left) and APD2 (right) in 10±0.5 km altitude on the 8th of February at 0:00 UTC. The estimated contributions of Mie- and Rayleigh-scattering are color coded. Here the background is negligible, since the signal is high and the measurement was done at night.

such that the Rayleigh-signal transmitted onto APD1 forms a frequency-independent background. This background is highlighted in green in the left panel of Figure 6.1.

The spectra measured with APD2 consist of the signal from Mie-scattering and Rayleigh-scattering as reflected on the confocal etalon, the dark count rate, and, depending on the use of a solar suppression filter, the solar background. When aerosols are present, a spike in the spectrum measured on APD1 is visible, corresponding to a dip at the same wavelength in the spectrum of APD2, as illustrated in the right panel of Figure 6.1. Due to the theoretical maximum transmission of 50% through the confocal etalon, this dip has a depth of about half the total aerosol signal in one frequency bin. Since the Rayleigh signal is much stronger on APD2, this effect can only be observed under strong aerosol loads.

In general, the aerosol load can be determined by comparing the peak signal with the signal in the wings of the spectrum measured with APD1. In the absence of aerosol load, the spectrum appears flat with only the frequency-independent Rayleigh background. Every significant peak observed on top of this background can be attributed to Mie-backscatter. For an increased altitude coverage, the routine for retrieving the BSR uses both measured spectra from APD1 and APD2, with the constant background from the APDs' dark count rate and the solar background removed. Figure 6.2 shows the steps from the initial altitude-dependent spectrum to the BSR.

First, a Mie-signal and a Rayleigh-signal are extracted from the APD1 spectrum using three windows, as shown in the bottom left panel of Figure 6.2. These windows are chosen based on the results of the Voigt-fit, previously performed for the wind measurements. The width of the center window is selected to be twice the average FWHM of the peak, thus containing approximately 96% of all photons received from Mie-backscatter. All photons within the center window are summed up to give the signal $P_{1,c}$. For the outer two

windows, all photons are summed up, and the resulting signal is corrected for the different spectral widths of the windows, giving $P_{1,Ray}$. The difference of these two signals contains the majority of the Mie-backscatter contribution to the spectrum of APD1:

$$P_{1,Mie} = P_{1,c} - P_{1,Ray} \tag{6.1}$$

As visible in green in the centre panel of Figure 6.2, the Rayleigh signal from APD1 ($P_{1,Ray}$) drops off typically above 20 km, due to the strong blocking of the Rayleigh signal by the confocal etalon, which results in the removal of the Rayleigh signal together with the background from the APDs' dark count rate. To calculate the BSR higher up, the signal from the APD2 is used, since on this detector, the Rayleigh backscatter is not blocked, resulting in a significantly higher signal and thus better statistics. Spectrally, not the whole APD2 spectrum is summed up for the signal, but only the previously defined outer windows, to avoid the dip shown in Figure 6.1. The signal from APD2 is scaled to $P_{1,Ray}$ at an altitude of 15 km to yield $P_{2,total}$.

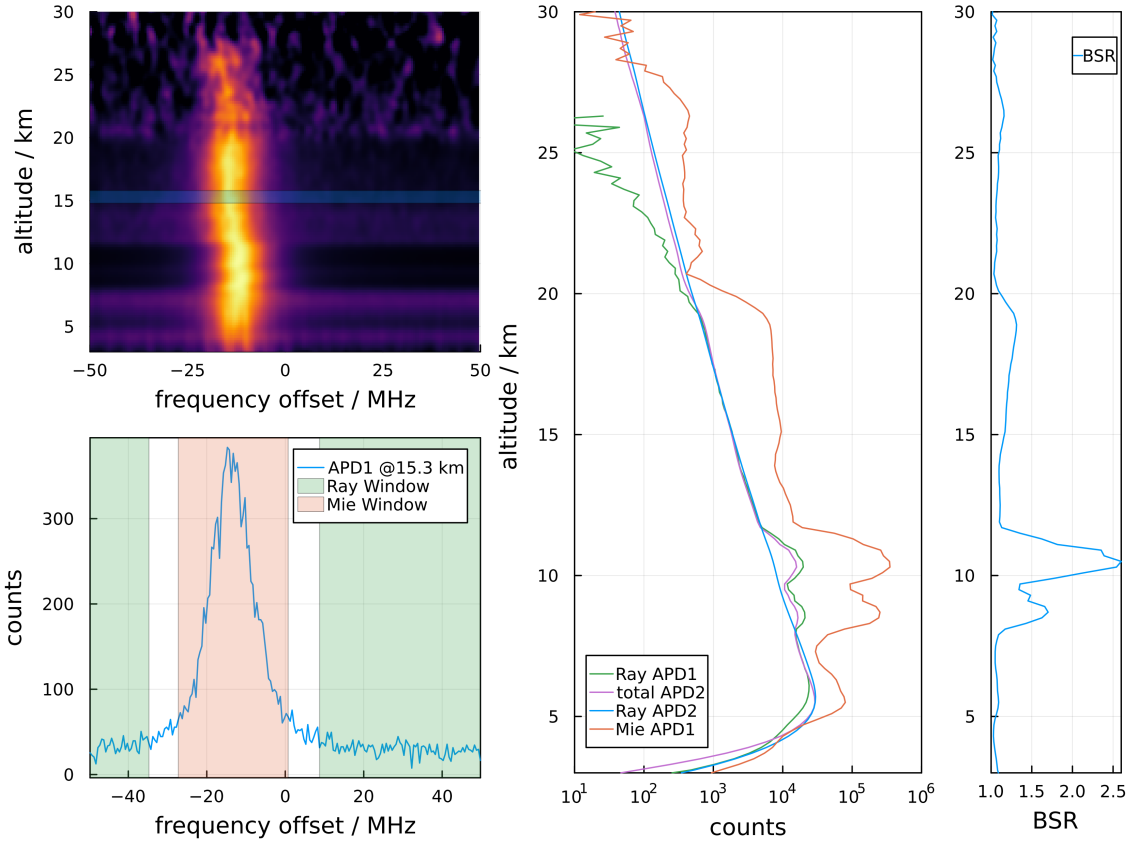

Figure 6.2. Connection between the measured spectra and the retrieved BSR. **top left:** Example of an atmospheric spectrum measured using APD1 of VAHCOLI 1 on 28 February 2023 between 19:30 UT and 22:30 UT with the vertical pointing telescope. A vertical integration window of 1 km was used, which was shifted in 200 m steps. **bottom left:** Spectrum measured on APD1 in 15.3±0.5 km. The windows used for the retrieval of the Mie and the Rayleigh signal is marked in orange and green. **centre:** Signals used for the calculation of the BSR. **right:** Calculated BSR profile.

Traditionally, the BSR is defined as:

$$R_A = \frac{P_{Ray} + P_{Mie}}{P_{Ray}} = \frac{P_{total}}{P_{Ray}} \tag{6.2}$$

where P_{Ray} and P_{Mie} represent the Rayleigh and Mie components of the backscatter, respectively, and P_{total} is the sum of these components.
For the two channel VAHCOLI instrument R_A is initially estimated in the processing routine using:

$$R_A = \frac{P_{1,Mie}}{P_{2,total}} \cdot \frac{1}{\zeta \cdot \eta} + 1 \tag{6.3}$$

Two correction factors, ζ and η, are required for an accurate estimation of the BSR. ζ is determined by the ratio of Rayleigh suppression in the spectra measured with APD1, and can be determined either numerically or experimentally (to be discussed later). η is based on the ratio between the peak height of the Mie peak and $P_{1,Mie}$, and is calculated by the processing routine using the fit results and the window width of the Mie window. While the typical value for η is 0.5, effects such as spectrum broadening or changes in the window size can significantly alter it.
Given that the BSR is estimated using $P_{2,total}$, which includes both Rayleigh and Mie components of the backscatter, the BSR is systematically underestimated. By rearranging the definition of BSR to

$$P_{2,Ray} = \frac{P_{2,total}}{R_A} \tag{6.4}$$

it is evident that $P_{2,total}$ can be corrected with the estimated BSR and then used again to calculate the BSR. By repeating these steps, the estimations for BSR and the clean Rayleigh signal converge towards the correct BSR and clean Rayleigh signal after a few iterations (less than 10). The resulting BSR is illustrated in the right panel and the cleaned Rayleigh signal in the center panel of Figure 6.2 in blue.

Numerical determination of ζ

The correction factor ζ is given by the differential peak transmission through the confocal etalon of Mie-scattering and Rayleigh-scattering. For the spectrally narrow Mie-scattering, the transmission can be determined numerically by convoluting the laser's Voigt profile with the filter's Airy function. For the transmission of the spectrally broader Rayleigh scattering, the periodicity of the confocal etalon's transmission curve must be considered, as the spectral width of the Rayleigh-scattering spans multiple free spectral ranges of the confocal etalon. Utilizing the precise measurements of the spectral shapes of the filter curves and the laser obtained during lidar operations, the transmission of Mie- and Rayleigh-scattering can be accurately determined using a numerical simulation, and hence ζ can be calculated from their ratio. The theoretical foundation of the numerical simulation is discussed in great detail in Froh (2021).
Figure 6.3 presents the result of the numerical simulation using typical parameters measured during the operation of the VAHCOLI 1 instrument. Displayed in green are the resulting spectral transmission curves through the confocal etalon. The total transmission

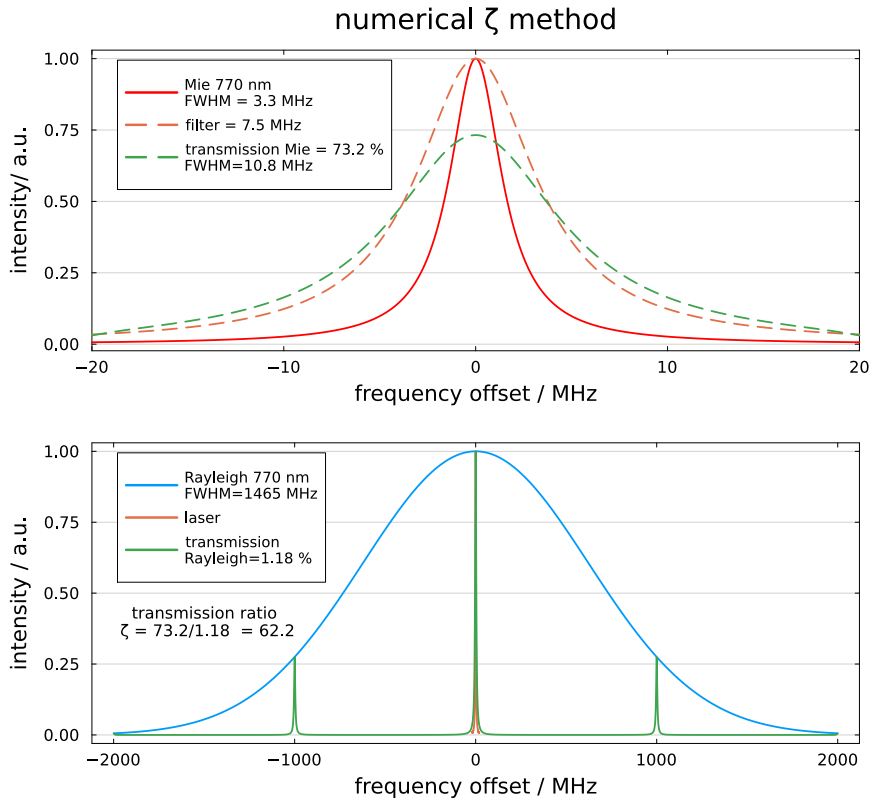

Figure 6.3. Example of the numerical method used to determine ζ.

is determined by integrating these curves. From the simulation of the Mie-transmission depicted in the top panel of the figure, a transmission of $t_{Mie} = 73.2\%$ is found. From the simulation of the Rayleigh-transmission, a value of $t_{Ray} = 1.18\%$ is determined. Thus, ζ is the ratio of the two, $\zeta = t_{Mie}/t_{Ray} = 62.2$. This result can also be interpreted as a suppression of the Rayleigh-signal in the Mie-channel by a factor of 62.2.

Experimental determination of ζ

For the experimental determination of ζ, the property of Rayleigh-scattering being proportional to the air density is exploited. Air density decreases with altitude exponentially as given by

$$\rho(z) \propto e^{-\frac{z}{H_p}} \tag{6.5}$$

which implies that the Rayleigh signal must exhibit a similar shape, with only minor deviations attributable to temperature variations. This characteristic facilitates a straightforward approach to determine ζ. The initial step is to use a profile $P_{2,total}$ from a measurement that includes aerosols, such as thin cirrus clouds, ensuring to select aerosol loads that do not saturate the APD, i.e., with count rates less than 1 MHz. The pure Rayleigh signal is then calculated using equations 6.2 and 6.4, iteratively adjusting ζ until the curvature of $\ln(P_{2,Ray})$ is minimized. An example of this method is illustrated in Figure 6.4.
In this case, a ζ value of 60 yields an effective correction of the visible aerosol contribution

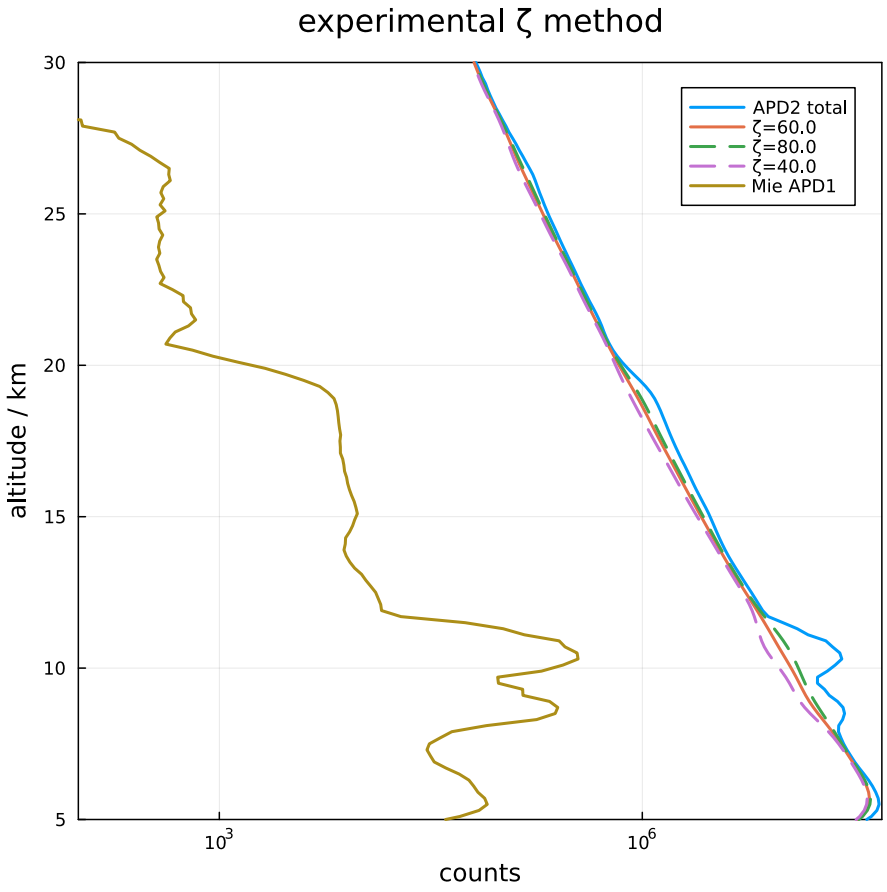

Figure 6.4. Example of the experimental method used to determine ζ.

to the APD2 signal. Based on several independent retrievals of ζ using this method, a value of $\zeta = 60 \pm 5$ is estimated, which aligns well with the results obtained from the numerical method.
This experimental method for retrieving ζ has the advantage of incorporating instrumental effects that are challenging to assess numerically, such as alignment discrepancies in the filters.
Regardless of the chosen method for estimating ζ, the same value can be applied to subsequent measurements as long as the system configuration remains unchanged.

6.1.2 Calculation of Aerosol Backscatter Coefficients

Utilizing the Mie to Rayleigh Backscatter Ratio, the backscatter coefficient of Mie scattering is determined using

$$\beta_{Mie}(z, \lambda) = \beta_{Ray}(z, \lambda) \cdot (R_A(z) - 1), \tag{6.6}$$

where $\beta_{Ray}(z, \lambda)$ represents the backscatter coefficient of Rayleigh scattering. The backscatter coefficient for Rayleigh scattering, $\beta_{Ray}(z, \lambda)$, can be derived for dry air from a number density profile $n(z)$ and the molecular backscattering cross-section $\sigma_\pi^R(\lambda)$, which is calculated using Equation 2.7.

Hence, the backscatter coefficient is given by

$$\beta_{Ray}(z, \lambda) = n(z) \cdot \sigma_{\pi}^{R}(\lambda) \tag{6.7}$$

(Measures, 1984, p.42). The number density, $n(z)$, can be obtained from an external source, such as radiosonde measurements or an atmospheric model, or best directly from the pure Rayleigh signal of the lidar measurement, adjusted to match a reference density profile. In this study, densities from ECMWF were employed to mitigate biases introduced by the correction of the overlap function, as elaborated in section 7.1.

6.2 Measurement Campaign Description

The data used for the results discussed in this chapter were primarily collected during the December 2022 campaign, as elaborated in Section 5.2. Additionally, the chapter includes observations from February 2023, a period during which the VAHCOLI instrument was predominantly configured for observations in the vertical field of view. Notably, the system operated largely autonomously during this time, automatically initiating and concluding measurements based on the assessment of favorable weather conditions. Despite this advanced operational mode, the measurement efforts were occasionally compromised by less-than-ideal weather conditions, including the frequent presence of cirrus clouds and other tropospheric cloud formations, which intermittently obstructed the data collection process.
Despite the imperfect conditions, the measurements from February are particularly noteworthy due to the occurrence of exceptionally low temperatures (below 190 K) around 20 km altitude during this period. These low temperatures can lead to the formation of Polar Stratospheric Clouds (PSCs), making the observations from this time period especially valuable.

6.3 Results

6.3.1 December 2022 Campaign

Mie to Rayleigh Backscatter Ratio

The Mie to Rayleigh backscatter ratio (BSR) calculated for the vertical field of view is presented in Figure 6.5 for two consecutive nights between the 16th and 18th of December. An integration time of 12 hours has been applied, allowing the BSR values to be interpreted as the nightly average. A vertical integration window of 1000 m, shifted every 200 m, was employed. The calculated BSR profiles for both nights are similar above 12 km, exhibiting a local maximum in the stratosphere at around 20 km altitude. Minor differences are noted in the slope above 20 km, where the first night displayed a more gradual slope compared to the second night. In the troposphere, the largest deviations between the two profiles were observed. On the first night, a minimal BSR of less than 1.025 was recorded at approximately 8 km altitude, whereas on the second night, the presence of a cirrus cloud induced a pronounced maximum in BSR, reaching 2.8 at this altitude. Below 5 km, the

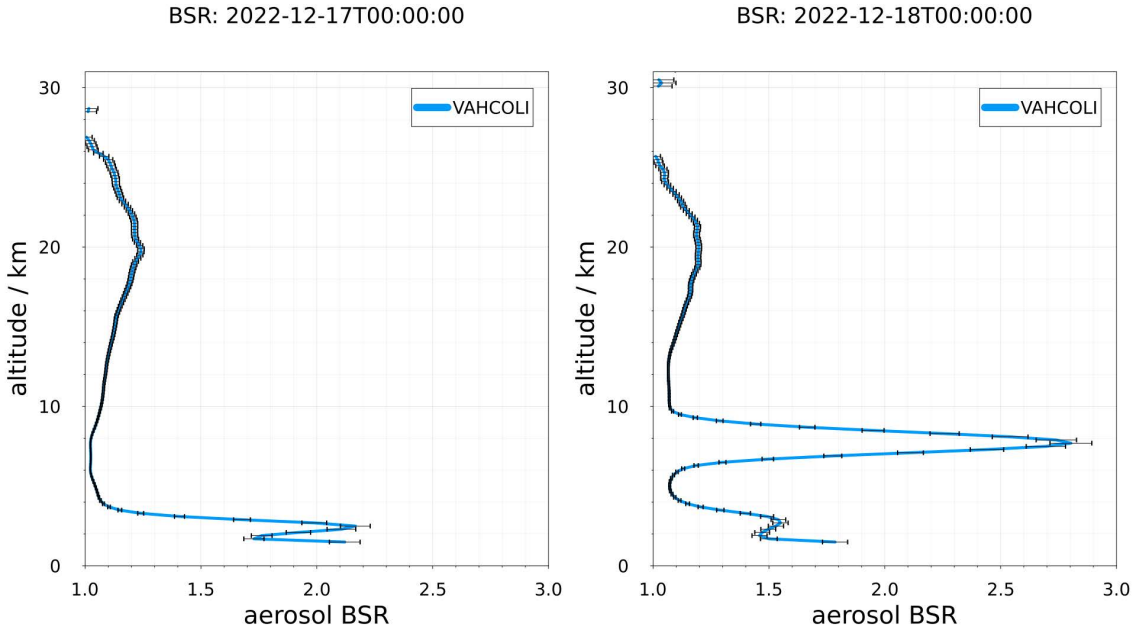

Figure 6.5. Mie to Rayleigh backscatter ratio measured on the nights of 16th-17th December 2022 (left) and 17th-18th December 2022 (right), integrating over 12 hours with a vertical integration window of 1000 m, shifted every 200 m. The occurrence of a cirrus cloud around 8 km on the second night is clearly visible. In the stratosphere, the backscatter ratio peaks around 20 km.

BSR increases again with decreasing altitude, with several local maxima indicating the presence of layered structures within this altitude range. Below 2 km, the system's chopper is fully closed, and thus, no BSR measurement is available.
Figure 6.6 illustrates the temporal evolution of the BSR using an integration window of 3 hours and 1000 m, which is shifted in 1-hour and 200 m increments. Similar to the nightly averages, the local maximum of the BSR in the stratosphere is visible as a band around 20 km. The temporal evolution exhibits significant variability at this altitude, with BSR fluctuating between 1.16 and 1.3. High BSR values appear as patches drifting through the field of view, with the temporal mean BSR at 20 km height being 1.21 ± 0.03. The vertical extent of this band, with a BSR above 1.15, shows considerable variability. In the troposphere, a region of low BSR is observed at the beginning of the measurement period between 5 and 9 km. Subsequently, the emerging cirrus clouds are distinctly visible within this altitude range. The BSR of these cirrus clouds exceeds 1.3, rendering their structure indistinguishable in this plot.

Aerosol backscatter coefficient

Utilizing the BSR calculated previously, the backscatter coefficient for Mie scattering (BSC) was derived as outlined in Section 6.1.2.
Figure 6.7 displays the BSC for the vertical field of view over the course of two nights, from the 16th to the 18th of December. An integration time of 12 hours was applied, rendering the BSC values representative of the nightly average. A vertical integration window of

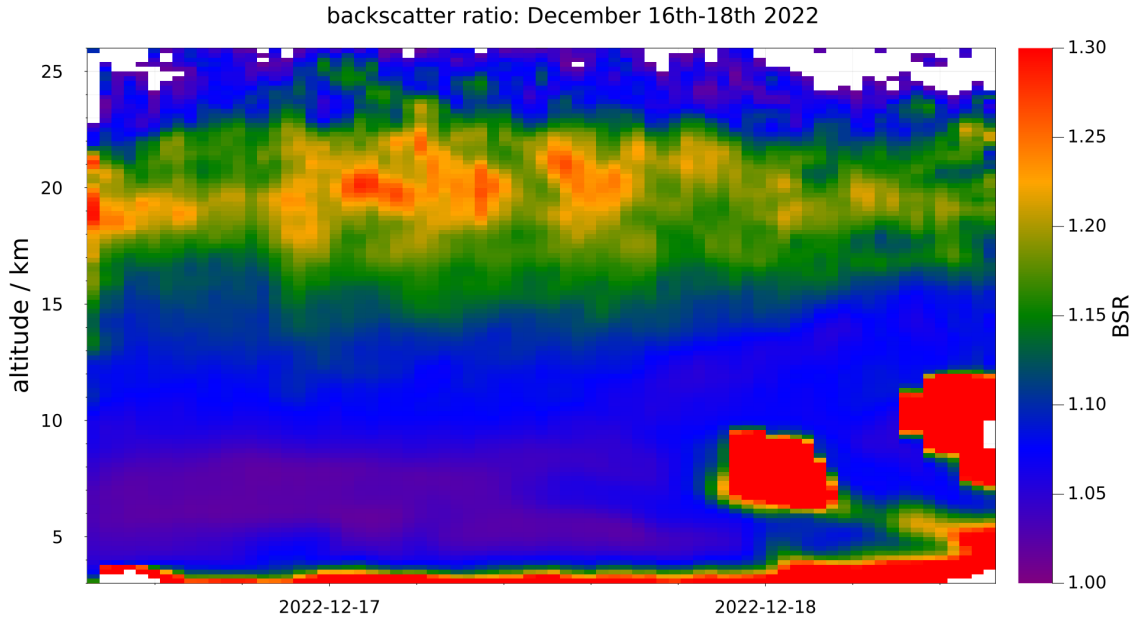

Figure 6.6. Mie to Rayleigh backscatter ratio measured from 12:00 UT on December 16th to 12:00 UT on December 18th, with an integration time of 2 hours and a vertical integration window of 1000 m, shifted every 40 minutes and 200 m. The peak of the backscatter ratio around 20 km is consistently visible throughout the measurement period. Cirrus clouds are notably present in the night from the 17th to the 18th of December.

1000 m, adjusted every 200 m, was utilized. Unlike the BSR, the BSC does not exhibit a well-defined maximum around 20 km for either night. Instead, the BSC remains relatively constant between 10 and 20 km, averaging $7.01 \pm 0.53 \times 10^{-6}$ km^{-1}sr^{-1} on the first night and $6.12 \pm 0.74 \times 10^{-6}$ km^{-1}sr^{-1} on the second night. Above 20 km, the BSC rapidly decreases, reaching values in the order of 10^{-7} km^{-1}sr^{-1} at altitudes above 25 km, where reliable BSC calculations were not possible. The orange curve in Figure 6.7 represents the October-December average of the aerosol backscatter coefficient provided by James Brooke, as computed using the WACCM-CARMA model (Brooke et al., 2017). Given the variability of stratospheric aerosols, the model data reasonably match our measurements, with the most notable difference being the slope above 22 km. On the second night, the appearance of a cirrus cloud around 8 km is evident as a peak with a maximum BSC of 2×10^{-4} km^{-1}sr^{-1} and a vertical extent of ± 1 km.

Figure 6.8 depicts the temporal evolution of the aerosol backscatter coefficient from 12:00 UT on December 16th to 12:00 UT on December 18th. An integration window of 3 hours and 1000 m, shifted in 1-hour and 200 m increments, was employed. During the initial 24 hours, the aerosol layer in the stratosphere exhibited minimal disturbances, but after this period, a band of air with a lower backscatter coefficient formed, ascending from around 8 km to reach approximately 15 km after 48 hours by the end of the measurement. This phenomenon seems to coincide with the transition from positive to negative meridional wind, as suggested by Figure 5.4. In the first 24 hours, lower backscatter coefficients were observed between 5 and 8 km, which dispersed after about 24 hours, leading to an

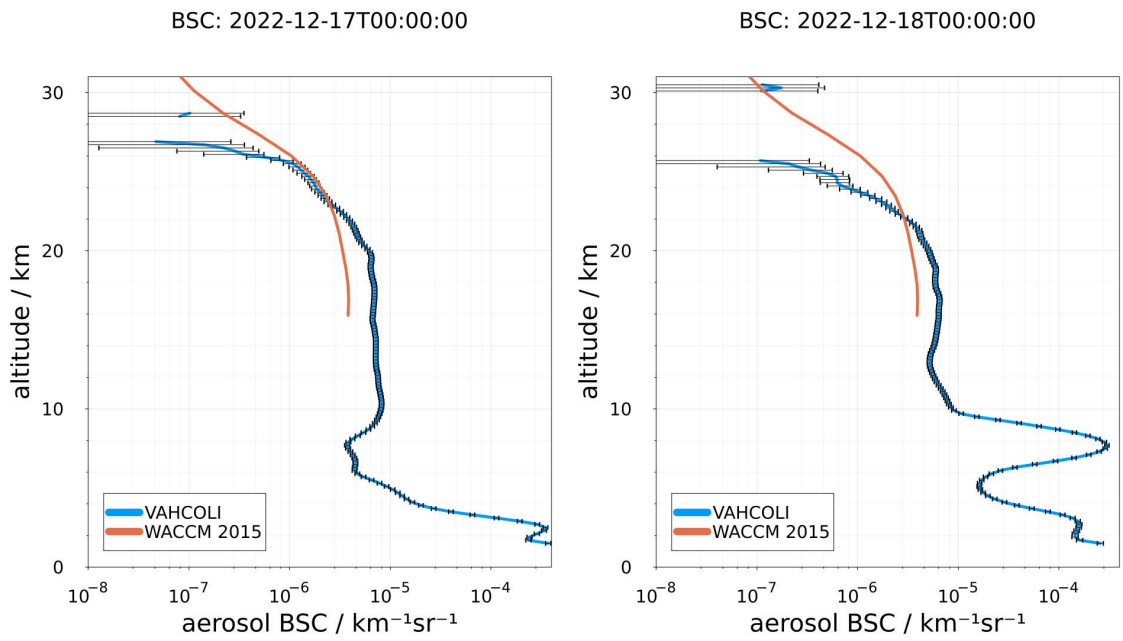

Figure 6.7. Aerosol backscatter coefficient for the nights of 16th-17th December 2022 (left) and 17th-18th December 2022 (right), with an integration time of 12h and a vertical integration window of 1000 m, shifted every 200 m. The second night clearly shows a cirrus cloud around 8 km. The backscatter coefficient remains nearly constant between 10 and 20 km and declines above this range. The orange line represents the October-December mean backscatter coefficient calculated with the WACCM model.

increase in the measured backscatter coefficient by an order of magnitude. After 36 hours, the emergence of a cirrus cloud at roughly 8 km, followed by a second cloud around 10 km, was noted. The orange line marks the highest altitude of the stratospheric aerosol layer with a backscatter coefficient of 1.5×10^{-6} km^{-1}sr^{-1}, illustrating the aerosol layer's height variation throughout the 48-hour measurement period. The maximum altitude for this BSC ranged between 22.3 km and 25.5 km, with an average height of 23.63 km and a standard deviation of 0.74 km.

6.3.2 February 2023 Campaign

In February 2023, a detailed case study on aerosols was conducted, with notable observations captured during the nights of the 7th to 8th and on the 11th. Figure 6.9 illustrates the Mie to Rayleigh backscatter ratio (BSR) for these specific dates, showcasing the distinct atmospheric phenomena encountered. In the first night an integration time of 12 h has been used and the BSR can be interpreted as a nightly mean, while on the 11th an integration time of 30 minutes was used due to the presence of a lot of tropospheric clouds with only short gaps.

The observation from the first night indicates a BSR in the stratosphere akin to those seen in December, featuring a local maximum around 20 km and a shallow slope above. Exceptional signal strength allowed for BSR retrieval up to 30 km without gaps. Below 14 km, the presence of dense cirrus clouds prevented BSR calculation due to the strong

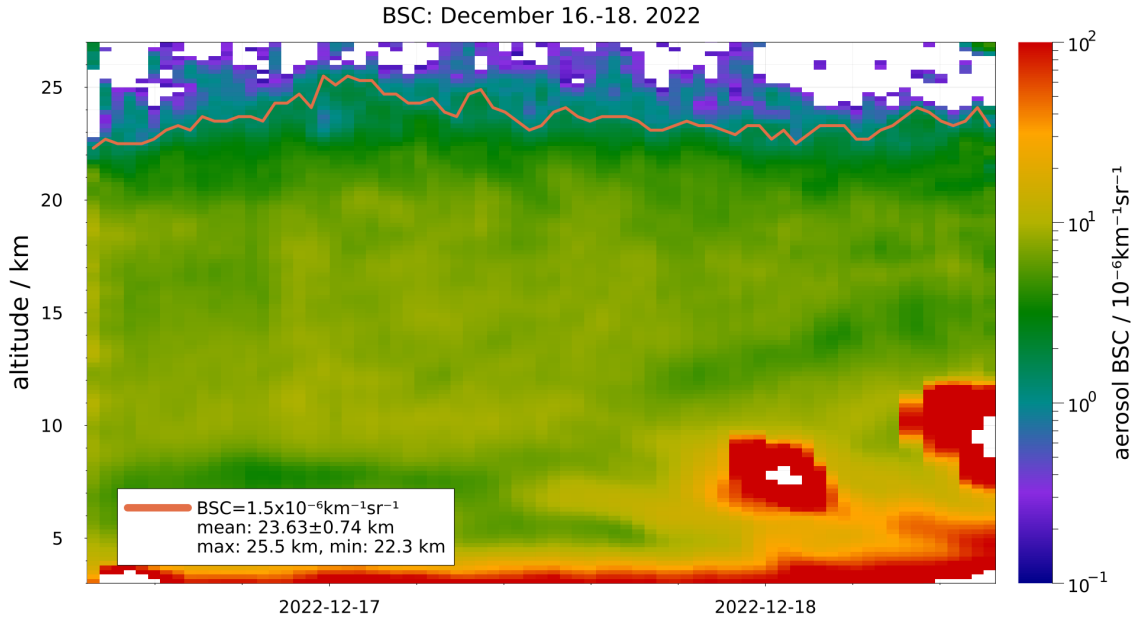

Figure 6.8. Aerosol backscatter coefficient between 12:00 UT on December 16th and 12:00 UT on December 18th, with an integration time of 2 hours and a vertical integration window of 1000 m, adjusted every 40 minutes and 200 m. Cirrus clouds were notably present in the night from the 17th to the 18th of December. The orange line indicates the altitude at which the backscatter coefficient falls to 1.5×10^{-6} km^{-1} sr^{-1}.

signal overloading the APDs. Conversely, the measurement from the 11th of February exhibits a pronounced increase in the local BSR maximum around 21 km, attributable to a polar stratospheric cloud (PSC), with BSR values reaching 2.75. This represents an approximate 6.5-fold increase in the Mie backscatter fraction compared to the previous night's maximum BSR of around 1.27. Beyond 21 km, the BSR declines sharply, and above 24 km, reliable retrieval is hindered by low signal strength due to extensive cirrus and additional cloud cover below 5 km, not depicted in Figure 6.9.

Figure 6.10 presents the computed average aerosol backscatter coefficient (BSC) in the stratosphere for both nights. The comparison with the January-March mean backscatter coefficient from the 2015 WACCM-Karma model shows good agreement, particularly in the slope above 22 km during the first night. The sole vertical measurement configuration, compared to the December data, led to an enhanced signal strength, enabling BSC measurement up to 30 km with the lowest measured value being 2×10^{-8}km^{-1}sr^{-1}. On the evening of the 11th of February, the emergence of the PSC markedly increased the BSC above 20 km, nearly tenfold, peaking at 1.8×10^{-5}km^{-1}sr^{-1} at an altitude of 21 km. The presence of strong cirrus and other tropospheric clouds led to diminished signal strength, as evident from increased measurement errors and gaps in BSC retrieval above 24 km.

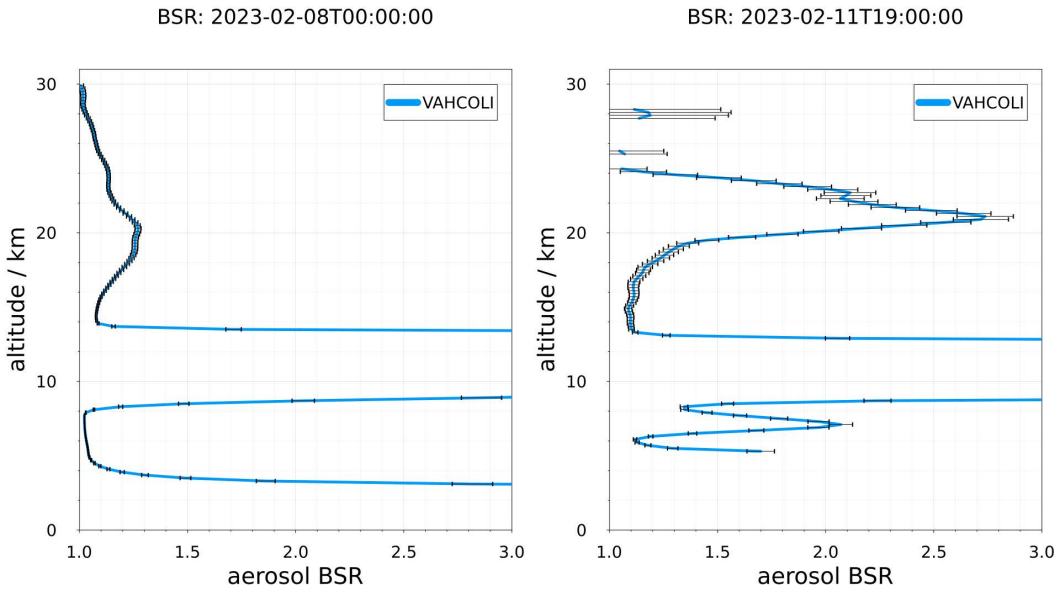

Figure 6.9. Mie to Rayleigh backscatter ratio measured during the night from the 7th to the 8th of February 2023 with an integration time of 12 hours (left) and on the 11th of February with an integration time of 30 minutes (right). A vertical integration window of 1000 m, shifted every 200 m, is used. The measurement on the 11th of February reveals a significantly increased BSR around 21 km due to the presence of a polar stratospheric cloud. Cirrus clouds, visible between 8 and 14 km, are too optically thick for accurate BSR measurement, leading to APD overload.

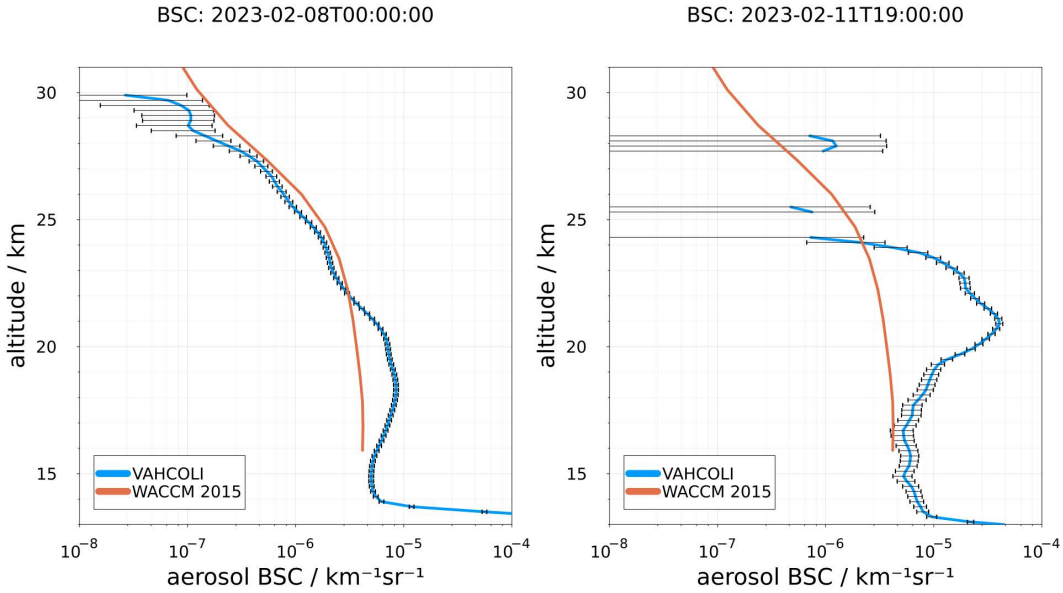

Figure 6.10. Aerosol backscatter coefficient for the nights of 7th-8th February 2023 (left) and on the 11th of February (right), with the same integration as Figure 6.9. The observation on the 11th of February shows a significant increase in BSC above 20 km due to a polar stratospheric cloud. The orange line denotes the January-March mean backscatter coefficient calculated with the 2015 WACCM model.

6.4 Discussion

The findings presented in this chapter demonstrate the VAHCOLI 1 unit's ability to accurately measure aerosol parameters, specifically the Mie to Rayleigh backscatter ratio (BSR) and the Mie backscatter coefficient (BSC). Utilizing a spectral method, this lidar system facilitates BSR measurements using essentially a single wavelength, notably at 770 nm. This approach contrasts with other systems that necessitate backscattering comparisons across multiple wavelengths via an intermediate color ratio step. The BSR measurements reveal atmospheric aerosol features, including tropospheric aerosols observable down to 3 km, cirrus clouds at the tropopause, and stratospheric aerosols within the Junge layer. A distinct peak in the BSR, observed around 20 km, aligns with typical lidar observations of stratospheric aerosols as documented in Langenbach et al. (2019) and Khaykin et al. (2017). This peak, however, is attributed not to an elevated number density of stratospheric aerosols but to the disparate altitude dependencies of Mie and Rayleigh scattering signals. While the Rayleigh scattering signal diminishes with the exponentially decreasing molecular density, aerosol backscattering exhibits a divergent pattern.
This observation becomes particularly evident when examining the aerosol BSC results. The BSR measurements display a pronounced peak at approximately 20 km in the December data, yet this peak is notably absent in the calculated BSC, suggesting a more homogeneous vertical distribution of the Junge layer. Remarkably, the Whole Atmosphere Community Climate Model (WACCM) BSC results show a good correspondence with the lidar-derived BSC measurements, especially in the night from the 7th to 8th February. This concordance is noteworthy, especially considering that the WACCM results represent three-month averages for the year 2015, and aerosols are inherently variable in nature.
The variability of stratospheric aerosols is particularly evident in the heatmaps presented. During the approximately 48-hour measurement period in December, the BSR at an altitude of around 20 km exhibited values ranging from 1.15 to over 1.3, indicating fluctuations in the aerosol load of more than 100%. In terms of the aerosol BSC, the top of the Junge layer—arbitrarily defined at a BSC value of $1.5 \times 10^{-6}\,\mathrm{km}^{-1}\,\mathrm{sr}^{-1}$—varied between 25.5 and 22.3 km during the same measurement period. Over longer durations, even more substantial variations are expected. To capture rapid fluctuations in aerosol load, very short integration times and narrow vertical integration windows are essential. Currently, the system's lack of sufficient signal strength prevents such measurements. This deficiency also constrains the sensitivity for stratospheric aerosols to BSC values exceeding $10^{-7}\,\mathrm{km}^{-1}\,\mathrm{sr}^{-1}$, even with extended integration times. It is important to note, that the system used for the measurements was not optimised for the maximal signal strength and used preliminary optics. It is thus expected that in the future a higher sensitivity can be achieved.
A higher signal strength is also required to measure aerosols in the tilted fields of view. For the placement of the spectral windows, which the method presented in this chapter is based on, it is required to precisely know the frequency at which the peak occurs, together with the width of the Mie-peak. For the vertical pointing field of view, this is relatively easy, since the winds and thus the Doppler-shift is small. The position and the width of the peak can thus be determined in altitudes with good signal strength, with a very high precision, and used to set the windows over the whole altitude range. For the tilted fields of view,

this is not possible, due to the much larger Doppler-shifts introduced by the horizontal winds. A higher signal strength, and thus a more reliable fit, would give the knowledge of the peak position up to higher altitudes and thus enable aerosol measurements in the tilted fields of view.

In addition to the anticipated observations of stratospheric and tropospheric aerosols, a polar stratospheric cloud (PSC) was detected, which is an extremely rare event for this latitude, especially in February. The observation marks the very first lidar measurement of a PSC at Kühlungsborn. The presence of substantial tropospheric and cirrus clouds suggested that atmospheric conditions were suboptimal for lidar observations. Nonetheless, the ability of the system to operate autonomously enabled the observation of the PSC during a brief 30-minute window when cloud coverage was reduced. As noted by Tritscher et al. (2021a), the occurrence frequency of PSC at the location of the IAP is considerably less than 5%. This instance underscores the value of an autonomous lidar network in capturing such infrequent phenomena. Under the prevailing weather conditions, a conventional lidar operator, particularly one focusing on the middle atmosphere, would likely not initiate observations. However, the automated capabilities of the VAHCOLI 1 system facilitated the documentation of this rare event.

The observations and analyses presented in this chapter not only underscore the VAHCOLI 1 unit's capability in autonomously measuring aerosol parameters but also highlight the feasibility of the instrument design and methodology of the analysis. The successful observation of phenomena such as polar stratospheric clouds, under conditions traditionally considered suboptimal for lidar operations, illustrates the unit's potential to significantly contribute to our understanding of atmospheric aerosols, especially when deployed in a network. These observations reinforce the value of autonomous lidar systems in capturing rare atmospheric events, suggesting a direction for future research focused on enhancing observational technologies.

7 | Rayleigh-Temperatures in the Presence of Aerosols

7.1 Temperature Retrieval

For the retrieval of temperatures the signal from elastic Rayleigh-scattering can be used. For this the lidar equation (2.1) can be simplified to

$$P_r(z) = C\frac{\tau(z)n_d(z)}{z^2}\,, \tag{7.1}$$

where C combines all atmosphere and system parameters, $\tau(z)$ is the altitude dependent transmission and $n_d(z)$ is the number density of air molecules. Due to the absence of significant absorption or extinction in the middle atmosphere for the wavelength of 770 nm the transmission is often assumed to be not altitude dependent in the middle atmosphere. Between 10 and 30 km this assumption holds in most cases, but not in the presence of strong aerosol loads. Aerosols are a significant factor to look out for in this altitude range. While above 30 km, the presence of Aerosols can often be neglected in lidar temperature measurements, below they can lead to a significant bias of the calculated temperatures. To handle this problem, traditional RMR-lidars use a Raman channel which detects inelastic rotational or vibrational Raman scattering on nitrogen molecules, which is not affected by aerosols and thus can be used for measurements below 30 km. Due to the smaller scattering cross section of Raman-scattering, the signal strength on the Raman channel is typically reduced by three to four orders of magnitude, which makes this approach only usable on lidars with exceptionally high laser power and large telescopes. On other (shorter) wavelength, ozone absorption also needs to be taken into account.
For VAHCOLI this receiver design is not feasible. Instead for the temperature measurements below 30 km the aerosol influence can be corrected using the backscatter ratios as presented in Chapter 6.1.1. Another challenge for temperature retrievals in the UTLS is presented in the form of the systems overlap function. As presented in Chapter 4.3 the overlap function for the VAHCOLI System is dominated by the defocussing of the Telescopes at lower altitudes. Since the focus point of the telescopes is not precisely known the overlap function can only be determined experimentally. For this, a simplified overlap function in the form of

$$C_{overlap}(z) = 1 - e^{-\frac{z+p_1}{p_2}} \tag{7.2}$$

is assumed. This assumption is a first order correction based on the comparison of the measurements to theoretical Rayleigh profiles and was empirically found to sufficiently

correct the overlap. A better calculation of an overlap function based on equation 7.2 is in principle possible, but was not deemed necessary at this point. Using the Hauchcorne method presented later and a reference pressure profile the two parameters p_1 and p_2 are iterated until the calculated pressure profile is in good agreement with the reference pressure profile. The overlap estimation can remain the same, as long as the system configuration remains unchanged. Similarly the opening of the chopper in the lowest part of the measurement can be corrected.
With the overlap and the aerosol influence corrected, and the constant background of the APD removed, it is assumed that the corrected photon count profile (P_{corr}) is proportional to the air number density.

$$P_r(z) \cdot C_{overlap}(z)^{-1} \cdot z^{-2} - P_{bg} = P_{corr}(z) \propto n_d(z) \tag{7.3}$$

When additionally assuming hydrostatic equilibrium it is possible to derive a temperature profile from the measured Rayleigh backscatter profile. Two different approaches are used for this. The more straight forward density gradient method, also referred to as the hydrostatic integration method (HSI), and the pressure gradient method, which introduces an intermediate step calculating the pressure.

Density gradient method

The pressure differential between a height z_0 and a height z is given by the weight of the column of air between these two heights.

$$\mathrm{d}p = -g \cdot \rho \cdot \mathrm{d}z \tag{7.4}$$

An altitude dependent relation for the temperature $T(z)$ can then be derived by inserting the ideal gas law ($p = nkT$):

$$T(z) = \frac{1}{n(z)} \left(n_0 \cdot T_0 - \frac{g\overline{m}}{k} \int_{z_0}^{z} n(z) \cdot \mathrm{d}z \right) \tag{7.5}$$

with $n_0 = n(z_0)$ and $T_0 = T(z_0)$. T_0 is the so-called seed temperature at the top integration altitude z_0, which is taken as apriory knowledge from an atmospheric model such as ECMWF. Note, that any constant factor of the number density $n(z)$ is reduced in this equation and thus the corrected lidar signal $P_{corr}(z)$, instead of the actual density, can be used. An iterative expression for the temperature can now be derived with z_0 the top of the temperature retrieval and Δz the altitude resolution of the lidar measurement:

$$T(z_i) = \frac{1}{P_{corr}(z_i)} \left(P_{corr}(z_{i+1}) \cdot T(z_{i+1}) - \frac{g\overline{m}}{k} \cdot \Delta z \frac{P_{corr}(z_i) + P_{corr}(z_{i+1})}{2} \right) \tag{7.6}$$

In our temperature retrieval z_0 is chosen in a way, that the ratio between the count rate and the mean background is two at that altitude. The temperature error at each altitude is then given by applying Gaussian error propagation. Here the impact of the seeding on the temperature error $\sigma_T(z)$ diminishes exponentially with altitude, since

$$\sigma_T(z) \propto e^{\frac{z-z_0}{H}} \sigma_T(z_o) \tag{7.7}$$

with H the atmospheric scale height (Khanna et al., 2012; Schöch et al., 2008; Chen et al., 2004).

Pressure gradient method

The pressure gradient method was first presented in Hauchecorne and Chanin (1980) and is thus also referred to as Hauchecorne–Chanin method (HC). It is the standard algorithm of the international Network for the Detection of Atmospheric Composition Change (NDACC) for the retrieval of Rayleigh temperatures (Leblanc et al., 2016). In this algorithm the photon count profile is normalized to the density at a fixed height of a reference density profile and can thus be treated as a density profile $\rho_{lidar}(z)$. For this the density from ECMWF in 30 km at the day of the measurement is utilised. Air pressure ($p(z)$), density ($\rho(z)$) and Temperature ($T(z)$) are related by:

$$p(z) = \frac{R\rho(z)T(z)}{M} \tag{7.8}$$

with R the universal gas constant and M the molecular Mass. Combining Eq. 7.4 and Eq. 7.8 leads to:

$$\frac{\mathrm{d}p(z)}{p(z)} = -\frac{Mg}{RT(z)}\,\mathrm{d}z = \mathrm{d}(\ln(p(z))) \tag{7.9}$$

Using the assumption, that within one height bin of the lidar profile the temperature is constant one arrives at an iterative expression for the generation of a pressure and temperature profile:

$$\frac{p(z_i - \Delta z/2)}{p(z_i + \Delta z/2)} = \exp\left\{\frac{Mg\Delta z}{RT(z_i)}\right\} \tag{7.10}$$

$$X(z_i) = \frac{\rho_{lidar}(z_i)g\Delta z)}{p(z_i + \Delta z/2)} \tag{7.11}$$

$$T(z_i) = \frac{Mg\Delta z}{R\ln(1 + X(z_i))} \tag{7.12}$$

For this routine a seeding pressure for the top layer is required, which is taken from ECMWF-IFS. When iterating downwards the statistical standard errors are then given by:

$$\frac{\sigma_T(z_i)}{T(z_i)} = \frac{\sigma_X(z_i)}{(1 + X(z_i)) \cdot \ln\left(1 + X(z_i)\right)} \tag{7.13}$$

with

$$\left(\frac{\sigma_X(z_i)}{X(z_i)}\right)^2 = \left(\frac{\sigma_\rho(z_i)}{\rho(z_i)}\right)^2 + \left(\frac{\sigma_p(z_i + \Delta z/2)}{p(z_i + \Delta z/2)}\right)^2 \tag{7.14}$$

$$\sigma_p(z_i + \Delta z/2)^2 = (\sigma_p(z_0 + \Delta z/2))^2 + \sum_{j=i+1}^{n} (g\sigma_\rho(z_j)\Delta z)^2 \tag{7.15}$$

Like for the seeding temperature in the density gradient method the contribution of the error of seeding pressure $\sigma_p(z_0 + \Delta z/2)$ on the calculated pressures and temperatures below decreases rapidly. (Hauchecorne and Chanin, 1980; Wing et al., 2018)

7.2 Measurement Campaign Description

For the results presented in this chapter, nightly averaged measurements from the December 2023 campaign, which is described in detail in Section 5.2, and from the February measurements described in Section 6.2, are used.

7.3 Results

The result of the temperature retrieval, as described in section 7.1, can be seen in figure 7.1. The left panel shows the corrected and scaled Rayleigh signal measured in the night from the 16th Dec 18:00UT until the 17th Dec 6:00UT, together with the density profile from ECMWF. Until an altitude of roughly 6 km the lines are almost superimposed, thanks to the correction of overlap and aerosols. Below the Rayleigh signal starts to diverge from the ECMWF density, due to the full closure of the chopper. The center panel shows the assumed functions for the overlap and the closing chopper, which are used for the correction, together with the ratio of the calculated pressure from the Hauchecorne-Chanin method and the ECMWF pressure. The pressure ratio is close to one in all altitudes above 6 km, which indicated a good correction, especially of the overlap function. For the overlap parameters p_1 and p_2 as defined in equation 7.2 values of 15 km and 10 km were chosen for this measurement. The right panel shows the calculated temperatures from the Hauchecorne-Chanin method and the direct hydrostatic integration together with the respective statistical error estimates and the ECMWF temperature. The temperatures using the combination of the Hauchecorne-Chanin method and the ECMWF densities are plotted as an additional reference here (later referred to as HC reference). The temperature retrieval starts at a seeding altitude of 47.5 km. In this case both integration methods result in almost indistinguishable temperature profiles, with the biggest differences showing in the different handling of the statistical error. The density gradient method is seeded with a temperature of 255 K and the pressure seeding of the Hauchecorne-Chanin method equates to a temperature of 262 K. With decreasing altitude the temperature also decreases, following the HC reference. The lowest temperature of approximately 200 K is reported around 28 km altitude, which is five degrees higher than the ECMWF temperature, but two degrees colder than the HC reference. Below 28km the temperatures from both methods exhibit a wavy pattern, oscillating between the ECMWF temperatures and the HC reference, until an altitude of approximately 17 km is reached. In lower altitudes the calculated temperatures follow ECMWF temperatures and the HC reference. A larger deviation from the ECMWF temperatures is visible below 8 km until the chopper closes in an altitude of 6 km disturbs the measurement. The start of the aerosol correction below 28 km is visible as an increase in the statistical error, caused by the statistical uncertainty with which the backscatter ratio is determined and the propagation in quadrature of it.
The importance of the aerosol correction is highlighted in figure 7.2. Here, the results of the temperature retrievals with different levels of aerosol correction are shown. With a partial correction of the aerosols, the calculated temperatures change drastically below 28 km. The lowest temperature is now calculated in an altitude of 22 km, 2 km above the peak in the BSR as shown in figure 6.5. The calculated temperatures are 15 K lower

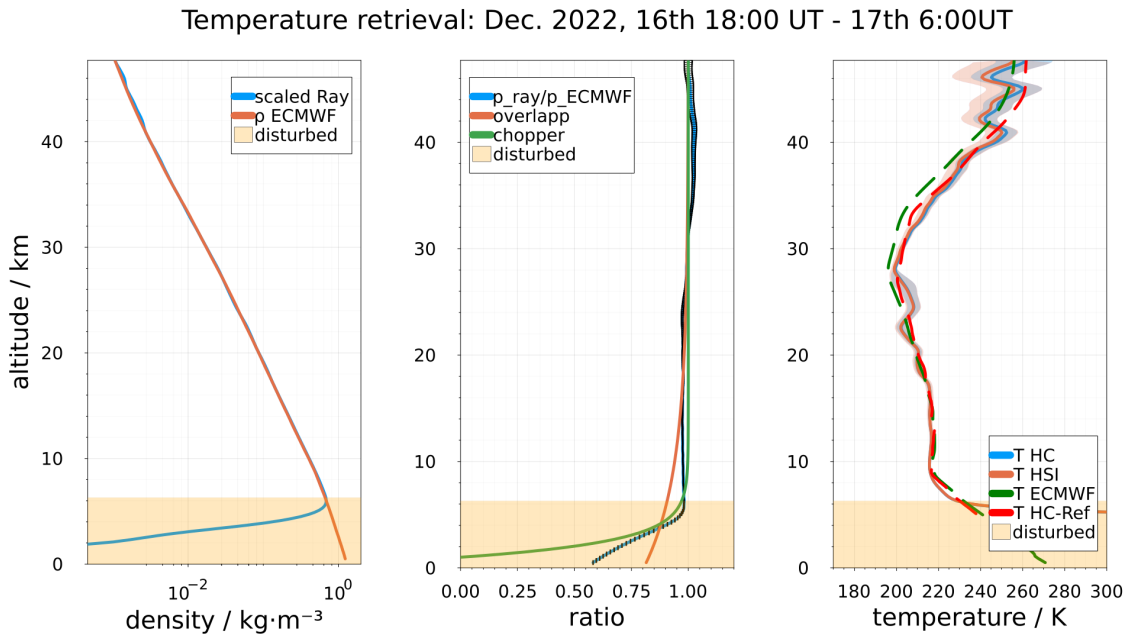

Figure 7.1. Retrieval of the nightly average temperature on the night from the 16th to 17th December 2022. **left:** The measured Rayleigh profile (blue) scaled to the ECMWF density profile (orange), with all corrections applied. Below 5km the Rayleigh signal suddenly drops, due to chopper closing. This altitude is marked in all plots with a transparent orange box, to indicate the disturbance of the temperature measurement. **center:** Ratios used for the correction of overlap (orange) and chopper curve (green), together with the ratio of the resulting pressure profile from the Hauchecorne-Chanin method to ECMWF pressure (blue). **right:** Temperature results from the Hauchecorne-Chanin method (blue) and the simple hydrostatic integration (orange) together with the ECMWF temperature (green, dashed) and the resulting temperature when applying the HC method to the ECMWF density (red, dashed).

than the reported ECMWF temperature for 50 % aerosol correction case and 30 K lower in case of no aerosol correction. Below 22 km, calculated and reference temperatures start converging, but at 17 km the calculated temperatures overshoot and the cold bias turns into a warm bias. Around 10 km altitude, the calculated temperatures are 10-15 K above the ECMWF temperatures when no aerosol correction is applied.

Figure 7.3 shows additional measurements of nightly average temperatures for the nights from the 17th to 18th December 2022, 7th to 8th February 2023 and 14th to 15th February 2023. The night from the 17th to 18th December shows a temperature structure similar to the previous night, shown in figure 7.1, with a temperature minimum around 27 km. The seeding approaches of both methods lead to similar temperature at the seeding altitude. Small remaining differences between the methods quickly vanish below the seeding altitude of 47 km. The wavy pattern visible in the night before below the temperature minimum is less pronounced, but still visible during this night. The night from the 7th to 8th February was done with only the vertically pointing telescope, resulting in a better signal compared to the measurements with the 5 fields of view in December, since the laser power is not distributed over the different fields of view, resulting in a high seeding altitude of almost 51 km. The temperatures calculated from this measurement exhibit a

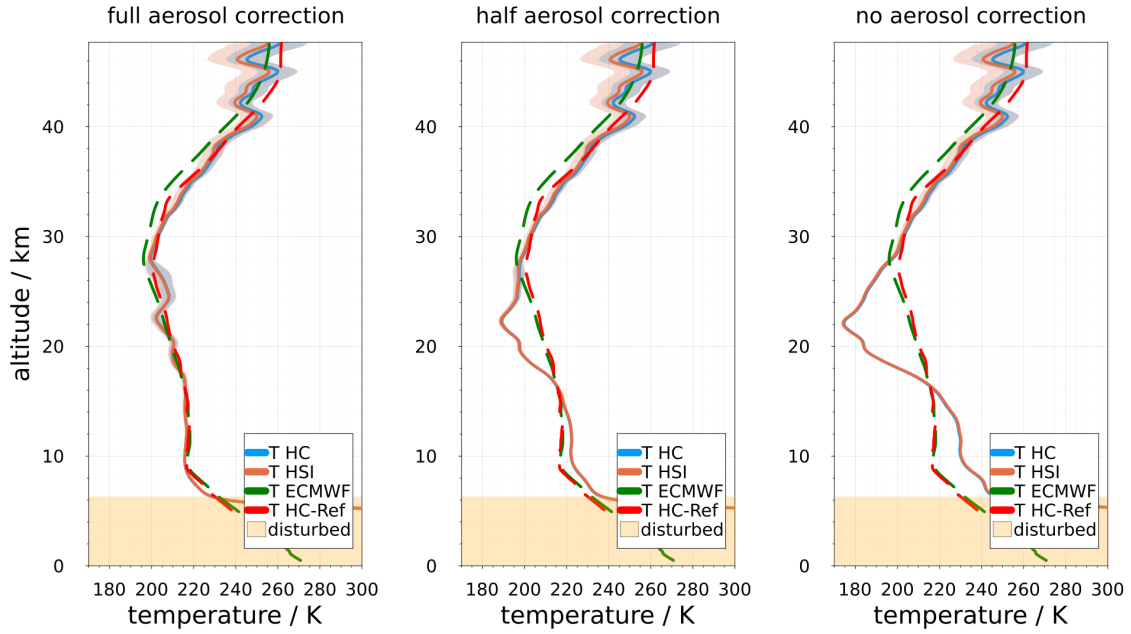

Figure 7.2. Comparison of the temperature results for the night from the 16th to 17th December 2022 when using different strength of aerosol correction. Results of the Hauchecorne-Chanin method (blue) and the hydrostatic integration method (orange) are shown together with the ECMWF temperatures (green, dashed) and the resulting temperature when applying the HC method to the ECMWF density (red, dashed) for reference. **left:** Aerosols fully corrected. **center:** Only half of the aerosols corrected. **right:** Aerosols not corrected.

significant difference from the ECMWF temperature and the HC reference temperature of 15 K and 7.5 K respectively in an altitude of 30 km. The temperature minimum extends from around 20 km to below 18 km with a temperature of 205 K. Below 14 km the measurement is disturbed by strong cirrus clouds.

A temperature calculated one week later for the night from the 14th to 15th February shows less deviation from the HC-reference, which it follows from 36 km to approximately 24 km. Between 36 km and the seeding altitude of close to 52 km, significant deviations from the references are visible. At 23 km and 20 km, two temperature dips as low as 187 K are visible in the calculated temperatures, which coincide with the two peaks of the polar stratospheric cloud observed on the 11th of February (see figure 6.9 and 6.10). Below these dips, the calculated temperature is in good agreement with the ECMWF temperature, until at 11 km the chopper disturbs the temperature measurement. Similarly to the measurement presented in the center column, the system measured only in the vertical field of view resulting in a higher seeding altitude of approximately 46 km.

All three measurements presented in figure 7.3 show differences between the Hauchecorne-Chanin method and the hydrostatic integration method as a result of the different seeding methods. Below the seeding altitude, the two methods converge until the difference between them becomes negligible, typically below 30 km when seeding altitudes between 40 and 46 km are used.

For the four nights previously discussed, measurements from IAP's RMR-lidar are available for comparison, as shown in Figure 7.4. For the December measurements, continuous

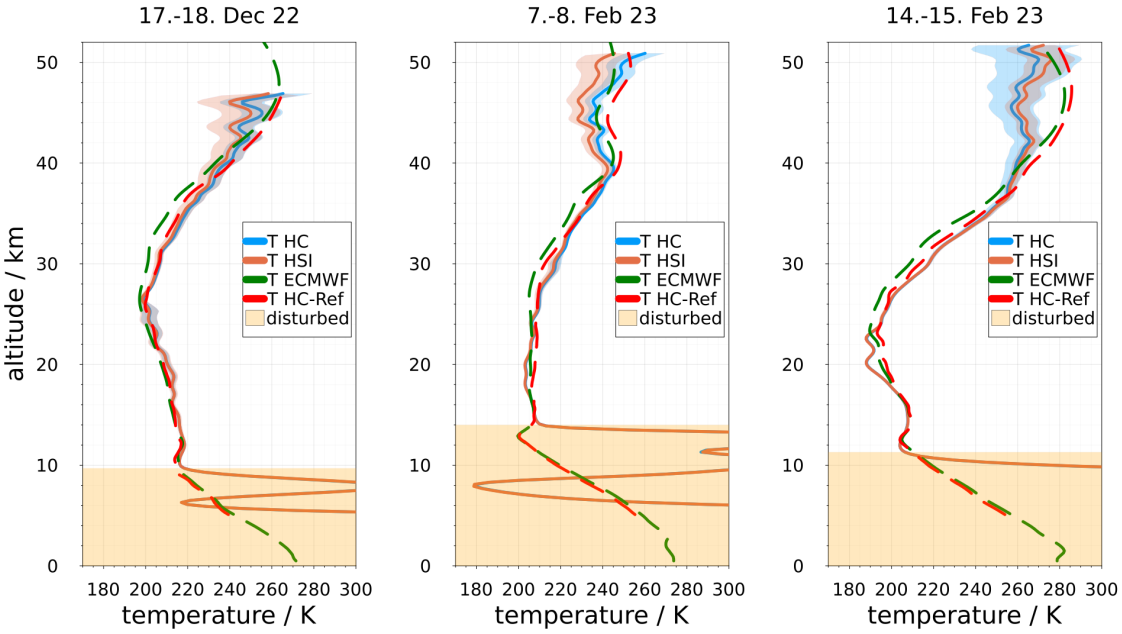

Figure 7.3. Comparison of the temperature results for three additional nights of continuous measurements between 17:00UT and 5:00UT, with an integration time of 12h and a vertical integration window of 1000 m shifted in 200 m steps. For each night the results of the Hauchecorne-Chanin method (blue) and the hydrostatic integration method (orange) are shown together with the ECMWF temperatures (green) and the resulting temperature when applying the HC method to the ECMWF density (red) for reference. **left:** Nightly average for the night from the 17th to 18th December 2022, during which the system measured along 5 fields of view. **center:** Nightly average for the night from the 7th to 8th February 2023. Here only the system measured only along the vertical field of view, three days prior to the observed PSC. **right:** Nightly average for the night from the 14th to 15th February 2023. Here the system measured only along the vertical field of view, three days after the observed PSC.

coverage throughout the nights is not available; hence, the RMR profile closest to midnight is selected for comparison. The December measurements utilize the RMR-lidar's Raman channels, enabling measurements below 25 km and in the presence of aerosols. In both December nights, temperatures measured with the RMR-lidar align well with those measured by VAHCOLI. The undulating feature observed in the VAHCOLI temperatures around 25 km during the first December night is similarly present in the RMR measurements, though with a slightly altered configuration.

In the second December night, discrepancies between the RMR temperatures and our temperature retrievals are apparent in altitudes between 30 and 40 km, exceeding σ but remaining within 3σ. The most significant differences are observed just below the seeding altitudes. For the February nights, RMR-lidar measurements are limited to altitudes above 25 km due to issues with the Raman channels. In the first February night, the RMR measurements correlate closely with the VAHCOLI 1 temperatures, particularly between 25 and 40 km. Above 40 km, larger deviations are noted up to the seeding altitude. A slight discrepancy is noted around 30 km, where the VAHCOLI system accounted for a detected aerosol layer.

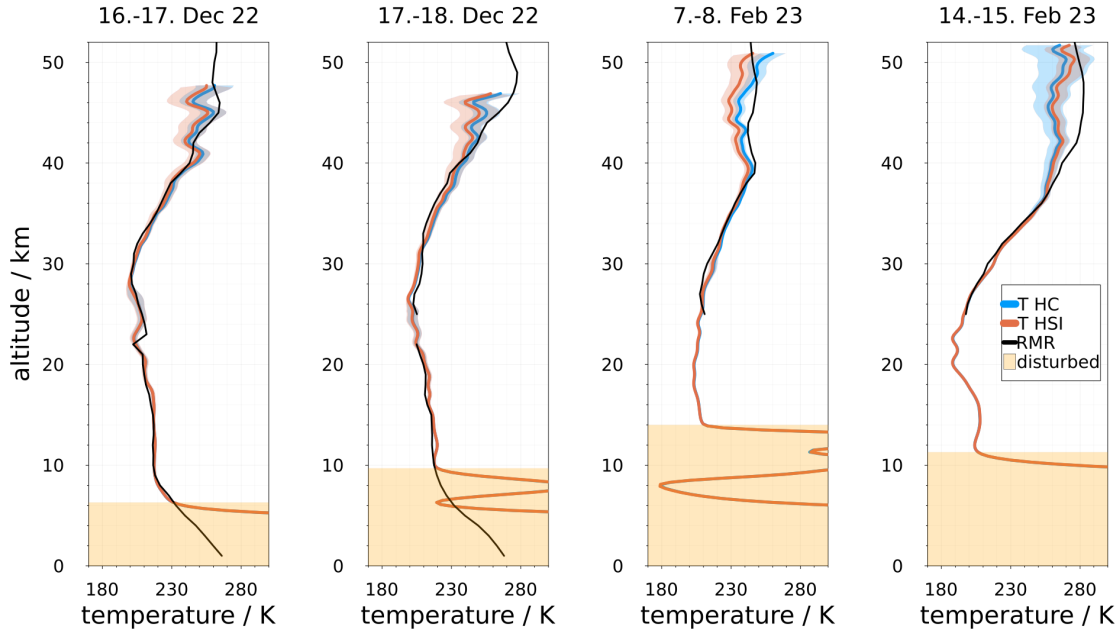

Figure 7.4. Comparison of the temperature results for the four nights to measurements of the RMR2 lidar in Kühlungsborn (black). For VAHCOLI 1 an integration time of 12h and a vertical integration window of 1000 m shifted in 200 m steps is used. The temperatures of the RMR lidar are sampled with an altitude resolution of 1 km and use an integration time of 120 minutes, if available the nightly average is used. **left:** Nightly average for the night from the 16th to 17th December 2022 for VAHCOLI 1 compared to the temperature measured with the RMR system at 19:30 UT ±60 min. **center-left:** Nightly average for the night from the 17th to 18th December 2022 for VAHCOLI 1 compared to the temperature measured with the RMR system at 19:45 UT ±60 min. **center-right:** Nightly averages for the night from the 7th to 8th February 2023. **right:** Nightly averages for the night from the 14th to 15th February 2023. For the nights in February the Raman-channel of the RMR lidar was inoperable and thus no measurements are available below 25 km.

A similar discrepancy around 30 km is also observed on the second February night, albeit less pronounced. Aside from this, the VAHCOLI temperatures and the RMR temperatures are in close agreement up to 36 km. Above this, deviations of several tenths of a Kelvin are observed up to the seeding altitude of the VAHCOLI lidar indicating a problem, with the removal of the non-linear background.

While the signal strength is highest in the vertical field of view, the tilted telescopes can also be used to calculate temperatures. Since no good quality aerosol measurements are possible along the oblique fields of view as discussed in chapter 6, one must assume homogeneity and use the aerosol measurements from the vertical field of view for the aerosol correction. The resulting temperatures for the night from the 16th to 17th December 2022 are shown in figure 7.5. Due to the reduced signal strength from the tilted telescopes compared to the vertical pointing FOV, the seeding altitude is also significantly decreased to ∼ 35 km in the north FOV and ∼36 km in the south FOV. In general, the temperature profiles measured in the tilted fields of view are comparable to the temperature profile from the vertical field of view. After an altitude range with stronger temperature oscillations from

the seeding altitude to ∼10 km below, the tilted temperature profiles exhibit the same features visible in the vertical temperature profile. A small systematic temperature shift between the individual fields of view was observed, most likely caused by uncertainties of the overlap correction for the different telescopes.

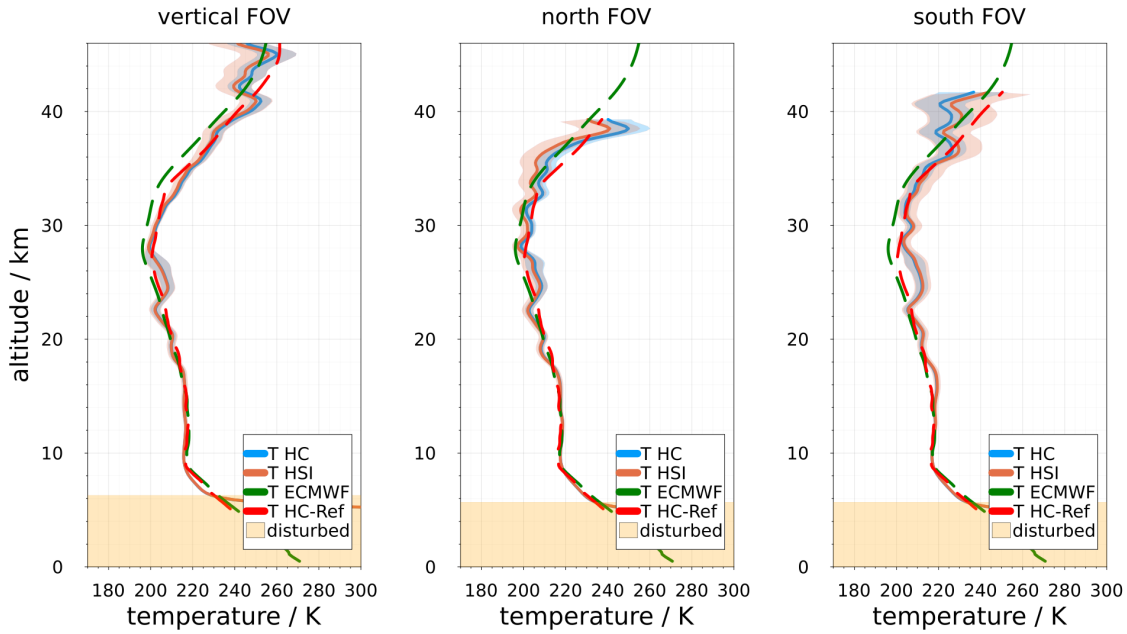

Figure 7.5. Comparison of the nightly average temperature in the night of the results for three different fields of view, with an integration time of 12h and a vertical integration window of 1000 m shifted in 200 m steps. For each field of view the results of the Hauchecorne-Chanin method (blue) and the hydrostatic integration method (orange) are shown together with the ECMWF temperatures (green) and the resulting temperature when applying the HC method to the ECMWF density (red) for reference. **left:** Temperature profile calculated from the vertical pointing 50 cm telescope. **center:** Temperature profile calculated from the 25 cm telescope tilted 30 degree of zenith towards north. **right:** Temperature profile calculated from the 25 cm telescope tilted 30 degree of zenith towards south.

7.4 Discussion

The temperature results presented in the previous section underscore the VAHCOLI instrument's ability to measure temperatures within the stratosphere and troposphere effectively. The process of retrieving temperatures is reliable, showing that the lidar temperatures are in acceptable agreement with those reported by ECMWF. The aerosol correction, utilizing the Mie to Rayleigh backscatter ratio as outlined in the preceding chapter, proves adequate for determining lower stratospheric and tropospheric temperatures. This assertion is supported by a comparison with Raman-temperatures from IAP's RMR lidar, which highlights undulating features absent in ECMWF temperature profiles.
Particularly under the favourable conditions observed in February 2023, VAHCOLI's enhanced sensitivity to aerosols enables accurate correction for aerosol influences on tem-

peratures, even at altitudes typically considered free of aerosols. The discrepancy between VAHCOLI and RMR temperatures around 30 km serves as a prime example, suggesting that VAHCOLI may correct for a possible aerosol layer not accounted for by the RMR lidar.
The derived temperatures from the tilted telescopes further demonstrate the MultiFOV design's strength in providing 3D atmospheric parameter measurements with a single instrument. Assuming aerosol concentration homogeneity is effective over a 12-hour integration period. For significantly shorter integration periods, however, a method for independent aerosol detection in the tilted fields of view is necessary and possible with better signal strength, as discussed in Section 6.4.
The current limitation in signal strength restricts the system's application for high-resolution studies of gravity waves in the middle atmosphere over short integration times. Yet, the ability to measure temperatures reliably up to 40 km, and with potential up to 50 km, showcases the system's overall capability for middle atmospheric temperature measurements. Enhancing laser power and detection efficiency could facilitate higher time resolution.

8 Discussion

8.1 Interpretation of the Results

The focus of this thesis was the development of a method, which allows three-dimensional coverage with a single lidar. With the design of the MultiFOV upgrade for the VAHCOLI instruments, this goal was successfully achieved. The measurements of wind and temperature in multiple fields of view presented in Section 5.3 and 7.3 highlight this. Especially the described observations of a meridional wind gradient found when comparing the measurements of meridional wind in the north and south field of view, demonstrate the utility of employing five fields of view with such an instrument.
In general, the horizontal wind measurements performed with the MultiFOV upgrade are very promising, with the winds of ECMWF and Aeolus in good alignment with the observations. The discrepancy between lidar and ECMWF vertical wind shows the benefit of lidar observations. The vertical winds measured with VAHCOLI show unprecedented accuracy, thanks to the spectral measurement method. These precise measurements of vertical winds are valuable on their own, as they allow for more precise gravity wave studies, since no background wind has to be considered, as well as give an insight into vertical coupling and mixing of the atmosphere.
Albeit limited to vertical measurements by the current status of the data processing and system performance, the measurements of the aerosol load in the atmosphere in form of the aerosol backscatter ratio and backscatter coefficient provide a valuable insight. The structure of the Junge layer reported in Section 6.3 is well in line with the structure typically reported by other backscatter ratio studies, and the WACCM-CARMA backscatter coefficients compared well to the measured backscatter coefficients. The, to our knowledge, first lidar observation of a Polar stratospheric cloud in Kühlungsborn is a great achievement and highlights the unique qualities of the VAHCOLI instruments, when it comes to aerosol sensitivity and autonomous operation.
This sensitivity for aerosol allows the measurement of temperatures in the troposphere and stratosphere even under relatively significant aerosol loads, without the need for additional Raman-channels. Only strong aerosol loads in the form of thick cirrus clouds can be a problem, since they overload the detector. The temperatures calculated along the tilted field of view are in good agreement with the vertically measured temperatures, as it is expected for the long integration time of 12 hours. Differences in the temperature between the individual fields of view, as they would be caused by the propagation of gravity waves through the fields of view, are only expected when higher temporal resolutions are available with higher signal strength.

The measurements of wind, aerosols, and temperatures mark completely new methods, only possible in the presented form due to the novel, spectral measurement technique applied in the VAHCOLI instruments. Since the measurement technique is unique, large parts of the data processing methods had to be developed from scratch. The demonstrated results from the new methods and the comparison of select cases to ECMWF, WACCM-CARMA, Aeolus and RMR-lidar data, indicate that our goal, to establish a robust data processing pipeline, was successful.
Overall, the reliability of the instrument between the initial measurement campaign and June 2023 was good, with more than 600 hours of measurements. Of these measurements 85 hours were done in MultiFOV mode, due to the higher complexity of setting the system up for multi field of view measurements and the experimental nature of the MultiFOV upgrade. Based on presented results and the measurements of the signal strength during the operation in MultiFOV mode, the calculations which presented in Chapter 4 for the design of the lens telescopes were confirmed. The telescopes performed in the lidar system as expected from the calculations and the laboratory measurements, and can thus be used without any restrictions in future systems.

8.2 Limitations and Future Improvements

The biggest limiting factors for the systems performance is its low signal strength. One of the highest signal measurements done in February 2023 showed count rates on APD2 of only ∼1.4% of the value used in Lübken and Höffner (2021) for the theoretical evaluation of the estimated performance. The laser used in the VAHCOLI 1 unit generates pulse energies of less than 3 mJ instead of the 6 mJ assumed for the calculations in the publication, and thus the overall detection efficiency of the system can be estimated to be on the order of 0.5 to 1%. While this is already an improvement compared to the VAHCOLI 0 prototype, the changes to the telescopes' temperature management and the optimisation of the vertical mirror telescope, did not provide the anticipated improvements, probably due to still unidentified optical issues in the detection bench. An improvement of the systems' detection efficiency to 10% or more, as reported for the IAP's mobile potassium lidar is realistic and even values of 30% detection efficiency, as used for the theoretical calculation of the estimated performance in Lübken and Höffner (2021), are feasible. Thus, an improvement of the signal strength by a factor of 10 to 30 in the future can be achieved with careful optimisation of the detection bench, which will lead to a significant improvement of vertical and temporal resolution and a better altitude coverage. Since the laser used in VAHCOLI 1 was the very first laser of its kind, it still has margins left in regards to is tuning. In the future, tuning the laser and increasing its repetition rate to 750 Hz, as done for the laser in VAHCOLI 2, will roughly double the laser power, without any hardware changes. When combining this laser update with the optimisation of the currently still preliminary design of the detection bench, an increase in signal strength by a factor of 20 to 60 seems feasible.
The instrument's low signal strength is also connected to the confinement of the measurement of aerosol BSR and BSC to the vertical pointing field of view. This limitation stems from the retrieval method for these parameters, as outlined in Chapter 6, which ne-

cessitates knowledge of wind-induced Doppler shifts and Doppler broadening from wind fluctuations. In tilted beams, these effects are significantly exacerbated by larger horizontal winds, necessitating the use of a Voigt function fit to the observed spectrum—a method viable only at altitudes with adequate signal strength. For future temperature studies leveraging tilted fields of view, a revised method for aerosol BSR retrieval is necessary to accurately correct for aerosols in tilted fields of view, when higher time resolutions are used and thus aerosol homogeneity across the fields of view can not be assumed.
A key limiting factor for the usage of multiple fields of view during measurement is the long time stability of the multi field of view upgrade. While the upgrade does hold its alignment when mounted to the side of the VAHCOLI core unit over the course of weeks, allowing for long, autonomous observations, some realignment is still required every month or too, which makes the current design not stable enough for long term autonomous operation, as it is required for a network instrument. For future implementations of the MultiFOV technique this stability needs to be improved, by either strengthening the MultiFOV housing or incorporate the multi field of view approach into the design from the beginning on, as it is done for the instruments in the follow up projects EULIAA and LidarCUBE. These projects rely on the lens telescope design developed for this work and will further improve their performance, by swapping the uncoated optics with coated versions and using custom lenses.

8.3 Comparison with Existing Lidar Systems

VAHCOLI instruments, alongside the data analysis methods developed throughout this thesis, establish a universal platform for measuring a variety of atmospheric parameters with a relatively simple and compact optical setup. This marks a significant departure from traditional DWL systems, which are generally larger and more narrowly focused on wind observation alone. For instance, systems utilizing the double edge technique, such as OHP and OPAR, are not capable of simultaneously measuring temperature and wind due to limitations highlighted by Khaykin et al. (2020). Conversely, systems using the DORIS technique, such as ALOMAR, can measure both wind and temperature simultaneously, but are very sensitive to aerosol interference (Baumgarten, 2010). This leads to the need for extensive corrections in the presence of aerosols.
In contrast, the VAHCOLI system can simultaneously measure wind, temperature, and aerosols without the accuracy of wind and temperature measurements being compromised by aerosol backscatter—in fact, the presence of aerosols enhances the system's wind detection capabilities.
Traditional DWL lidars still hold advantages in terms of temporal resolution and the extent of altitude coverage—with wind measurements in this thesis extending up to 25 km and temperature readings averaged nightly up to 50 km. However, anticipated improvements in signal strength are expected to extend both the temporal resolution and altitude reach of our measurements. Furthermore, the incorporation of Doppler-Rayleigh and Doppler-resonance measurements, which require no hardware modifications to the system, will potentially expand the altitude coverage beyond that of all currently operational DWL systems.

9 | Conclusion

The objective of this thesis was to advance the VAHCOLI instruments, with a particular focus on the accurate measurement of three-dimensional wind patterns. This was done with the intention of enhancing our understanding of atmospheric dynamics. The development and implementation of the MultiFOV upgrade have proven instrumental in achieving this goal, offering a new perspective on atmospheric observation.

9.1 Achievement of Research Objectives

1. **Three-Dimensional Atmospheric Coverage:** The successful development of a methodology allowing for partial three-dimensional atmospheric coverage using a single lidar system marks a significant milestone. The MultiFOV upgrade has shown its efficacy in measuring wind and temperature across multiple fields of view, addressing the objective of observing horizontal scales crucial for studying atmospheric phenomena.

2. **Observation of Horizontal Scales:** Significant progress has been made in the coverage of horizontal scales, extending from the microscale to the mesoscale. This is an essential aspect for the observation of gravity waves and stratified turbulence. The meridional wind gradient analysis underscores the system's capability in capturing atmospheric dynamics across these scales.

3. **System's Network Application and Cost Efficiency:** The design of the MultiFOV upgrade, focusing on the system's network application and cost efficiency, enables a comprehensive collection of atmospheric data, aligning with the goal of extensive atmospheric monitoring. The upgrade itself was realised in a cost effective manner, drastically increasing the measurement capabilities of an individual instrument, with only a slight increase in cost.

4. **Robust Data Processing Pipeline:** A robust data processing pipeline has been developed to convert the spectral raw data into data products usable for atmospheric studies. This includes winds up to 25 km, aerosol backscatter ratio and backscatter coefficient up to $\sim$30 km and temperatures below 50 km.

Additional Achievements

While the main aim of the work done for this thesis was the measurement of three-dimensional winds, in the process of achieving this goal additional atmospheric parameters, such as aerosol backscatter ratio and coefficient and temperature, were measured. The analysis of these parameters is beyond the initially set goal, but highlights the capability of the upgraded system. Thanks to the combination of the autonomous observation capabilities and the aerosol sensitivity of the instrument, a polar stratospheric cloud over Kühlungsborn was measured. An event which is highly unlikely to capture with a lidar.
The capability to measure temperatures also goes beyond the initially set goals for the project and has the additional benefit of validating the measured aerosol parameters, since without the correct measurement of the aerosol BSR, the measured temperatures would deviate significantly from the temperature profiles reported by ECMWF and the IAPs RMR-lidar.
These additional achievements highlight the general concept of the VAHCOLI instruments to be universal lidars. As they cover a wide altitude range, have (now) multiple fields of view and are able to do measurements of Mie-, Rayleigh- and resonance-scattering, they are able to provide diverse measurements of atmospheric parameters, by using completely new methods for measurements and data analysis.

9.2 Future Directions

The primary challenge facing the system is its low signal strength, limiting aerosol parameter measurements and affecting resolution. Future improvements aim at optimising the detection bench to enhance signal strength significantly, a crucial step for high-resolution atmospheric studies. Also the alexandrite laser used for the measurements, which are presented in this thesis, was the first of it's kind and not fully optimised. It is expected that the usage of a new laser with higher average power, operating at 750 Hz will further increase the signal strength.
The measurement techniques presented in this thesis will find broad usage in the future, especially in the follow up projects to VAHCOLI and more in-depth atmospheric studies.

Follow up projects

Two follow up projects have started, which are partly based on the technologies presented in this thesis.
The first one is **EULIAA** which stands for European Lidar Array for Atmospheric Climate Monitoring. This EU-funded project aims to develop a lidar array measuring autonomously and continously the atmospheric wind and temperature from 5 km to 50 km. The lidar units developed for this project leverage the multi field of view techniques presented in this thesis, first using three fields of view with an option to use five. The instruments will use a novel, frequency doubled version of the alexandrite ring laser operating at 386 nm in a deep Fraunhofer line, for better daylight coverage. A next generation UV-laser based on alexandrite with the necessary parameters has been demonstrated by Scheuer et al. (2024).

The second project is **LidarCUBE**, which is funded by Germanys Federal Ministry of Education and Research. In this project the technology transfer to a consortium of research institutes and small and medium-sized enterprises is prepared, with the ultimate goal to foster production capabilities for middle atmosphere universal wind lidars in the industry. The instruments developed in this project are bases on a simplified and optimised design derived from the VAHCOLI instruments.
Both of the projects will make use of an updated design of the lens telescope, which were developed for this thesis, as can be seen in Figure 9.1. These will leverage the higher quantities of required optics in the project, to replace the uncoated lenses in the telescope design with custom coated lenses and thus increase the performance of the lens telescopes further.

Figure 9.1. CAD renderings of the instruments developed in the follow up projects. **left:** CAD drawing of the preliminary instrument design for the EULIAA project. **center & right:** CAD drawings of the preliminary instrument design for the LidarCUBE project (LiCuSpace, 2024).

Future atmospheric studies

Future atmospheric studies will include prolonged studies or campaigns for the validation of the instruments' measurement capabilities. These studies will either be done with the instruments build for and discussed in this thesis or at latest as part of the EULIAA project. The multi field of view techniques presented in this thesis can not only be applied to measurements of temperature and wind, but also to other atmospheric parameters such as aerosol and metal densities. With sufficiently increased signal strength, the comparison of aerosol measurements in multiple fields of view can increase our knowledge of the aerosol distribution and homogeneity in the stratosphere. Similarly, studies of the homogeneity of the mesospheric metal layers are possible with the multi field of view approach. Figure 9.2 shows preliminary results for potassium densities measured during the December 2022 campaign in three different fields of view, highlighting, the capability to observe resonance scattering even with the smaller lens telescopes. Future systems with higher

signal strength will thus also be able to do temperature and wind measurements in the mesosphere.

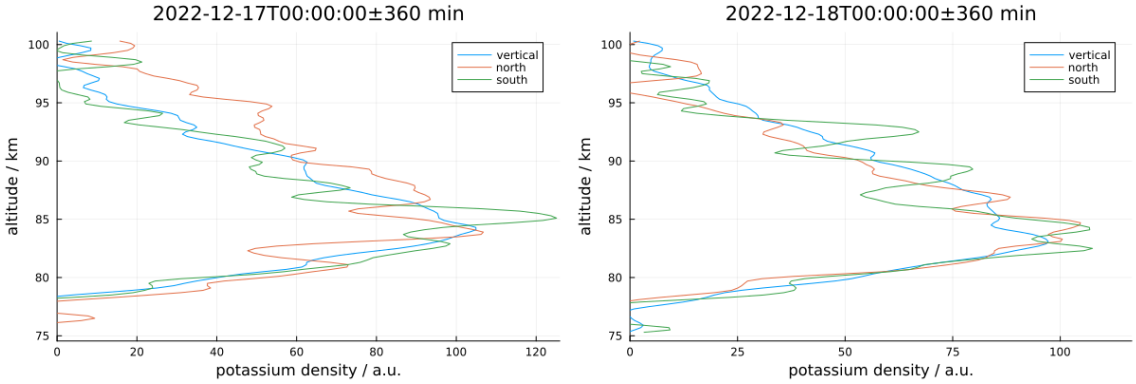

Figure 9.2. Preliminary measurements of potassium densities done in December 2022. An integration time of 12h and a vertical integration window of 1000 m shifted in 200 m steps was used **left:** Nightly average for the night from the 16th to 17th December 2022. **right:** Nightly average for the night from the 17th to 18th December 2022.

With unique sensitivity for aerosols of the VAHCOLI instruments, future measurement campaigns will contribute to the O-MSP-Li project, which focuses on observations of meteor smoke particles in the middle atmosphere with lidar.
In conjunction with the observations for O-MSP-Li, a comprehensive investigation into vertical winds is planned. High-resolution vertical winds will be analysed together with the Doppler broadening of the Mie spectrum. The objective is to utilise the Doppler broadening measurement provided by the instrument to quantify turbulence in the atmosphere.

A | Autocollimation setup

As discussed in 4.3, the optical quality of the telescopes represents a significant factor in the performance of a lidar system. Consequently, an autocollimation setup was employed to assess the optical quality of the telescopes designed and constructed for the multi-field of view upgrade. A schematic and an image of this setup can be found in Figures A.1 and A.2, respectively. The camera in the setup is employed to rapidly assess the optical quality of the telescope and identify the focus point of the telescope. The combination of a pinhole in front of a photo diode is utilized to more accurately gauge the telescope's impact on system efficiency. The time resolved signal of the photo diode can also be utilized to assess the effect of turbulence on signal strength in a laboratory setting. Following assembly, each lens telescope is focused and tested using the image on the camera. This ensures the performance of the lidar and significantly reduces the time required to identify the optimal focus point for lidar measurements when conducting atmospheric measurements.

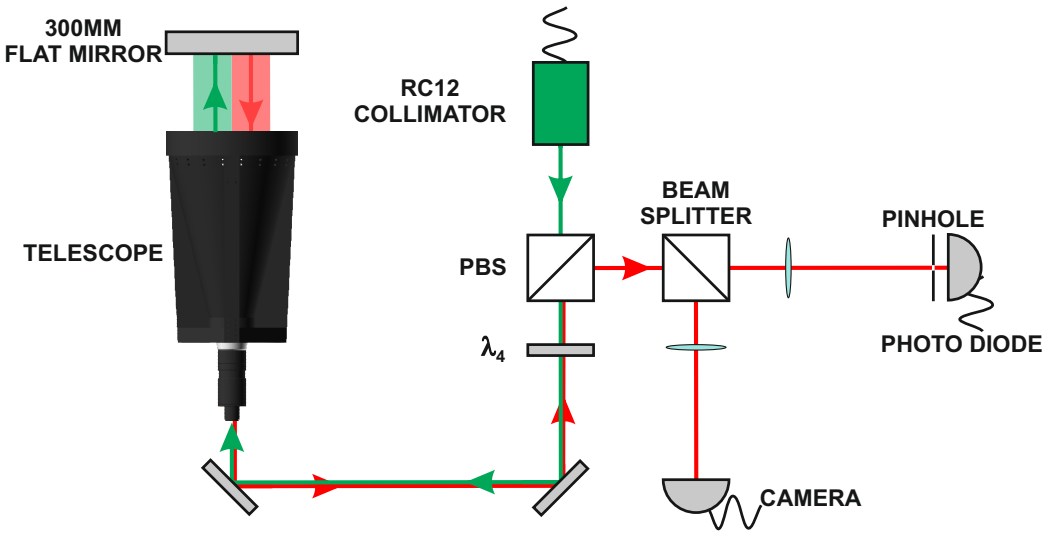

Figure A.1. Schematic sketch of the autocollimation setup. A Thorlabs RC12 reflective collimator is employed as the source of a beam of linearly polarised collimated light with a diameter of 12 mm. The light is then directed through an optical isolator comprising a polarising beam splitter and a $\lambda/4$ plate into the telescope. A flat mirror with a diameter of 300 mm reflects the beam back through the telescope and the optical isolator, where it is deflected into a beam splitter by the polarisation rotation. The split beam is directed onto the camera and the pinhole with an attached photodiode via focusing lenses.

Figure A.2. Image of the autocollimation setup on the optical bench, with one of the lens telescopes for the multi field of view upgrade installed. The 300 mm flat mirror is mounted in a 3D-printed holder, which allows for adjustment of the mirror's angle.

Bibliography

Anderson, J. A.: Astronomical Seeing, Journal of the Optical Society of America, 25, 152, https://doi.org/10.1364/josa.25.000152, 1935.

Anonymous, T. H.: Long and Short Focus, British Journal of Photography, XIII, 138, 1866.

Bailey, D. T.: Meteorological monitoring guidance for regulatory modeling applications, DIANE Publishing, URL https://www.epa.gov/sites/default/files/2020-10/documents/mmgrma_0.pdf, 2000.

Baker, W. E., Atlas, R., Cardinali, C., Clement, A., Emmitt, G. D., Gentry, B. M., Hardesty, R. M., Källén, E., Kavaya, M. J., Langland, R., Ma, Z., Masutani, M., McCarty, W., Pierce, R. B., Pu, Z., Riishojgaard, L. P., Ryan, J., Tucker, S., Weissmann, M., and Yoe, J. G.: Lidar-Measured Wind Profiles: The Missing Link in the Global Observing System, Bulletin of the American Meteorological Society, 95, 543–564, https://doi.org/10.1175/bams-d-12-00164.1, 2014.

Banyard, T., Wright, C., Hindley, N., Halloran, G., Krisch, I., Kaifler, B., and Hoffmann, L.: Atmospheric Gravity Waves in ADM-Aeolus Wind Lidar Observations, Geophysical Research Letters, 48, e2021GL092 756, https://doi.org/10.5194/egusphere-egu21-7911, 2021.

Baumgarten, G.: Doppler Rayleigh/Mie/Raman lidar for wind and temperature measurements in the middle atmosphere up to 80 km, Atmospheric Measurement Techniques, 3, 1509–1518, https://doi.org/10.5194/amt-3-1509-2010, 2010.

Baumgarten, G., Fiedler, J., Hildebrand, J., and Lübken, F.: Inertia gravity wave in the stratosphere and mesosphere observed by Doppler wind and temperature lidar, Geophysical Research Letters, 42, 10–929, https://doi.org/10.1002/2015gl066991, 2015.

Bezanson, J., Edelman, A., Karpinski, S., and Shah, V. B.: Julia: A Fresh Approach to Numerical Computing, SIAM Review, 59, 65–98, https://doi.org/10.1137/141000671, 2017.

Billant, P. and Chomaz, J.-M.: Self-similarity of strongly stratified inviscid flows, Physics of Fluids, 13, 1645–1651, https://doi.org/10.1063/1.1369125, 2001.

Boyd, R. W.: The wavelength dependence of seeing, Journal of the Optical Society of America, 68, 877, https://doi.org/10.1364/josa.68.000877, 1978.

Brooke, J. S. A., Feng, W., Carrillo-Sánchez, J. D., Mann, G. W., James, A. D., Bardeen, C. G., Marshall, L., Dhomse, S. S., and Plane, J. M. C.: Meteoric Smoke Deposition in the Polar Regions: A Comparison of Measurements With Global Atmospheric Models, Journal of Geophysical Research: Atmospheres, 122, 11,112–11,130, https://doi.org/https://doi.org/10.1002/2017JD027143, 2017.

Chanin, M. L., Garnier, A., Hauchecorne, A., and Porteneuve, J.: A Doppler lidar for measuring winds in the middle atmosphere, Geophysical Research Letters, 16, 1273–1276, https://doi.org/10.1029/gl016i011p01273, 1989.

Chen, J., Xie, C., Zhao, M., Ji, J., Wang, B., and Xing, K.: Research on the Performance of an Active Rotating Tropospheric and Stratospheric Doppler Wind Lidar Transmitter and Receiver, Remote Sensing, 15, 952, https://doi.org/10.3390/rs15040952, 2023.

Chen, W., Tsao, C., and Nee, J.: Rayleigh lidar temperature measurements in the upper troposphere and lower stratosphere, Journal of Atmospheric and Solar-Terrestrial Physics, 66, 39–49, https://doi.org/10.1016/j.jastp.2003.09.014, 2004.

Coddington, H.: A Treatise on the Reflection and Refraction of light: being Part I. of a System of Optics, 1829.

Deshler, T.: A review of global stratospheric aerosol: Measurements, importance, life cycle, and local stratospheric aerosol, Atmospheric Research, 90, 223–232, https://doi.org/10.1016/j.atmosres.2008.03.016, 2008.

Dierickx, P.: Optical Performance of Large Ground-based Telescopes, Journal of Modern Optics, 39, 569–588, https://doi.org/10.1080/09500349214550551, 1992.

Drinkwater, M., Borgeaud, M., Elfving, A., Goudy, P., and Lengert, W.: ADM-Aeolus Mission Requirements Document, revision 0, AE-RP-ESA-SY-001 EOP-SM/2047, URL https://earth.esa.int/eogateway/documents/20142/1564626/Aeolus-Mission-Requirements.pdf, 2016.

Einstein, A.: Zur Quantentheorie der Strahlung, Physikalische Zeitschrift, 18, 121–128, https://doi.org/10.1515/9783112596609-016, 1917.

ESA, E. S. A.: Aeolus operations, https://www.esa.int/Enabling_Support/Operations/Aeolus_operations, accessed: 2023-07-30, 2020.

Fernald, F. G.: Analysis of atmospheric lidar observations: some comments, Applied Optics, 23, 652, https://doi.org/10.1364/ao.23.000652, 1984.

Fiedler, F. and Panofsky, H. A.: Atmospheric Scales and Spectral Gaps, Bulletin of the American Meteorological Society, 51, 1114–1120, https://doi.org/10.1175/1520-0477(1970)051<1114:asasg>2.0.co;2, 1970.

Fiedler, J. and Baumgarten, G.: The ALOMAR Rayleigh/Mie/Raman lidar: status after 30 years of operation, Atmospheric Measurement Techniques Discussions, 2024, 1–27, https://doi.org/10.5194/amt-2024-31, 2024.

Fiocco, G. and Smullin, L. D.: Detection of Scattering Layers in the Upper Atmosphere (60–140 km) by Optical Radar, Nature, 199, 1275–1276, https://doi.org/10.1038/1991275a0, 1963.

Flamant, P. H.: Atmospheric and meteorological Lidar: from pioneers to space applications, Comptes Rendus. Physique, 6, 864–875, https://doi.org/10.1016/j.crhy.2005.09.006, 2005.

Folkard, M. and Ward, J.: Fabry-Perot type optical interference filters, Department of Defence, Defence Science and Technology Organisation ..., 1986.

Fricke-Begemann, C.: Lidar investigations of the mesopause region: temperature structure and variability, Ph.D. thesis, IAP, 2004.

Fricke-Begemann, C., Alpers, M., and Höffner, J.: Daylight rejection with a new receiver for potassium resonance temperature lidars, Optics Letters, 27, 1932, https://doi.org/10.1364/ol.27.001932, 2002.

Fried, D. L.: Optical Resolution Through a Randomly Inhomogeneous Medium for Very Long and Very Short Exposures, Journal of the Optical Society of America, 56, 1372, https://doi.org/10.1364/josa.56.001372, 1966.

Friedman, J. S., Tepley, C. A., Raizada, S., Zhou, Q. H., Hedin, J., and Delgado, R.: Potassium Doppler-resonance lidar for the study of the mesosphere and lower thermosphere at the Arecibo Observatory, Journal of Atmospheric and Solar-Terrestrial Physics, 65, 1411–1424, https://doi.org/10.1016/j.jastp.2003.09.004, 2003.

Fritts, D. C. and Alexander, M. J.: Gravity wave dynamics and effects in the middle atmosphere, Reviews of Geophysics, 41, https://doi.org/https://doi.org/10.1029/2001RG000106, 2003.

Froh, J.: Entwicklung spektraler Messmethoden für Doppler-Lidar, https://doi.org/10.18453/ROSDOK_ID00003422, vorgelegt von Jan Froh, 2021.

Froh, J., Höffner, J., Mauer, A., Mense, T. H., Eixmann, R., Lübken, F.-J., Munk, A., Strotkamp, M., and Jungbluth, B.: Aerosol measurements in the tropo- and stratosphere by spectral splitting of Rayleigh and Mie signals within a compact lidar of 1 m3, in: Remote Sensing of Clouds and the Atmosphere XXVII, edited by Comerón, A., Kassianov, E. I., Schäfer, K., Picard, R. H., Weber, K., and Singh, U. N., vol. 12265, SPIE, SPIE, https://doi.org/10.1117/12.2636289, 2022.

Garnier, A. and Chanin, M. L.: Description of a Doppler rayleigh LIDAR for measuring winds in the middle atmosphere, Applied Physics B Photophysics and Laser Chemistry, 55, 35–40, https://doi.org/10.1007/bf00348610, 1992.

Gerding, M., Wing, R., Franco-Diaz, E., Baumgarten, G., Fiedler, J., Köpnick, T., and Ostermann, R.: The Doppler wind, temperature, and aerosol RMR lidar system at Kühlungsborn/Germany – Part 1: technical specifications and capabilities, EGUsphere, 2023, 1–29, https://doi.org/10.5194/egusphere-2023-2733, 2023.

Gordon, J. P., Zeiger, H. J., and Townes, C. H.: The Maser—New Type of Microwave Amplifier, Frequency Standard, and Spectrometer, Physical Review, 99, 1264–1274, https://doi.org/10.1103/physrev.99.1264, 1955.

Hahn, D. W.: Light scattering theory, Department of Mechanical and Aerospace Engineering, University of Florida, p. 18, 2009.

Hansen, P. C., Pereyra, V., and Scherer, G.: Least Squares Data Fitting with Applications, Johns Hopkins University Press, https://doi.org/10.1353/book.21076, 2013.

Hauchecorne, A. and Chanin, M.: Density and temperature profiles obtained by lidar between 35 and 70 km, Geophysical Research Letters, 7, 565–568, https://doi.org/10.1029/gl007i008p00565, 1980.

Hocking, W.: A review of Mesosphere–Stratosphere–Troposphere (MST) radar developments and studies, circa 1997–2008, Journal of Atmospheric and Solar-Terrestrial Physics, 73, 848–882, https://doi.org/10.1016/j.jastp.2010.12.009, 2011.

Hocking, W. K.: Strengths and limitations of MST radar measurements of middle-atmosphere winds, Annales Geophysicae, 15, 1111–1122, https://doi.org/10.1007/s00585-997-1111-1, 1997.

Hulburt, E. O.: Observations of a Searchlight Beam to an Altitude of 28 Kilometers, Journal of the Optical Society of America, 27, 377, https://doi.org/10.1364/josa.27.000377, 1937.

Höffner, J. and Lübken, F.: Potassium lidar temperatures and densities in the mesopause region at Spitsbergen (78°N), Journal of Geophysical Research: Atmospheres, 112, https://doi.org/10.1029/2007jd008612, 2007.

Höffner, J., Froh, J., Mense, T., Mauer, A., Strotkamp, M., Munk, A., Jungbluth, B., and Hoffmann, H.-D.: Ground-based general purpose Doppler-lidar: a technology for Doppler-aerosol measurements and beyond, in: International Conference on Space Optics — ICSO 2020, edited by Sodnik, Z., Cugny, B., and Karafolas, N., vol. 11852, pp. 952–970, SPIE, SPIE, https://doi.org/10.1117/12.2599364, 2021.

Jesse, O.: Die Beobachtung der leuchtenden Wolken, Meteorologische Zeitschrift, p. 179–181, 1887.

Johnson, E. A., Meyer, R. C., Hopkins, R. E., and Mock, W. H.: The Measurement of Light Scattered by the Upper Atmosphere from a Search-Light Beam, Journal of the Optical Society of America, 29, 512, https://doi.org/10.1364/josa.29.000512, 1939.

Khanna, J., Bandoro, J., Sica, R. J., and McElroy, C. T.: New technique for retrieval of atmospheric temperature profiles from Rayleigh-scatter lidar measurements using nonlinear inversion, Applied Optics, 51, 7945, https://doi.org/10.1364/ao.51.007945, 2012.

Khaykin, S. M., Godin-Beekmann, S., Keckhut, P., Hauchecorne, A., Jumelet, J., Vernier, J.-P., Bourassa, A., Degenstein, D. A., Rieger, L. A., Bingen, C., Vanhellemont, F., Robert, C., DeLand, M., and Bhartia, P. K.: Variability and evolution of the mid-latitude stratospheric aerosol budget from 22 years of ground-based lidar and satellite observations, Atmospheric Chemistry and Physics, 17, 1829–1845, https://doi.org/10.5194/acp-17-1829-2017, 2017.

Khaykin, S. M., Hauchecorne, A., Wing, R., Keckhut, P., Godin-Beekmann, S., Porteneuve, J., Mariscal, J.-F., and Schmitt, J.: Doppler lidar at Observatoire de Haute-Provence for wind profiling up to 75 km altitude: performance evaluation and observations, Atmospheric Measurement Techniques, 13, 1501–1516, https://doi.org/10.5194/amt-13-1501-2020, 2020.

Klein, R.: Scale-Dependent Models for Atmospheric Flows, Annual Review of Fluid Mechanics, 42, 249–274, https://doi.org/10.1146/annurev-fluid-121108-145537, 2010.

Langenbach, A., Baumgarten, G., Fiedler, J., Lübken, F.-J., von Savigny, C., and Zalach, J.: Year-round stratospheric aerosol backscatter ratios calculated from lidar measurements above northern Norway, Atmospheric Measurement Techniques, 12, 4065–4076, https://doi.org/10.5194/amt-12-4065-2019, 2019.

Leblanc, T., Sica, R. J., van Gijsel, J. A. E., Haefele, A., Payen, G., and Liberti, G.: Proposed standardized definitions for vertical resolution and uncertainty in the NDACC lidar ozone and temperature algorithms – Part 3: Temperature uncertainty budget, Atmospheric Measurement Techniques, 9, 4079–4101, https://doi.org/10.5194/amt-2016-122, 2016.

LiCuSpace: LidarCUBE — licuspace.de, https://licuspace.de/produkte/lidarcube/, [Accessed 14-02-2024], 2024.

Lindborg, E.: The energy cascade in a strongly stratified fluid, Journal of Fluid Mechanics, 550, 207, https://doi.org/10.1017/s0022112005008128, 2006.

Lorenz, E. N.: Available Potential Energy and the Maintenance of the General Circulation, Tellus, 7, 157–167, https://doi.org/10.1111/j.2153-3490.1955.tb01148.x, 1955.

Lübken, F.-J., Baumgarten, G., Hildebrand, J., and Schmidlin, F. J.: Simultaneous and co-located wind measurements in the middle atmosphere by lidar and rocket-borne techniques, Atmospheric Measurement Techniques, 9, 3911–3919, https://doi.org/10.5194/amt-9-3911-2016, 2016.

Lübken, F.-J. and Höffner, J.: VAHCOLI, a new concept for lidars: technical setup, science applications, and first measurements, Atmospheric Measurement Techniques, 14, 3815–3836, https://doi.org/10.5194/amt-14-3815-2021, 2021.

Maiman, T. H.: Stimulated Optical Radiation in Ruby, Nature, 187, 493–494, https://doi.org/10.1016/b978-0-08-013320-1.50016-6, 1960.

Martin, A., Weissmann, M., Reitebuch, O., Rennie, M., Geiß, A., and Cress, A.: Validation of Aeolus winds using radiosonde observations and numerical weather prediction model equivalents, Atmospheric Measurement Techniques, 14, 2167–2183, https://doi.org/10.5194/amt-14-2167-2021, 2021.

Martucci, G., Navas-Guzmán, F., Renaud, L., Romanens, G., Gamage, S. M., Hervo, M., Jeannet, P., and Haefele, A.: Validation of pure rotational Raman temperature data from the Raman Lidar for Meteorological Observations (RALMO) at Payerne, Atmospheric Measurement Techniques, 14, 1333–1353, https://doi.org/10.5194/amt-14-1333-2021, 2021.

McCormick, M. P., Lawrence, J. D., and Crownfield, F. R.: Mie Total and Differential Backscattering Cross Sections at Laser Wavelengths for Junge Aerosol Models, Applied Optics, 7, 2424, https://doi.org/10.1364/ao.7.002424, 1968.

Measures, R. M.: Laser remote sensing: Fundamentals and applications, Wiley New York, URL https://ui.adsabs.harvard.edu/abs/1984wi...book.....M, 1984.

Mehio, N., Dai, S., and Jiang, D.-e.: Quantum Mechanical Basis for Kinetic Diameters of Small Gaseous Molecules, The Journal of Physical Chemistry A, 118, 1150–1154, https://doi.org/10.1021/jp412588f, 2014.

Mense, T. H., Höffner, J., Baumgarten, G., Eixmann, R., Froh, J., Mauer, A., Munk, A., Wing, R., and Lübken, F.-J.: 3D wind observations with a compact mobile lidar based on tropo- and stratospheric aerosol backscatter, Atmospheric Measurement Techniques, 17, 1665–1677, https://doi.org/10.5194/amt-17-1665-2024, 2024.

Mie, G.: Beiträge zur Optik trüber Medien, speziell kolloidaler Metallösungen, Annalen der Physik, 330, 377–445, https://doi.org/10.1002/andp.19083300302, 1908.

Munk, A., Jungbluth, B., Strotkamp, M., Hoffmann, H.-D., Poprawe, R., and Höffner, J.: Diode-pumped Alexandrite ring laser for lidar applications, in: Solid State Lasers XXV: Technology and Devices, edited by Clarkson, W. A. and Shori, R. K., vol. 9726, pp. 74–79, SPIE, SPIE, https://doi.org/10.1117/12.2212578, 2016.

Munk, A., Jungbluth, B., Strotkamp, M., Hoffmann, H.-D., Poprawe, R., Höffner, J., and Lübken, F.-J.: Diode-pumped alexandrite ring laser in single-longitudinal mode operation for atmospheric lidar measurements, Optics Express, 26, 14 928, https://doi.org/10.1364/oe.26.014928, 2018.

Munk, A., Strotkamp, M., Jungbluth, B., Froh, J., Mense, T., Mauer, A., and Höffner, J.: Rugged diode-pumped Alexandrite laser as an emitter in a compact mobile lidar system for atmospheric measurements, Applied Optics, 60, 4668, https://doi.org/10.1364/ao.422634, 2021.

Munk, A., Scheuer, S., Strotkamp, M., Jungbluth, B., Froh, J., Mense, T., Mauer, A., and Höffner, J.: Energy-scaling of a diode-pumped Alexandrite laser and prototype development for a compact general-purpose Doppler lidar, Applied Optics, 62, 8732, https://doi.org/10.1364/ao.504567, 2023.

Murphy, D. M., Abou-Ghanem, M., Cziczo, D. J., Froyd, K. D., Jacquot, J., Lawler, M. J., Maloney, C., Plane, J. M. C., Ross, M. N., Schill, G. P., and Shen, X.: Metals from spacecraft reentry in stratospheric aerosol particles, Proceedings of the National Academy of Sciences, 120, https://doi.org/10.1073/pnas.2313374120, 2023.

Nappo, C. J.: An introduction to atmospheric gravity waves, vol. 102, Academic press, 2013.

Ofek, E. O. and Ben-Ami, S.: Seeing-limited Imaging Sky Surveys—Small versus Large Telescopes, Publications of the Astronomical Society of the Pacific, 132, 125 004, https://doi.org/10.1088/1538-3873/abc14c, 2020.

Paffrath, U., Lemmerz, C., Reitebuch, O., Witschas, B., Nikolaus, I., and Freudenthaler, V.: The Airborne Demonstrator for the Direct-Detection Doppler Wind Lidar ALADIN on ADM-Aeolus. Part II: Simulations and Rayleigh Receiver Radiometric Performance, Journal of Atmospheric and Oceanic Technology, 26, 2516–2530, https://doi.org/10.1175/2009jtecha1314.1, 2009.

Paschotta, R.: M2 Factor, RP Photonics Encyclopedia, https://doi.org/10.61835/zxz, available online at https://www.rp-photonics.com/m2_factor.html.

Poblet, F. L., Chau, J. L., Conte, J. F., Avsarkisov, V., Vierinen, J., and Charuvil Asokan, H.: Horizontal Wavenumber Spectra of Vertical Vorticity and Horizontal Divergence of Mesoscale Dynamics in the Mesosphere and Lower Thermosphere Using Multistatic Specular Meteor Radar Observations, Earth and Space Science, 9, e2021EA002 201, https://doi.org/10.1029/2021ea002201, e2021EA002201 2021EA002201, 2022.

Poblet, F. L., Vierinen, J., Avsarkisov, V., Conte, J. F., Charuvil Asokan, H., Jacobi, C., and Chau, J. L.: Horizontal Correlation Functions of Wind Fluctuations in the Mesosphere and Lower Thermosphere, Journal of Geophysical Research: Atmospheres, 128, e2022JD038 092, https://doi.org/10.1029/2022jd038092, e2022JD038092 2022JD038092, 2023.

Preusse, P., Ern, M., Bechtold, P., Eckermann, S. D., Kalisch, S., Trinh, Q. T., and Riese, M.: Characteristics of gravity waves resolved by ECMWF, Atmospheric Chemistry and Physics, 14, 10 483–10 508, https://doi.org/10.5194/acp-14-10483-2014, 2014.

Raman, C. V. and Krishnan, K. S.: A New Type of Secondary Radiation, Nature, 121, 501–502, https://doi.org/10.1038/121501c0, 1928.

Rani, S. I., Jangid, B. P., Kumar, S., Bushair, M. T., Sharma, P., George, J. P., George, G., and Das Gupta, M.: Assessing the quality of novel Aeolus winds for NWP applications at NCMRWF, Quarterly Journal of the Royal Meteorological Society, 148, 1344–1367, https://doi.org/10.1002/qj.4264, 2022.

Ratynski, M., Khaykin, S., Hauchecorne, A., Wing, R., Cammas, J.-P., Hello, Y., and Keckhut, P.: Validation of Aeolus wind profiles using ground-based lidar

and radiosonde observations at Réunion island and the Observatoire de Haute-Provence, Atmospheric Measurement Techniques, 16, 997–1016, https://doi.org/10.5194/amt-16-997-2023, 2023.

Rayleigh, L.: XXXIV. On the transmission of light through an atmosphere containing small particles in suspension, and on the origin of the blue of the sky, The London, Edinburgh, and Dublin Philosophical Magazine and Journal of Science, 47, 375–384, https://doi.org/10.1080/14786449908621276, 1899.

Reitebuch, O., Lemmerz, C., Nagel, E., Paffrath, U., Durand, Y., Endemann, M., Fabre, F., and Chaloupy, M.: The Airborne Demonstrator for the Direct-Detection Doppler Wind Lidar ALADIN on ADM-Aeolus. Part I: Instrument Design and Comparison to Satellite Instrument, Journal of Atmospheric and Oceanic Technology, 26, 2501–2515, https://doi.org/10.1175/2009jtecha1309.1, 2009.

Rennie, M. P., Isaksen, L., Weiler, F., de Kloe, J., Kanitz, T., and Reitebuch, O.: The impact of Aeolus wind retrievals on ECMWF global weather forecasts, Quarterly Journal of the Royal Meteorological Society, 147, 3555–3586, https://doi.org/10.1002/qj.4142, 2021.

Robock, A.: Volcanic eruptions and climate, Reviews of Geophysics, 38, 191–219, https://doi.org/https://doi.org/10.1029/1998RG000054, 2000.

Roedel, W. and Wagner, T.: Die atmosphärische Zirkulation, pp. 143–194, Springer Berlin Heidelberg, https://doi.org/10.1007/978-3-662-54258-3_4, 2011.

Scheuer, S., Munk, A., Strotkamp, M., Haefner, C. L., Höffner, J., and Froh, J.: Efficient intra-cavity frequency doubled, diode-pumped, Q-switched alexandrite laser directly emitting in the UV, Optics Express, 32, 7553, https://doi.org/10.1364/oe.513731, 2024.

Schöch, A., Baumgarten, G., and Fiedler, J.: Polar middle atmosphere temperature climatology from Rayleigh lidar measurements at ALOMAR (69° N), Annales Geophysicae, 26, 1681–1698, https://doi.org/10.5194/angeo-26-1681-2008, 2008.

Souprayen, C., Garnier, A., and Hertzog, A.: Rayleigh–Mie Doppler wind lidar for atmospheric measurements II Mie scattering effect, theory, and calibration, Applied Optics, 38, 2422, https://doi.org/10.1364/ao.38.002422, 1999a.

Souprayen, C., Garnier, A., Hertzog, A., Hauchecorne, A., and Porteneuve, J.: Rayleigh–Mie Doppler wind lidar for atmospheric measurements I Instrumental setup, validation, and first climatological results, Applied Optics, 38, 2410, https://doi.org/10.1364/ao.38.002410, 1999b.

Stoffelen, A., Pailleux, J., Källén, E., Vaughan, J. M., Isaksen, L., Flamant, P., Wergen, W., Andersson, E., Schyberg, H., Culoma, A., Meynart, R., Endemann, M., and Ingmann, P.: THE ATMOSPHERIC DYNAMICS MISSION FOR GLOBAL WIND FIELD MEASUREMENT, Bulletin of the American Meteorological Society, 86, 73–88, https://doi.org/10.1175/bams-86-1-73, 2005.

Strotkamp, M., Witte, U., Munk, A., Hartung, A., Gausmann, S., Hengesbach, S., Traub, M., Hoffmann, H.-D., Hoeffner, J., and Jungbluth, B.: Broadly tunable, diode pumped Alexandrite laser, in: Advanced Solid-State Lasers Congress, ASSL, pp. ATu3A–42, Optica Publishing Group, OSA, https://doi.org/10.1364/assl.2013.atu3a.42, 2013.

Synge, E. H.: XCI.A method of investigating the higher atmosphere, The London, Edinburgh, and Dublin Philosophical Magazine and Journal of Science, 9, 1014–1020, https://doi.org/10.1080/14786443008565070, 1930.

Tenti, G., Boley, C. D., and Desai, R. C.: On the Kinetic Model Description of Rayleigh–Brillouin Scattering from Molecular Gases, Canadian Journal of Physics, 52, 285–290, https://doi.org/10.1139/p74-041, 1974.

Timmreck, C.: Modeling the climatic effects of large explosive volcanic eruptions, WIREs Climate Change, 3, 545–564, https://doi.org/https://doi.org/10.1002/wcc.192, 2012.

Tritscher, I., Pitts, M. C., Poole, L. R., Alexander, S. P., Cairo, F., Chipperfield, M. P., Grooß, J., Höpfner, M., Lambert, A., Luo, B., Molleker, S., Orr, A., Salawitch, R., Snels, M., Spang, R., Woiwode, W., and Peter, T.: Polar Stratospheric Clouds: Satellite Observations, Processes, and Role in Ozone Depletion, Reviews of Geophysics, 59, e2020RG000 702, https://doi.org/10.1029/2020rg000702, 2021a.

Tritscher, I., Pitts, M. C., Poole, L. R., Alexander, S. P., Cairo, F., Chipperfield, M. P., Grooß, J.-U., Höpfner, M., Lambert, A., Luo, B., Molleker, S., Orr, A., Salawitch, R., Snels, M., Spang, R., Woiwode, W., and Peter, T.: Polar Stratospheric Clouds: Satellite Observations, Processes, and Role in Ozone Depletion, Reviews of Geophysics, 59, e2020RG000 702, https://doi.org/10.1029/2020RG000702, 2021b.

von Zahn, U. and Höffner, J.: Mesopause temperature profiling by potassium lidar, Geophysical Research Letters, 23, 141–144, https://doi.org/10.1029/95gl03688, 1996.

von Zahn, U., von Cossart, G., Fiedler, J., Fricke, K. H., Nelke, G., Baumgarten, G., Rees, D., Hauchecorne, A., and Adolfsen, K.: The ALOMAR Rayleigh/Mie/Raman lidar: objectives, configuration, and performance, Annales Geophysicae, 18, 815–833, https://doi.org/10.1007/s00585-000-0815-2, 2000.

Wing, R., Hauchecorne, A., Keckhut, P., Godin-Beekmann, S., Khaykin, S., McCullough, E. M., Mariscal, J.-F., and d'Almeida, É.: Lidar temperature series in the middle atmosphere as a reference data set – Part 1: Improved retrievals and a 20-year cross-validation of two co-located French lidars, Atmospheric Measurement Techniques, 11, 5531–5547, https://doi.org/10.5194/amt-11-5531-2018, 2018.

Wing, R., Martic, M., Hauchecorne, A., Porteneuve, J., Keckhut, P., Courcoux, Y., Yung, L., Retailleau, P., and Cocuron, D.: Atmospheric Density and Temperature Vertical Profile Retrieval for Flight-Tests with a Rayleigh Lidar On-Board the French Advanced Test Range Ship Monge, Atmosphere, 11, 75, https://doi.org/10.3390/atmos11010075, 2020.

Witschas, B.: Light Scattering on Molecules in the Atmosphere, pp. 69–83, Springer Berlin Heidelberg, https://doi.org/10.1007/978-3-642-30183-4_5, 2012.

Witschas, B., Lemmerz, C., Geiß, A., Lux, O., Marksteiner, U., Rahm, S., Reitebuch, O., Schäfler, A., and Weiler, F.: Validation of the Aeolus L2B wind product with airborne wind lidar measurements in the polar North Atlantic region and in the tropics, Atmospheric Measurement Techniques, 15, 7049–7070, https://doi.org/10.5194/amt-15-7049-2022, 2022.

Xia, H., Dou, X., Sun, D., Shu, Z., Xue, X., Han, Y., Hu, D., Han, Y., and Cheng, T.: Mid-altitude wind measurements with mobile Rayleigh Doppler lidar incorporating system-level optical frequency control method, Optics Express, 20, 15 286, https://doi.org/10.1364/oe.20.015286, 2012.

Yan, Z., Hu, X., Guo, W., Guo, S., Cheng, Y., Gong, J., and Yue, J.: Development of a mobile Doppler lidar system for wind and temperature measurements at 30–70 km, Journal of Quantitative Spectroscopy and Radiative Transfer, 188, 52–59, https://doi.org/10.1016/j.jqsrt.2016.04.024, 2017.

Young, A. T.: Rayleigh scattering, Physics Today, 35, 42–48, https://doi.org/10.1063/1.2890003, 1982.

Danksagung

An dieser Stelle möchte ich all den Menschen danken, die mich während der Anfertigung dieser Doktorarbeit unterstützt und begleitet haben.

Mein besonderer Dank gilt meinem Doktorvater, Prof. Dr. Franz-Josef Lübken, der es mir ermöglicht hat diese Arbeit zu schreiben. Seine fachliche Expertise, die anregenden wissenschaftlichen Diskussionen und sein Engagement waren entscheidend für den erfolgreichen Abschluss dieser Arbeit.

Dr. Josef Höffner möchte ich im Besonderen danken, für die unzähligen Diskussionen, in denen ich nahezu alles Wesentliche über Lidars gelernt habe. Seine Geduld und Expertise waren von unschätzbarem Wert.

Mein Dank gilt auch dem restlichen, großartigen VAHCOLI-Team, also Dr. Jan Froh, Alsu Mauer und Dr. Ronald Eixmann, für die angenehme Zusammenarbeit und den kollegialen Beistand.

Insgesamt möchte ich den Mitarbeitern der Abteilung Optische Sondierungen und Höhenforschungsraketen des IAPs danken, besonders Prof. Dr. Gerd Baumgarten, Dr. Michael Gerding und Dr. Robin Wing, für die vielen motivierenden Diskussionen rund um meine Dissertation und darüber hinaus.

Ebenfalls danke ich Prof. Dr. John Plane für die Bereitstellung der WACCM-CARMA Modellrechnungen und den wissenschaftlichen Austausch.

Nicht zuletzt danke ich meiner Familie und meinen Freunden für ihre bedingungslose Unterstützung und ihr Verständnis während dieser intensiven Zeit. Ihr habt mir immer den Rücken gestärkt und mich ermutigt weiterzumachen.

Ein besonderer Dank gilt Rebekka. Danke, dass du all das mitgemacht hast und stets an meiner Seite warst. Deine Geduld, Liebe und Widerstandsfähigkeit, stundenlanges Monologisieren über Lidar, Laser und 3D-Druck zu ertragen, waren für mich von unschätzbarem Wert. Ohne deine Unterstützung wäre diese Arbeit ein deutlich freudloseres Unterfangen gewesen.

Danke.